Journal of Atmospheric and Solar–Terrestrial Physics 259 (2024) 106253

Contents lists available at ScienceDirect

Journal of Atmospheric and Solar–Terrestrial Physics

journal homepage: www.elsevier.com/locate/jastp

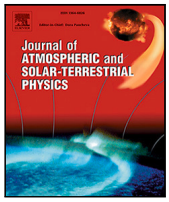

Research paper

Terrestrial and Martian space weather: A complex systems approach

Abraham Chian [a,b,*], Rodrigo Miranda [c], Cesar Bertucci [d], Xóchitl Blanco-Cano [h], Joe Borovsky [e], Sergio Dasso [d], Ezequiel Echer [b], Adriane Franco [f], Kirolosse M. Girgis [g], J. Américo González-Esparza [h], Tohru Hada [g], Hiroshi Hasegawa [i], Syau-Yun Hsieh [j], Primoz Kajdič [h], Christian Mazelle [k], Erico Rempel [b,l], Diana Rojas-Castillo [h], Beatriz Sánchez-Cano [m], David Sibeck [n], Marina Stepanova [o], José Valdés-Galicia [h], Juan Valdivia [p]

[a] University of Adelaide, Adelaide, SA, Australia
[b] National Institute for Space Research (INPE), São José dos Campos, SP, Brazil
[c] University of Brasília, Brasília, DF, Brazil
[d] University of Buenos Aires (UBA-CONICET), Buenos Aires, Argentina
[e] Space Science Institute, Boulder, CO, USA
[f] Federal University of Southern and Southeastern Pará (UNIFESSPA), Marabá, PA, Brazil
[g] Kyushu University, Fukuoka, Japan
[h] National Autonomous University of Mexico (UNAM), Mexico City, Mexico
[i] Institute of Space and Astronautical Science, JAXA, Sagamihara, Japan
[j] Johns Hopkins University Applied Physics Laboratory, Laurel, MD, USA
[k] Research Institute in Astrophysics and Planetology (IRAP), Toulouse, France
[l] Aeronautics Institute of Technology (ITA), São José dos Campos, SP, Brazil
[m] School of Physics and Astronomy, University of Leicester, Leicester, UK
[n] NASA/GSFC, Greenbelt, MD, USA
[o] University of Santiago, Santiago, Chile
[p] University of Chile, Santiago, Chile

ARTICLE INFO

Keywords:
Space weather
Sun–Earth environment
Sun-Mars environment
Complex systems
Nonlinear dynamics

ABSTRACT

A comparative overview of Terrestrial and Martian space weather is presented, with emphasis on applying the tools of complexity and nonlinear dynamics to study the spatiotemporal dynamics and structures of sun–Earth and sun–Mars space environment. The following topics are reviewed: (1) complex systems approach to solar atmosphere and solar wind; (2) complex systems approach to planetary bow shock and magnetosphere–ionosphere; (3) Martian space weather, bow shock, and magnetosphere–ionosphere; (4) imaging planetary magnetosphere–ionosphere.

1. Introduction

Space weather refers to the spatiotemporal changes in the space environment between the sun and planet, which has significant impact on systems and technologies orbiting Earth, Mars, and other planets and moons in the solar system. The nowcasting and forecasting of space weather demand an in-depth understanding of the physical processes from the interior of the sun to the surface of planets and moons. The innovative concepts and techniques of systems science and nonlinear dynamics provide a powerful methodology for the development of science and technology of space weather (Borovsky and Valdivia, 2018; Chang, 2015; Chian et al., 2022; Rempel et al., 2023; Valdivia et al., 2013).

During the 2022 Latin-America Conference on Space Geophysics held at INPE in Brazil, Dr. Chian shared with Dr. Sibeck the idea of a future multi-spacecraft mission to Mars involving a spacecraft for global imaging of Martian magnetosphere–ionosphere in conjunction with a constellation of CubeSats to study the solar wind and Mars interaction and the Martian space weather. Motivated by this idea, a Martian Space Weather (MSW) team has been set up with the objective of applying the systems science approach and nonlinear dynamics tools to improve our understanding of the complex spatiotemporal dynamics and structures of sun–Earth and sun–Mars space environment, as well as to advance the nowcasting and forecasting of Terrestrial and Martian

* Corresponding author at: University of Adelaide, Adelaide, SA, Australia.
E-mail address: abraham.chian@gmail.com (A. Chian).

https://doi.org/10.1016/j.jastp.2024.106253
Received 8 August 2023; Received in revised form 28 April 2024; Accepted 30 April 2024
Available online 6 May 2024

space weather. The initial MSW team consists of an international group of 22 space scientists from 9 countries: Argentina, Australia, Brazil, Chile, France, Japan, Mexico, UK, and USA, representing 16 major space agencies/centers (ESA, INPE, IRAP, JAXA, NASA) and universities.

The present paper is the first joint task of the MSW team aiming to promote open discussions on the similarities and differences between Terrestrial and Martian space weather, based mainly on some published results of the MSW members, which may serve as the blueprint for developing future space missions.

The outline of this paper is as follows.

2. Complex systems approach to solar atmosphere and solar wind

2.1. Solar and interplanetary magnetic flux ropes

The coronal plasma outflowing from the Sun, i.e., the solar wind, is a natural consequence of the high temperature (and consequent high pressure) solar corona. Thus, the pressure gradient wins over gravity and originates a solar wind, transporting solar material to the local interstellar medium.

The solar wind is the main mediator for determining the level of Sun–Earth coupling. As a variable star, changes on Sun activity determines the interplanetary plasma and magnetic properties of the heliosphere, and thus the geo-space, the terrestrial atmospheric environment, as well as the planetary space ambient (e.g., Daglis et al., 2021). As consequence, a deeper understanding of the solar wind properties is crucial to explain the main space weather processes and to make better predictions of the effects of Sun on spatial environments and atmospheres of planets.

The physical state of the solar wind system involves populations of particles (mainly protons and electrons) in interaction with plasma waves and turbulence. Energy of some particle populations can reach relativistic levels. Thus, charged particles and electromagnetism are the main protagonists on a system having complex interactions (e.g., Borovsky, 2021).

Different spatial/temporal scales are involved in the interplanetary physical processes, from milliseconds to thousands of years and from the gyro-cycle radius of ions/electrons to the size of the entire solar system. Depending on the scale of interest, different physical processes are more relevant and then different theoretical frameworks can be used to describe them, as for instance magnetohydrodynamics (MHD), Hall MHD, electron MHD or kinetic theory.

In particular there are three major solar transients affecting the space environments of planets in the solar system, where the solar wind plays a key role. They are: (1) Solar Energetic Particles (SEPs) (e.g., Klein and Dalla, 2017), (2) Stream Interaction Regions (SIRs) (e.g., Richardson, 2018), and (3) Interplanetary Coronal Mass Ejections (ICMEs) (e.g., Temmer, 2021).

Acceleration of particles during solar flares and at shocks driven by CMEs are believed to be the main processes to produce SEPs. After the solar injection, the transport properties of these particles in the interplanetary medium are also keys to forecast their arrival to a given heliospheric location. The physical processes linked with SEP transport in the solar wind include mainly guiding by the mean interplanetary magnetic field and scattering by magnetic fluctuations, which includes waves and turbulence.

The interaction between the fast solar wind coming from coronal holes (CHs) and the slow solar wind, creates SIRs, which can persist for many solar rotations depending on the stability of CHs. SIRs can accelerate energetic particles, decrease the intensity of Galactic cosmic rays (GCRs), and trigger space activity in planetary environments.

The hugest transient objects in the interplanetary medium causing the most geoeffective events are the ICMEs, being the main actors for the Sun–Earth coupling. They transport released magnetic energy and helicity from the Sun to the outer heliosphere, which have crucial consequences on the solar dynamo. ICMEs can also strongly disfigure the global shape of the interplanetary magnetic field (IMF) and plasma properties, in particular adding the presence of bi-directional streams of supra-thermal electrons (energies of 80-1000 eV), parallel and/or antiparallel to the IMF, which is generally regarded as proxy of solar connectivity of field lines (e.g., Dasso et al., 2005).

Their internal magnetic configuration and their interaction with the ambient solar wind are crucial to determine the impact on planetary space ambient.

There is an accumulated evidence indicating that at least a sub-set of ICMEs, called interplanetary magnetic clouds (MCs, Burlaga et al. (1981)) are formed by magnetic field lines that form a helical magnetic structure (i.e., a twisted flux tube called magnetic flux rope).

Interplanetary flux ropes (FRs) can be typically described locally using 2D (symmetry of translation along its main axis) helical MHD equilibria models. In-situ observations also support a circular cross section shape (Démoulin et al., 2016).

The simplest MHD equilibrium model, and theoretically/empirically supported one, is the circular linear force-free model (Lundquist, 1950), which is the theoretically expected MHD structure when relaxation is reached via dissipation of free energy keeping the magnetic helicity constant (i.e., a so-called MHD Taylor state).

From an analysis of a set of well behaved MCs, using a superposed epoch analysis, and considering erosion of the flux rope (Dasso et al., 2006), the typical twist distribution in MCs at 1 au was found to be consistent with the cylindrical force free configuration (Lanabere et al., 2020, 2022). However, evolution of these structures in the solar wind is very important to make predictions in space weather and they are not yet fully understood.

Turbulent properties of the solar wind are also of major interest for space weather. For instance, they are crucial to understand the interaction between particles and electromagnetic fields in the interplanetary medium. Several decades of turbulent properties of the solar wind have been used to model in-situ observations from single spacecraft observations, and only in recent years some results coming from simultaneous multi-spacecraft observations helped to decouple the space/time mix, which enable us to start to understand the full space–time structure of turbulent heliospheric plasmas.

New spacecraft missions will provide empirical bases, in both domains (simultaneous multi-spacecraft observations and observations at different heliodistances) to attack the deficiencies that remain in these two key topics of the solar wind: evolution of interplanetary flux ropes and solar wind turbulence.

2.2. Lagrangian coherent structures in solar turbulence

The dynamical systems approach to turbulence, such as Lagrangian coherent structures and chaotic saddles, provides powerful tools to reveal the complex dynamics of space plasma turbulence (Chian et al., 2022). The particle trajectories in turbulent plasma flows exhibit Lagrangian chaos, where the paths of initially neighboring particles diverge exponentially when averaged over a given time interval yielding positive finite-time Lyapunov exponent (Chian et al., 2023). Unstable and stable manifolds of plasma particles constitute distinguished material lines or surfaces that act as transport barriers in turbulence. These distinguished lines/surfaces are the hyperbolic Lagrangian coherent structures that attract or repel the neighboring material, both retarding and facilitating plasma transport through chaotic mixing, thus are responsible for organizing and mediating the transport and interaction of matter and energy in plasma turbulence. The technique of Lagrangian coherent structures has been applied to elucidate Lagrangian chaos in MHD numerical simulations (Rempel et al., 2011, 2017) and spacecraft observation of solar turbulence (Chian et al., 2014, 2019, 2020, 2023).

Explosive and eruptive events with multiscale spatiotemporal dynamics such as flares and coronal mass ejections in the active Sun and microflares and minicoronal mass ejections in the quiet Sun are driven by photospheric vortical flows in the vicinity of the polarity inversion lines and at supergranular junctions. Hence, the study of the origin and evolution of long-lived vortices in solar turbulence is fundamental for understanding physical processes that lead to coronal eruptions. Kinematic vorticity plays an important role in the evolution of network magnetic fields (Chian et al., 2023). The solar network magnetic fields are among the most distinct structures of the photosphere. They outline the supergranular junctions in the quiet and active Sun, where the diverging flows from nearby supergranular cells collide and turn into converging downdrafts with strong shear where cold plasma returns to the solar interior, resulting in complex interactions between turbulent convective flows and magnetic fields associated with the Kelvin–Helmholtz instability (Chian et al., 2020). The network magnetic fields are organized into predominantly vertical kilogauss flux tubes and form patches of intense magnetic flux concentrations that can persist for hours and even days. Supergranular flows may be the origin of slow solar wind emanating from coronal hole boundaries and switchback events detected in the solar wind (Bale et al., 2019).

Chian et al. (2014) used *Hinode* solar data to establish the correspondence of the network of high magnetic flux concentrations to the attracting Lagrangian coherent structures, and demonstrated that the boundaries of supergranular cells are given by the maxima of the backward finite-time Lyapunov exponent of the horizontal plasma velocity, which expose the location of the sinks of photospheric flows at supergranular junctions in a plage active region. Chian et al. (2019) showed that the center of a supergranular cell is given by the local maximum of forward finite-time Lyapunov exponent and the repelling Lagrangian coherent structures interconnect the Lagrangian centers of neighboring supergranular cells in the quiet Sun. Chian et al. (2020) presented

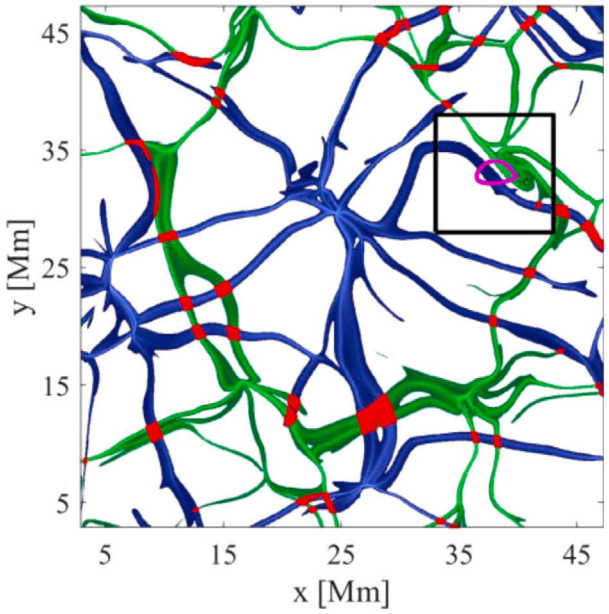

Fig. 1. Hinode observation of Lagrangian chaotic saddles and stretching–twisting–folding Lagrangian coherent structures at supergranular junctions of the quiet-Sun. Lagrangian chaotic saddles (red points) are given by the intersections of the thresholded unstable (green) and stable (blue) manifolds with the threshold given by 0.3×10^{-4}, superposed by the boundary (magenta line) of the kinematic vortex computed by the Lagrangian Averaged Vorticity Deviation (Rempel et al., 2017) for the time interval from 12:53:51 UT to 13:23:51 UT on 2010 November 2. Attracting Lagrangian coherent structures (unstable manifolds) are obtained by the backward finite-time Lyapunov exponent computed from 19:25:29 UT on 2010 November 2 to 08:31:15 UT on 2010 November 2. Repelling Lagrangian coherent structures (stable manifolds) are obtained by the forward finite-time Lyapunov exponent computed from 19:25:29 UT on 2010 November 2 to 06:19:42 UT on 2010 November 3. (For interpretation of the references to color in this figure legend, the reader is referred to the web version of this article.)

observational evidence of Lagrangian chaotic saddles in plasmas given by the intersections of finite-time unstable and stable manifolds as seen in Fig. 1, and showed that the persistent objective vortices are formed in the gap regions of Lagrangian chaotic saddles at supergranular junctions in the quiet Sun. Chian et al. (2023) reported the observational evidence of chaotic stretching–twisting–folding of Lagrangian coherent structures in turbulent vortical flows at a quiet-Sun supergranular junction that cause the intensification of core magnetic field, electromagnetic energy flux, and interface electric current density in two merging magnetic flux tubes trapped by a persistent objective kinematic vortex as seen in Fig. 2.

2.3. Intermediate shock in the solar-planetary environment

One of the most fundamental yet unsettled issues in magnetohydrodynamics (MHD) is the presence of the so-called intermediate shock waves (also known as Alfvén shocks). Specifically, the observational evidence of their existence in real plasmas remains uncertain, and their detection has become an important and challenging issue in future spacecraft missions. Similar to how fast and slow shocks can be considered as the steepened, finite-amplitude versions of their linear wave counterparts, the intermediate shocks may be realized through the steepening of finite-amplitude intermediate waves, as first demonstrated by high-precision numerical simulations (Wu, 1987; Brio and Wu, 1988; Wu, 1988). Certainly, the intermediate shocks satisfy the Rankine–Hugoniot conditions, where upstream and downstream flows are respectively supersonic and subsonic to the intermediate speed, and entropy increases across the shock (Fig. 3).

Nevertheless, the existence of intermediate shocks was considered implausible for quite a long time because they did not satisfy the

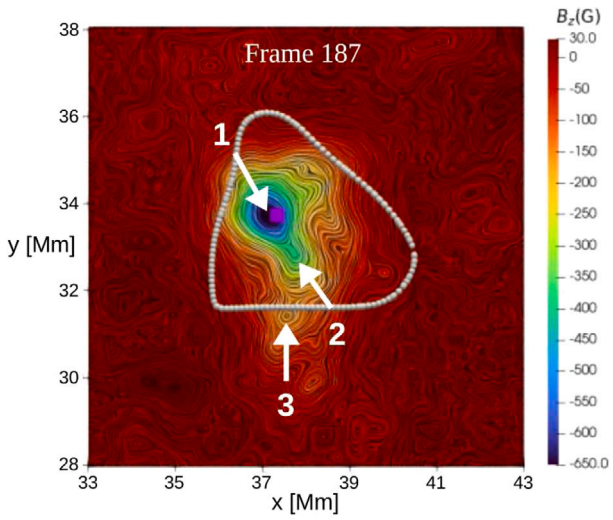

Fig. 2. Hinode observation of the spatiotemporal dynamics of the horizontal electric current density and line-of-sight magnetic field at supergranular junctions of the quiet-Sun at 13:11:51 UT on 2010 November 2. The Line Integral Convolution map of the horizontal electric current density superposed by the line-of-sight magnetic field inside the black box region of Fig. 1. The gray circles denote the boundary of the persistent objective kinematic vortex. The upper two arrows mark the centers of two merging magnetic flux tubes (1 and 2) trapped by the vortex, and the vertical arrow at the bottom marks the center of the third magnetic flux tube (3) which is not trapped by the vortex. The magenta square denotes the location of the maximum of the line-of-sight magnetic field at the interior of vortex boudary near the center of the magnetic flux tube 1. During a time interval of 30 min of the supergranular vortex lifetime, from 12:53:51 UT to 13:23:51 UT, a steady vortex stretching is observed which results in a steady intensification of the core-magnetic field inside tubes 1 and 2 due to vortex trapping; whereas, the core-magnetic field inside the tube 3 decays steadily due to the absence of vortex trapping.

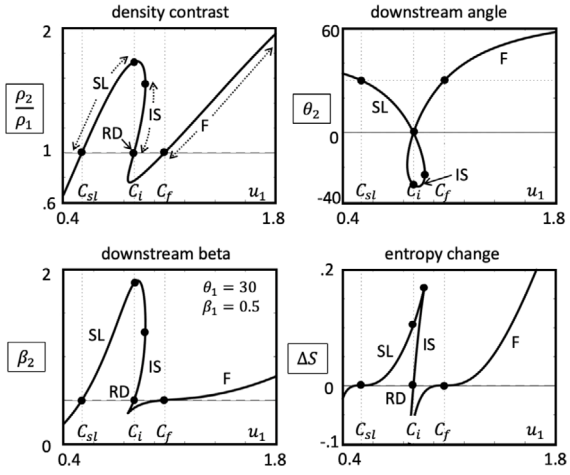

Fig. 3. Solutions of the MHD Rankine–Hugoniot relations. Shown are (a) the density contrast across the discontinuity, (b) downstream magnetic field angle with respect to the shock normal, (c) downstream plasma beta ratio, and (d) the entropy change across the discontinuity, all plotted versus the upstream flow speed. Time stationarity and one-dimensional planar geometry of the discontinuity are assumed. Upstream magnetic field angle relative to the shock normal is 30 degrees, and upstream plasma beta = 0.3. F, SL, IS, RD in the figures stand for the fast, slow, intermediate shocks, and the rotational discontinuity, respectively. Note that the intermediate shock (to be more exact, shown here is the "2-3 intermediate shock", according to the classification by Kennel et al. (1989)) is compressional and entropy increasing, satisfying the second law of thermodynamics.

"evolutionary conditions" (Jeffrey and Taniuti, 1964; Kantrowitz and Petschek, 1964). In other words, infinitesimally small perturbations given to the shock could not be resolved as a superposition of waves

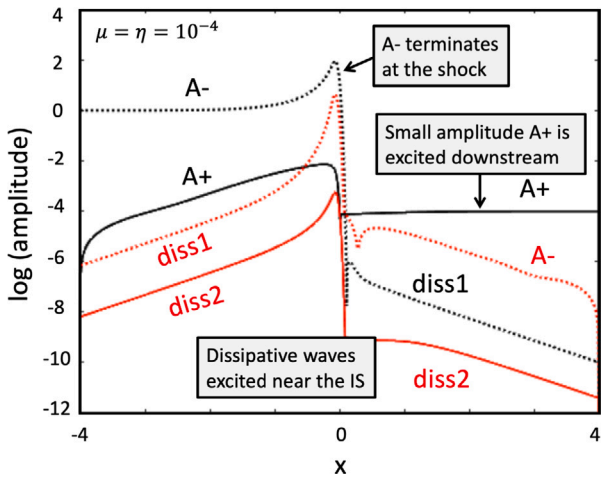

Fig. 4. Interaction between the Alfvén wave and the intermediate shock computed by solving an eigenvalue problem of dissipative MHD. As the Alfvén wave with negative phase velocity (A-) is introduced from upstream ($x < 0$) and reaches the intermediate shock, mode conversion occurs near the shock and the Alfvén as well as dissipative wave modes are excited in such a way that the upstream and downstream perturbations are uniquely connected across the shock. This is possible due to the presence of dissipation.

outgoing from the shock due to the lack of degrees of freedom (i.e., the number of waves). On the other hand, it has been proposed that this entire argument can be drastically altered when dissipation is included in the plasma, no matter how small the dissipation may be (Hada, 1994; Inoue and Inutsuka, 2007). When dissipative wave modes are included, arbitrary perturbations given to the shock can be expressed as a superposition of outgoing wave modes. Therefore, the intermediate shocks are evolutionary in dissipative MHD, and hence, in a real plasma (Fig. 4).

Efforts have been made to detect intermediate shocks in various regions of space plasma. One of the earliest studies was the Voyager 1 data analysis by Chao et al. (1993), in which they attempted to fit the MHD Rankine–Hugoniot relations to the magnetic and plasma data when the spacecraft was at a distance of about 9 AU away from the sun in the solar wind. One of the discontinuities they found exhibited properties specific to intermediate shocks, namely the transition from sub- to super-intermediate flow speed and a sign reversal of the transverse magnetic field (see Fig. 3(b)) across the shock. Further efforts to identify the intermediate shocks in the solar wind have been made by several authors (Feng et al., 2007; Feng and Wang, 2008). A systematic survey of discontinuities in the solar wind and their classification into the MHD shocks and MHD discontinuities was conducted by Tsurutani et al. (2011).

The intermediate shock may exist as an intrinsic part of curved shock such as the planetary bow shock. Fig. 5 shows a schematic of possible shock magnetic field configurations when no symmetry is imposed at the point where the wave propagation vector aligns with the upstream field (Steinolfson and Hundhausen, 1990b,a). When the upstream plasma beta is low, the configuration in (a) with a fast shock on both sides of the central point is physically unrealistic, while that in (b) with an intermediate shock on one side and a fast shock on the other is possible. MHD simulations have been performed to analyze this type of configurations in association with the coronal mass ejection (Steinolfson and Hundhausen, 1990b,a; De Sterck et al., 1998, 1999; De Sterck and Poedts, 2001).

It is well-known that a pair of slow shocks develop from the X-point of the symmetric Petscheck-type magnetic reconnection. Several authors argue that, in asymmetric magnetic reconnections, various MHD discontinuities including the intermediate shocks may develop in

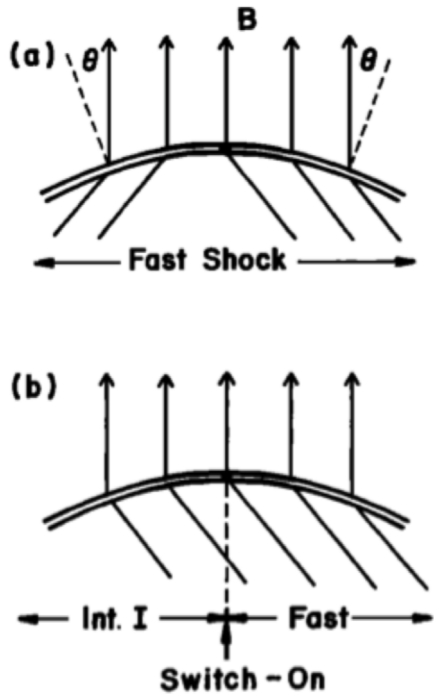

Fig. 5. Low-Mach number 2D shock geometry in a low-beta plasma (Steinolfson and Hundhausen, 1990b). If upstream plasma beta is high and the shock is essentially hydrodynamic, configuration of (a) is possible, while if the upstream beta is low, configuration (b) with an intermediate shock must be chosen. Note the sign reversal of transverse magnetic field across the intermediate shock in (b).

addition to the slow shocks (Lin et al., 1992; La Belle-Hamer et al., 1994; Lin and Lee, 1999).

Formation and evolution of intermediate shocks within the solar atmosphere is a topic that has started to attract significant attention these days. Houston et al. (2020) examined fluctuations in the plasma parameters using spectro-polarimetric data of a large sunspot and compared them with Rankine–Hugoniot relations. They found that the intermediate shock solution provides the closest match between theory and observations at optical depth equivalent to the boundary between the upper photosphere and lower chromosphere. By performing 2D compressible MHD simulations of an Orszag–Tang vortex, Snow et al. (2021) modeled a highly turbulent system in which a variety of shocks and discontinuities are continuously generated, collide with each other, and dissipate. They found that the system is dominated by fast and slow shocks, with far less-frequent intermediate shocks appearing most readily near magnetic reconnection sites.

2.4. Complexity-entropy of solar wind turbulence

The solar wind is in a turbulent state, as evidenced by power spectra displaying power-law scaling with a spectral index nearly -5/3 (Matthaeus et al., 1982; Leamon et al., 1998; Burlaga and F.-Viñas, 2004). Intermittency in the solar wind is characterized by probability distribution functions of fluctuations that become non-Gaussian with decreasing scale within the inertial subrange (Sorriso-Valvo et al., 2001; Koga et al., 2007; Chian and Miranda, 2009). Magnetic reconnection is a mechanism in plasmas that converts magnetic energy into kinetic and thermal energy, and can provide an origin of intermittent magnetic field turbulence in the solar wind (Chian et al., 2016). Turbulence, intermittency and magnetic reconnection in plasmas are intrinsically related in a complex manner. Hence, a complex systems approach is key to improve our understanding of these phenomena.

The Jensen–Shannon (J–S) complexity-entropy index is a statistical tool that can distinguish stochastic processes from deterministic

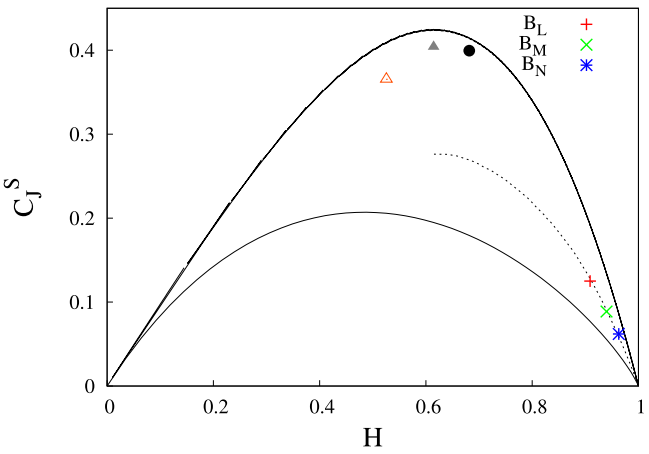

Fig. 6. The complexity-entropy plane for the L (red plus symbol) M (green cross) and N (blue asterisk) components of the magnetic field in a magnetic reconnection exhaust. The full black circle, open red triangle, and full gray triangle represent the chaotic time series of the logistic map, the skew tent map, and the Hénon map, respectively. The crescent-shaped curves represent the minimum and maximum values of the complexity C_J^S for a given value of the entropy H, and the dotted line represents stochastic fractional Brownian motion.. (For interpretation of the references to color in this figure legend, the reader is referred to the web version of this article.)
Source: Adapted from Miranda et al. (2021)

chaos (Rosso et al., 2007), and has been successfully applied to experiments with electronic oscillators (Soriano et al., 2011), stock market data (Zunino et al., 2009), the Southern Oscillation index (Bandt, 2005) and river streamflow data (de Carvalho Barreto et al., 2023). Interplanetary magnetic field data collected by the Wind spacecraft has been compared to magnetic field data from the Swarthmore Spheromak Experiment and the ion saturation current data from the Large Plasma Device using the J–S index by Weck et al. (2015). Their results indicate that the Wind data displays higher entropy and lower complexity than the data from the experimental devices, due to the physically confined nature of the experiments compared to the interplanetary magnetic field data. The J–S index has been applied to solar wind data detected by the Helios, Wind and Ulysses spacecraft by Weygand and Kivelson (2019), showing that the complexity decreases and the entropy increases with the distance from the Sun. This trend was also observed for greater radial distances (out to $\sim$ 34 AU) using data from Voyager 2 by Raath et al. (2022). However, they note that a decreasing signal-to-noise ratio at radial distances $\gtrsim$ 20 AU due to instrumental uncertainty can result in an increase of the permutation entropy.

The solar wind can be regarded as a complex network of entangled magnetic flux tubes and Alfvénic fluctuations propagating within each flux tube (Bruno et al., 2001; Borovsky, 2008). Flux tubes can emerge locally in the turbulent solar wind as a consequence of energy cascade (Matthaeus and Montgomery, 1980; Veltri, 1999; Greco et al., 2008, 2009; Telloni et al., 2016), or can be advected by the solar wind as "fossil" structures from the solar surface (Bruno et al., 2001; Borovsky, 2008). Magnetic reconnection is essential to understand the dynamics of solar flares, coronal mass ejections, rope–rope magnetic reconnection in the solar wind, and the interaction between the solar wind and planetary magnetospheres. The conversion of magnetic energy into kinetic and thermal energy during magnetic reconnection leads to the formation of magnetic exhausts. Several characteristics of magnetic exhausts have been unveiled using *in-situ* data in the solar wind. For example, Enžl et al. (2014) showed that the magnetic flux available for reconnection and the reconnection efficiency increase with the magnetic shear angle. Mistry et al. (2017) demonstrated that the guide magnetic field within the exhaust is enhanced, and the plasma density and ion temperature at the exhaust increase as a function of the inflow plasma beta and the guide field.

Intermittent turbulence in time series can be characterized by computing the scaling exponents of higher-order statistics that require a large number of data points for convergence. The computation of the J–S index depends on the construction of probability functions of ordinal patterns, which can be obtained using relatively short time series. Since magnetic exhausts usually have a short duration (Enžl et al., 2014), the J–S index can be a useful tool to understand turbulence within magnetic exhausts. In Miranda et al. (2021), the J–S index of magnetic field fluctuations was obtained for four different magnetic exhausts in the solar wind at 1 AU. The magnetic field components were projected into the LMN coordinates using the hybrid minimum variance analysis (Gosling and Phan, 2013). The L direction is related to the exhaust outflow direction, the M direction is related to the reconnection guide field direction, and the N component is related to the normal of the current sheet. Fig. 6 shows the complexity-entropy plane, and the J–S index for the L, M and N magnetic-field components in a magnetic exhaust observed by the Wind spacecraft at the interior of a magnetic cloud associated with an interplanetary coronal mass ejection, with a main shock arrival detected at 1:13 UT on 1997 December 30. The crescent-shaped curves indicate the minimum and maximum complexity values for a given value of entropy. This figure shows that all magnetic field components display J–S index values corresponding to stochastic fluctuations, in agreement with previous studies (Weck et al., 2015; Weygand and Kivelson, 2019). For the four events analyzed, the L component displays lower degree of entropy and higher degree of complexity than the M and N components. Miranda et al. (2021) demonstrated that coherent structures, which are responsible for intermittency within the inertial subrange, are also responsible for lower values of entropy and higher values of complexity, which is in agreement with numerical simulations of MHD turbulence (Rempel et al., 2009; Miranda et al., 2015). These results can contribute to the understanding of the complex energy conversion process during magnetic reconnection events in the solar wind.

2.5. Extreme events and origin of multifractality in solar wind turbulence

The solar wind is permeated by coherent structures such as magnetic flux ropes and current sheets (Chian et al., 2016). Current sheets are the main contributors for multifractality and departure from Gaussianity in the probability distribution functions (PDFs) of magnetic-field fluctuations in intermittent turbulence (Marsch and Tu, 1997; Burlaga, 2001; Bruno and Carbone, 2013; Bruno, 2019; Gomes et al., 2019, 2023). Such phenomena are closely related to the occurrence of extreme events, which are events with high amplitude in comparison with the distribution's mean.

Gomes et al. (2019) and Gomes et al. (2023) conducted a statistical analysis of extreme events and multifractality in the solar wind magnetic-field data detected by the fluxgate magnetometer (FGM) onboard Cluster-1, with 22 Hz sampling frequency. Fig. 7(a) shows the time series for 2008 March 9 (red). The green regions denote current sheets, which are responsible for intermittent extreme events in the series, as revealed by Gomes et al. (2019). Fig. 7(b) shows the time series for 2016 January 25, which is characterized by a higher degree of stationarity and the absence of current sheets (Gomes et al., 2019). Fig. 7(c) compares the ζ scaling exponents of the $|\mathbf{B}|$ series of 2008 March 9 (red line with circles) with the ζ scaling exponents of its random phases series (magenta line with triangles). Since the random phases series has a Gaussian PDF, it removes from the original series the intermittent extreme events responsible for the fat-tailed PDF and the ζ scaling exponent becomes linear, following the Kolmogorov (K41) monofractal line (dashed line). This result reveals the importance of the contribution from a fat-tailed PDF to the multifractality of the time series of 2008 March 9. In Fig. 7(d), the same analysis is done for the time series of 2016 January 25, where both the original series and its random phases series show an Iroshnikov–Kraichnan (IK) linear behavior. The time series of 2016 January 25 does not have a fat-tailed PDF, although it has a multifractal spectrum (see Fig. 9 in Gomes et al. (2023)).

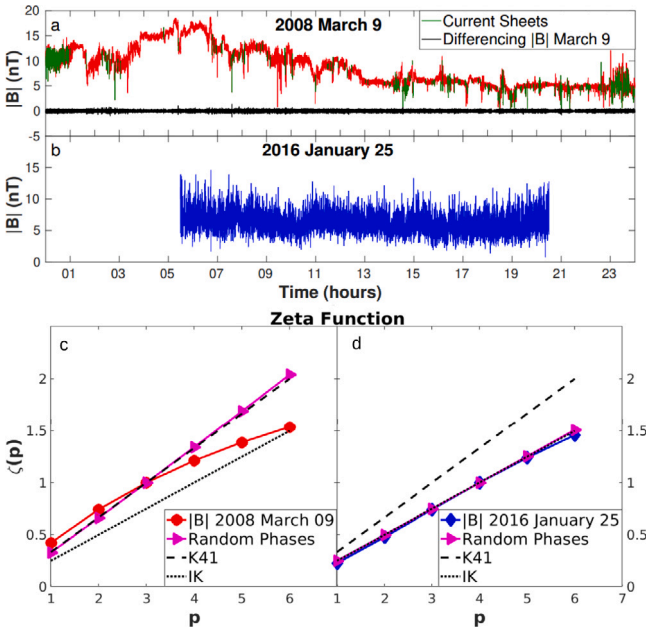

Fig. 7. Solar wind time series of $|\mathbf{B}|$ measured by Cluster-1 for (a) 2008 March 9 (red), containing current sheets (green); (b) for 2016 January 25 (blue), without current sheets. Zeta functions for $|\mathbf{B}|$ for (c) 2008 March 9 (red circles) and its Random Phases (magenta triangles); (d) for 2016 January 25 (blue diamonds) and its Random Phases (magenta triangles). The dashed lines represent the K41 scaling and the dotted lines, the IK scaling. (For interpretation of the references to color in this figure legend, the reader is referred to the web version of this article.)
Source: Adapted from Gomes et al. (2023).

Since both time series of 2016 January 25 and 2008 March 9 series are multifractal, but only for the time series of 2008 March 9 the ζ-scaling is nonlinear, we conclude that the ζ-function is capable of measuring multifractality when it is due to intermittency, or fat-tailed PDFs, but not when it is due to long-range correlations. Gomes et al. (2023) showed that a multifractal detrended fluctuation analysis (MFDFA) is more appropriate than the ζ-function to study multifractality in the solar wind. The results of Gomes et al. (2019) and Gomes et al. (2023) suggest that the solar wind is always multifractal, but for time series with current sheets, the magnetic-field turbulence follows a K41-scaling and multifractality is due to both intermittency and nonlinear correlations; for time series without current sheets, turbulence follows an IK-scaling and multifractality is predominantly produced by long-range correlations.

2.6. Interplanetary origin of geomagnetic storms

Geomagnetic storms are large disturbances in the Earth's magnetosphere–ionosphere system due to enhanced solar wind magnetosphere coupling, mainly through the magnetic reconnection mechanism (Dungey, 1961). The merging between the interplanetary magnetic field (IMF) and the Earth's magnetic field occurs preferentially when the IMF Bz component has a large intensity, a long duration, and is southward directed (Bs), opposite to the Earth's magnetopause dayside field (Dungey, 1961; Gonzalez et al., 1994, 1999). The strength of a geomagnetic storm is usually measured by the Dst index, derived from ground based low latitude magnetometers (Sugiura, 1964). According to the peak value of Dst, geomagnetic storms are usually classified as intense, Dst ≤ -100 nT; moderate, $-100 <$ Dst ≤ -50 nT, or weak, $-50 <$ Dst ≤ -30 nT (Gonzalez et al., 1994, 1999).

The occurrence of intense storms is preceded by disturbed interplanetary conditions, such as the presence of large Bs fields ≥10 nT (or the

equivalent electric field Ey dawn to dusk component ≥5 mV/m), with duration longer than 3 h. These conditions are also called the interplanetary Ey criteria (Gonzalez and Tsurutani, 1987). These criteria were confirmed in following studies (Echer et al., 2008; Rawat et al., 2018). Specific Ey criteria for moderate storms were also determined (Echer et al., 2013).

The major interplanetary structures in the solar wind which can be sources of significant Bs and consequent geomagnetic activity are interplanetary coronal mass ejections (ICMEs) and their sheath regions, which can occur alone or in combination. Their combined occurrence occurs when there are Bs fields in both the ICME and in the sheath between the ICME driven shock and the ICME front boundary. The other important structures are corotating interaction regions (CIRs) and their driving coronal hole high speed streams (HSS) (Tsurutani et al., 1988; Gonzalez et al., 1999, 2007, 2011).

Gonzalez et al. (2007) and Echer et al. (2008) have investigated the solar cycle variation of interplanetary drivers of 90 intense geomagnetic storms during solar cycle 23 (1996–2006). It was found that the most important interplanetary structures leading to intense geomagnetic storms, and the percentage of storms they caused in cycle 23 were: ICME driving shocks, (24%), sheath fields, (24%), combined ICME and sheath fields, (16%), and CIRs, (13%). During the rising and maximum phases of cycle 23, most of intense storms were caused by ICME and sheath fields combined, or by sheath fields alone. While in the declining and minimum phases there was a similar contribution of CIRs, combined sheath and ICME fields, and pure sheath fields in causing storms. Intense storms showed a near in phase variation with sunspot number, with storm rates of: 3 storms per year in the minimum and rising phases, 8.5 storms per year in the maximum phase and 6.5 storms per year in the declining phase of the solar cycle.

For moderate storms occurring during solar cycle 23, Echer et al. (2013) studied the interplanetary origin of 213 storms. The solar cycle distribution of moderate storms showed a dual peak variation with sunspot cycle, with occurrence peak near solar maximum and another in the descending phase, around 3 years later. The highest rate of moderate storms was found as 25 storms per year in the declining phase. The major interplanetary drivers of moderate storms and the percentage of storms they caused were: CIRs and their HSS drivers, (47%), ICMEs, (20%), sheath fields, (10.8%), and ICME and sheath combination of fields, (10%). CIRs and HSSs were the dominant drivers in the declining phase and at solar minimum, while those interplanetary structures had the same level of importance as ICMEs combined with their sheath fields in the rising and maximum solar cycle phases. Interplanetary Ey criteria for moderate magnetic storms were also derived. It was found that around 80% of the moderate storms followed the criteria of Ey ≥ 2 mV/m for intervals longer than 2 h.

Rawat et al. (2018) studied comparatively the interplanetary drivers of geomagnetic storms (intense and moderate) for the cycles 23 and 24 ascending to early descending phases. It was found in that work a reduction of about 75% (34%) in intense (moderate) storm occurrence rate during cycle 24 compared to cycle 23. ICMEs combined with sheath fields, or ICME and sheath fields isolated were identified to be the dominant drivers for intense storms during cycle 24 (89%) and cycle 23 (64%). The Bs and Ey fields were weaker for the cycle 24 interval compared to a similar interval in cycle 23.

Solar cycle 24 was weaker than cycle 23 (Gonzalez et al., 2011; Hajra et al., 2021). A long term study of geomagnetic storms was performed from January 1957 through December 2019 (1523 storms) by Hajra et al. (2021). The yearly rate of storms had high correlation with lag near zero with sunspot number, with a periodicity of near 10–11 years. Solar cycles 20 and 24 were found to be significantly weaker compared to the cycles 19, 21, 22, and 23 in solar flux, solar wind–magnetosphere coupling, and resultant geomagnetic activity.

Most of storms are driven by Bs fields due to a single interplanetary structure or a combination of them (ICME and sheath fields). However some storms have more complex Dst profiles. They seem be caused by the interaction between different interplanetary structures, especially ICME-ICME or ICME-CIR interactions. Dal Lago et al. (2006) analyzed the 21-22 October 1999 storm which had a contribution of a HSS overtaking an ICME. Dasso et al. (2009) found two MC interacting in the long ICME interval leading to the very intense storm of May 2005. Cid et al. (2008) discussed the role of complex interplanetary structures (mainly interaction of ICMES) in causing or intensifying very intense geomagnetic storms.

Finally, it has been noted that all very strong or superstorms (Dst ≤ −250 nT) have occurred due to ICME and sheath fields or their combined occurrence as simple or complex events. No superstorm so far has been caused only by CIR and HSS fields (Gonzalez et al., 2011; Meng et al., 2019).

2.7. Geoeffectiveness of interaction regions of fast and slow solar wind

The Stream Interaction Regions (SIR) form in the interplanetary medium when a fast solar wind stream overtakes a slow one. Fast and slow solar wind streams have different physical properties and originate from different solar sources. Fast streams are originate from coronal holes (Zirker, 1977; Cranmer, 2009) while slow streams came from regions around the solar streamer belt (Antiochos et al., 2011). Their interaction is a consequence of solar rotation. Since the two streams have different magnetic fields, they cannot mix and are separated by a tangential discontinuity (stream interface). A compression region builds up around the stream interface, and their boundaries eventually steepen and form two shock waves. A forward shock (FS) propagates against the slow ambient wind, and a reverse shock (RS) propagates against the fast ambient wind. The FS compresses and accelerates the slow ambient wind, and the RS compresses and decelerates the fast ambient wind. The two compressed streams tend to equalize their speeds (Krieger et al., 1973; Smith and Wolfe, 1976; Zirker, 1977; Tsurutani et al., 2006).

There is a gradual heliocentric evolution of the SIRs. In the inner heliosphere, when they are still in formation, they do not have shocks at their boundaries but compressive waves. Beyond 1 AU, the two boundary shocks form and strengthen. The interaction region expands and increases its radial width with the heliocentric distances (Smith and Wolfe, 1976). The large-scale dynamics of the solar wind change with the solar cycle (González-Esparza and Smith, 1996; Gonzalez-Esparza, 2000). SIR events dominate these dynamics in the descending and minimum phases of the solar cycle (González-Esparza and Smith, 1997). When low-latitude coronal holes are maintained for several solar rotations, the SIR form recurrently and are called corotating interaction regions (CIRs). When there is a quasi-stable low-latitude coronal hole, it can produce CIRs generating recurrent geomagnetic activity during several solar rotations. As the source of the fast solar wind stream, these stable low-latitude coronal holes can produce CIRs generating recurrent geomagnetic activity during several solar rotations (Richardson, 2006; Tsurutani et al., 2006).

SIRs are the primary source of geomagnetic storms during the descending and minimum phases of the solar cycle. In general, the geomagnetic storms caused by SIRs are not as intense as the ones caused by the CMEs (Richardson, 2006; Tsurutani et al., 2006). However, as the SIRs evolve at further heliocentric distances and become wider and their shocks strengthen, then it is possible that these events would be more effective on other planets beyond 1 AU.

It is important to understand better the space weather roles SIR have on Mars and their surroundings.

Around 1/3 of CIRs/SIRs are followed by moderate or intense geomagnetic storms (Alves et al., 2006). Although this percentage is lower than for ICMEs it has been found that CIRs are the more common interplanetary driver of moderate storms in the declining and minimum solar cycle phases (Tsurutani et al., 2006; Echer et al., 2008). Further, in those phases a significant number of intense storms is also driven by CIRs/SIRs (Gonzalez et al., 2007; Echer et al., 2008).

Another type of geomagnetic activity is due to CIR/SIRs. The high intensity long duration continuous auroral electrojet activity (HILDCAAs) (Tsurutani and Gonzalez, 1987) occurs mainly after SIR/CIRs (Hajra et al., 2013). HILDCAAS are an enhanced interval of high latitude geomagnetic activity observed usually in the recovery phase of magnetic storms. HILDCAAS can last from days to weeks. During these intervals there are quasi periodical fluctuations in solar wind and magnetospheric parameters of several hours (Souza et al., 2016), intensification of relativistic electrons in the Earth's radiation belts (Hajra et al., 2014), enhanced auroral activity (Guarnieri, 2006) and geomagnetic disturbances (Mendes et al., 2022), among other effects.

Studies of solar wind effects on Mars are limited by the smaller amount of solar wind data available near Mars orbit compared to the near continuous observations near Earth in the last couple of decades. To determine solar wind parameters near Mars orbit one has to use solar wind propagation models or *in situ* measurements of Mars orbiting spacecraft. However these spacecraft stays only part of their orbit in the solar wind making the available data sporadic.

In a study using Mars Express data, Dubinin et al. (2008) observed the effect of SIRs/CIRs on Mars. Those authors found that the magnetic barrier ceased to be a shield for the incoming solar wind. As a result, large parcels of solar wind plasma penetrated into the Mars induced magnetosphere and sweep out dense plasma from the ionosphere. The topside Martian ionosphere became fragmented consisting of intermittent cold/low energy and energized plasmas. These effects were observed at least until altitudes of 270 to 300 km.

Lee et al. (2017) studied the first years of MAVEN data and the solar wind conditions. Those authors showed the arrival of energetic particles and electrons associated with a CIR, which can cause disturbances in Martian space environment.

Zhao et al. (2023) studied the proton cyclotron wave (PCW) occurrence rate in Mars during the passage of CIRs/SIRs and found that the PCW occurrence rate is increased by a factor of about 1.8 during the SIR phase relative to the pre-SIR and post-SIR phases. This enhanced wave occurrence may have important effects on Mars atmosphere and extraction of planetary ions through wave-particle interactions (de Souza Franco et al., 2019; Franco et al., 2023).

Geyer et al. (2021) studied the proprieties of CIRs/SIRs near Earth and Mars for cycle 24. They found that both the pressure and the occurrence of fast shocks are enhanced for CIRs/SIRs observed near Mars in relation to Earth. It has also been observed that solar wind varies with heliocentric distance, with CIR/SIR shocks became more common for distances longer than 1 AU (Smith and Wolfe, 1976; Echer et al., 2020).

Considering these features of interplanetary dynamics and observed effects on Mars it will be important to conduct future research to investigate the impact of solar wind and CIRs on Martian environment.

3. Complex systems approach to planetary bow shock and magnetosphere–ionosphere

3.1. Planetary magnetosphere as a complex system

In general, planetary magnetospheres seem to display multi-scale non-linear complex behavior; being the Earth magnetosphere, formed by the interaction between the Earth's magnetic field and the persistent solar wind, the more extensively studied case. In fact, a number of works indicate that the magnetospheric turbulence has an intermittent character (Angelopoulos et al., 1999; Consolini and De Michelis, 1998; Borovsky et al., 1997; Stepanova et al., 2003) and displays self-organization (Klimas et al., 2000). For example, in Fig. 8(a) we can observe the time series of the AE index. By defining events through a threshold value (horizontal line), we can compute a proxy for the amount of energy dissipated during the event as $\int AE^2(t)dt$. We then can construct the distribution of different measures, such as the energy dissipated (as shown in Fig. 8(b)), time duration, waiting time between

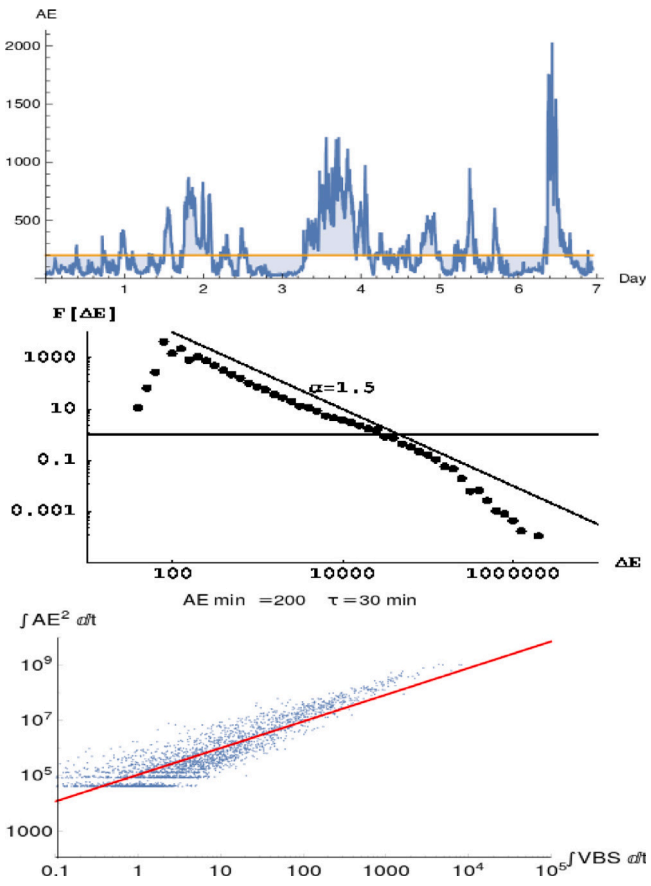

Fig. 8. (a) The AE index and the definition of the threshold to define events. (b) Event statistics of energy dissipated, taken as $\Delta E = \int AE^2 dt$ during an event, which follows a power law. (c) The energy dissipated as a function of $\int VB_s dt$ during the same event.

events, etc. Interestingly enough, as discussed by many researchers, the event statistics seem to display power law behavior, which is an indication of self-similarity and self-organization. Indeed, there have been a number of attempts to introduce physics based models, such as sandpile models, that are capable of displaying such behavior. One particular case, is the canonical model for nonlinear-intermittent reconnection, produced by spatio-temporal chaos (Klimas et al., 2000; Valdivia et al., 2013), and which displays self-organization. Moreover, it is possible to plot our proxy for the energy dissipated during the event vs a proxy for the solar wind input, namely $\int VBs(t)dt$, as shown in Fig. 8(c). It suggests that despite considerable complexity for small events, there is a direct relation for rather large events. This is a reflection of a bifurcation diagram that the canonical nonlinear-intermittent reconnection model (Valdivia et al., 2013) is able to reproduce. It is also a consequence of the self-organization processes that occur in the magnetotail and the complex dynamics it produces.

Moreover, the Earth's magnetosphere is a nonlinear high-dimensional system, that is driven by an also high dimensional turbulent and nonlinear solar wind. In addition, the complex Earth magnetosphere is composed of a number of sub systems, that are connected by fields and plasma waves (Borovsky and Valdivia, 2018). However, it is open and dissipative, so that the current view is that it evolves in a low-D (low dimensional) "attractor" that can be described by a few state variables (a combination of magnetospheric and solar wind variables). This paradigm has proliferated low-D models (Vassiliadis et al., 1999), that sometimes have been reconstructed by applying artificial intelligence techniques. Some of these models are currently taken as operational magnetospheric forecasting models by a number of space weather services around the world. However, as a high-D system, there

are inherent fluctuations that through the nonlinearity of the system can significantly perturb the "attractor" producing dynamical behavior that can be quite complex. Furthermore, recent research on the nature of geomagnetic storms and substorms have shown that they are indeed affected by turbulence (El-Alaoui et al., 2013; Stepanova et al., 2011). Hence, despite important scientific advances, there are numerous problems that remain unsolved (Denton et al., 2016; Borovsky and Valdivia, 2018), some due to these fluctuations-nonlinearity interaction, which would have consequences for the construction of more reliable space weather forecasting models.

In addition, in a number of the magnetospheric regions we observe relevant levels of turbulence (Borovsky et al., 1997; Pinto et al., 2011; Stepanova et al., 2011), therefore, fluctuations can non-linearly feedback to the dynamics and affect other regions, making for an interesting evolution. One strategy to study the relevance of these fluctuations-nonlinearity interactions is through the multifractal spectra. In Fig. 9(a) we observe different multifractal spectra for different subsets of the AE index, which were computed using a wavelet technique (Valdivia et al., 2013). This is a reliable methodology to try to estimate the width of the spectra, which serves as a quantification of the fluctuations-nonlinearity interaction and the strength of the complexity in the system. Clearly, the different subsets produce a consistent view of the multifractality of the system. The wider the spectra, the more intermittent and complex the behavior is. Such analysis has also been conducted to study the spatial variation of this multifractal spectral width for magnetic fluctuations at satellite heights (Toledo et al., 2021), showing that these fluctuation-nonlinearity interactions can become quite relevant. Furthermore, the width of the spectra has consequences for the reliability and robustness of the low-D solar wind-driven models that can be constructed.

Of course, to properly understand the evolution of the magnetosphere though these low-D models, we must account for these fluctuations. For example, Blunier et al. (2021) proposed a method to take advantage of the fluctuation-nonlinearity interaction through a technique based on machine learning to discover the relevant system science variables that determine the evolution of the system. The methodology was to train a neural network model for the dynamics of $\vec{X}(t) = [Dst(t), AL(t), AU(t)]$ (at 1 hr resolution), namely,

$$\vec{X}(t+1) = F(\vec{X}(t), \vec{I}(t), \ldots, \vec{I}(t - m\tau)),$$

using solar wind drivers $\vec{I}(t) = [Bz, By, Bx, V, VBs, n, T, P, \epsilon_A]$ (these variables are magnetic field B, plasma velocity V, density of particles n, temperature T, dynamic pressure P, and Akasofu's parameter ϵ) at different time delays. After training, the robustness of each of the variables entering the model was estimated by adding noise to that particular variable in F and estimate how much it degraded the predictability of $\vec{X}$. The training is done by back propagation over one step error and avoids overfitting by minimizing the one step error over the testing set. They found that the predictability was very sensible to some particular variables (at t or at previous delay times), which we will call the robust variables, while others did not affect it in a significant manner. In Fig. 9(b) we show the relative error produced by shuffling the order of a given variable at a particular time delay. We observe that the number of robust solar wind variables, affecting the dynamics of the system, are only 6 that produce sensible effects over the error. This defines the robust model that is trained with only these 6 solar wind variables, which can now be used as a dynamical system to generate a forecast of $\vec{X}$ assuming known solar wind variables at time t and at previous time delays. The forecasting capabilities of the system is shown in Fig. 9(c) for a particular storm that is not in the training nor testing sets. In Blunier et al. (2021) the authors note that the iterated error becomes smaller compared with an equivalent model using a larger set of solar wind parameters as drivers. Hence, we have taken advantage of the fluctuations of the system to find the relevant solar wind parameters that affect, in a robust manner, the dynamics of the system.

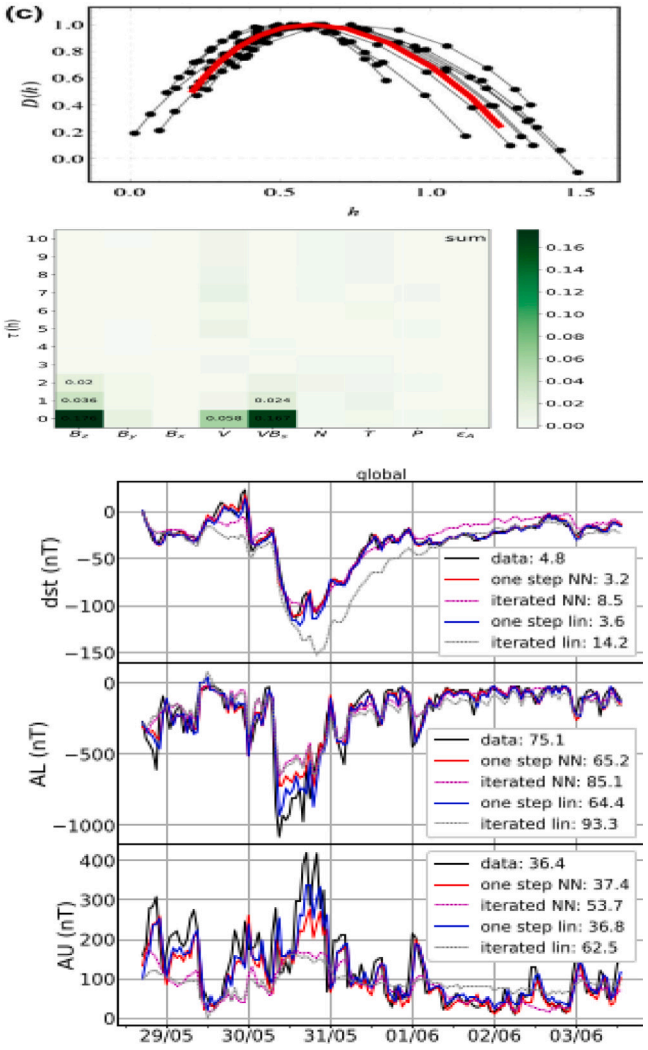

Fig. 9. (a) Different multifractal spectra that are superposed for different subsets of the AE index (taken from Valdivia et al. (2013)). They were computed using a wavelet technique that allows to reconstruct, in a consistent manner, the width of the spectra (adapted from Valdivia et al. (2013)). (b) An account of the solar wind variable robustness in a neural net model for the evolution of $\vec{X}(t) = [Dst(t), Al(t), Au(t)]$ from solar wind variables (x axis) at different time delays (y axis). We display the relative error produced when shuffling a particular solar wind driver (adapted from Blunier et al. (2021)). Here we note that there are only 6 robust, or relevant, variables. (c) Iterated forecast for $\vec{X}(t)$ assuming we know the 6 relevant solar wind variables used for the robust model.(adapted from Blunier et al. (2021)).

Hence, these complex techniques provide insight about the role played by the nonlinearity and high dimensionality in the resulting dynamics of the system, and particularly can help discover the effective low-D "attractor" and find the robust variables that determine its dynamics. As such they offer an opportunity to understand the planetary magnetospheric dynamics, discover the physically relevant variables determining the evolution of the system, and eventually help construct reliable space weather models in other planetary environments, particularly by taking into account multifractality, predictability, and hopefully extreme values.

3.2. Terrestrial foreshock transient structures and particle diffusion

In recent years it has become increasingly clear that the Earth's bow shock (Ness et al., 1964) and foreshock (Eastwood et al., 2005) are not just regions that process the solar wind (SW) but that they play a vital role in the formation of certain types of space weather phenomena.

These have been observed to occur in the absence of any large-scale SW perturbations, such as interplanetary coronal mass ejections, stream interaction regions, or interplanetary shocks (e.g., Gosling et al., 1991).

Different kinds of mechanisms have been invoked to explain certain types of magnetospheric transient perturbations, such as Pc1-5 pulsations and aurorae that occur during periods of quiet SW conditions. Those mechanisms involve the formation of transient upstream mesoscale structures (TUMS) upstream of the bow shock of the Earth. These structures form either due to intrinsic foreshock processes or due to interactions of directional discontinuities (DD, e.g., Borovsky, 2008) of the interplanetary magnetic field (IMF) with the bow shock and the foreshock region.

It has been shown that the larger-scale TUMS exhibit large variations of total pressure inside them and that this leads to the local deformation of the magnetopause and the precipitation of the particles into the ionosphere. In the following, we briefly describe each of the structures and their contribution to space weather.

In this paper, we will only focus on small- and mid-scale phenomena at the bow shock. It is worth noting that it is important to consider also large-scale interactions and the current system at planetary bow shocks (Lopez, 2018; Dredger et al., 2023). The planetary bow shock is always a generator, extracting kinetic energy from the solar wind and converting it into electromagnetic energy. On the bow shock in front of a planetary magnetosphere a current flow arises due to the curl of the interplanetary magnetic field across the shock. The closure of the bow shock current system remains an open question. A recent event studied by Dredger et al. (2023) using simultaneous observations from *MMS*, *AMPERE*, and *DMSP* satellites provided evidence for a partial closure of bow shock current through the Earth's ionosphere.

3.2.1. Foreshock cavitons and spontaneous hot flow anomalies

Foreshock cavitons (Fig. 10a) are structures that form in the portion of the foreshock permeated by compressive and transverse ultra-low frequency (ULF) waves (Omidi, 2007; Blanco-Cano et al., 2009; Blanco-Cano, 2010). Non-linear interactions of both types of waves result in the formation of localized regions characterized by cores of strongly diminished plasma density and magnetic field (~50% on average, see Kajdič et al., 2013) that are surrounded by rims in which both quantities exhibit enhanced values. Foreshock cavitons may have very structured interiors, they propagate sunwards in the reference frame of the SW plasma, but are convected towards the bow shock by the SW (Kajdič et al., 2011). Wang et al. (2020) showed that the velocity of cavitons in the SW frame is anticorrelated with their size. Statistical analysis of these structures (Kajdič et al., 2013) showed that plasma and magnetic field magnitude variations inside the cavitons are highly correlated, that their average duration in the spacecraft data is ~65 s, and that their extents range between 1 R_E and 13 R_E with the average value being 4.6 R_E. Foreshock cavitons are observed for a wide range of IMF and SW parameters, but preferentially form for higher magnetic field strengths, SW velocities, Alfvén speeds, and for smaller plasma densities when compared to average SW properties. Since foreshock cavitons are carried towards the bow shock, they may act as a "moving wall" in the second-order Fermi acceleration process of suprathermal ions (Omidi et al., 2021).

As foreshock cavitons approach the bow shock, they interact with it in such a way that the ions in the core of the cavitons are further energized and the plasma density and magnetic field magnitude are further reduced, leading to their increase in the outer parts and thus to the formation of spontaneous hot flow anomalies (SHFAs, Zhang et al. (2013), Omidi et al. (2013), see also Fig. 10b).

In their statistical study of simulated SHFAs, Tarvus et al. (2021) showed that foreshock cavitons form at distances up to ~11 R_E from the bow shock and that their transition into SHFAs takes place within ~2 R_E upstream of the shock. These authors also found that only a third of the cavitons evolve into SHFAs.

Kajdič et al. (2017) showed that SHFAs exhibit cores in which the B-field and plasma density are diminished by 90 % on average and that their average duration in the spacecraft data is about 1 min. Inside SHFAs the SW flow is highly decelerated and deflected from the radial direction (Zhang et al., 2013). Blanco-Cano et al. (2018) performed a statistical study of SHFAs and their interaction with the bow shock in hybrid simulations. These authors found that SHFAs may survive the shock crossing into the downstream region. They can cause shock erosion and lead to the formation of magnetosheath cavities (Katırcıoğlu et al., 2009).

Further studies are needed to show whether foreshock cavitons and SHFAs can be geoeffective and whether they cause any space weather phenomena.

3.2.2. Foreshock compressional boundaries

The compressive ULF waves accumulate on at least one edge of the ULF wave foreshock, leading to the formation of foreshock compressional boundary (FCB, Omidi et al. (2009, 2013), Rojas-Castillo et al. (2013b,a), see Fig. 10c). These structures represent boundary regions that separate the highly disturbed ULF wave foreshock from either the pristine SW or the section of the foreshock populated by field-aligned ion beams (FAB, Schwartz and Burgess, 1984) but not the ULF waves. FCBs are characterized by a highly correlated increase of magnetic field magnitude and density (by ~40% on average) that is followed by strong decreases of these two quantities on the foreshock side. Inside FCBs the SW velocity decreases by ~10% on average. Omidi et al. (2013) and Kajdič et al. (2017) have reported that FCBs also form on the edges of traveling foreshocks.

It has been shown by Hartinger et al. (2013) that FCBs may cause perturbations of the geomagnetic field. This occurs due to variations of total pressure inside FCBs which cause local, traveling magnetopause distortions and transient fluctuations of the geomagnetic field magnitude. Changes in the orientation and location of the foreshock and the corresponding FCB result in propagation of such magnetospheric fluctuations.

3.2.3. Foreshock cavities

Foreshock cavities or traveling foreshocks (Fig. 10d) appear upstream of the bow shock, either in pristine SW or in the region of the ion foreshock that is not perturbed by the 30-second waves. They form when a bundle of magnetic field lines from a relatively thin magnetic flux rope connects to the nominally quasi-perpendicular bow shock in such a way that the shock's geometry is locally changed to quasi-parallel (Schwartz et al., 2006; Billingham et al., 2008, 2011; Kajdič et al., 2017; Ala-Lahti et al., 2021). As the flux tube is convected by the SW, its intersection with the bow shock propagates along the bow shock surface. Upstream of it, a foreshock is formed that follows this intersection.

There are several ways that traveling foreshocks can cause disturbances in the magnetosphere and the atmosphere. Their interiors exhibit pressure variations which have been shown to drive magnetospheric Pc1 waves, accompanied by electromagnetic ion-cyclotron (EMIC) wave activity in the dayside magnetosphere (Suvorova et al., 2019). Concretely, traveling foreshocks caused ground Pc1 pearl pulsations of long duration (~1 h) in the morning side. These pulsations were accompanied by short-time magnetic field compressions and EMIC wave activity observed by satellites in the dayside magnetosphere.

Traveling foreshocks exhibit the same phenomena as the "regular" foreshock, namely ULF waves, FCB, etc. As such, the ULF waves inside the traveling foreshocks may be an important source of the magnetospheric Pc3 and Pc4 waves (10-45 s or 100-22 mHz and 200-20 s or 5–50 mHz, e.g., Jacobs et al., 1964; Troitskaya et al., 1971; Greenstadt and Olson, 1977; Russell et al., 1983; Engebretson et al., 1987).

Finally, Sibeck et al. (2021) and Kajdič et al. (2021a) showed that the foreshock cavities are directly transmitted into the magnetosheath and may cause the formation of magnetosheath jets (e.g., Plaschke et al., 2018) downstream of the quasi-perpendicular bow shock which is important since it has been demonstrated that magnetosheath jets can be geoeffective (see Plaschke et al., 2018, and the references therein).

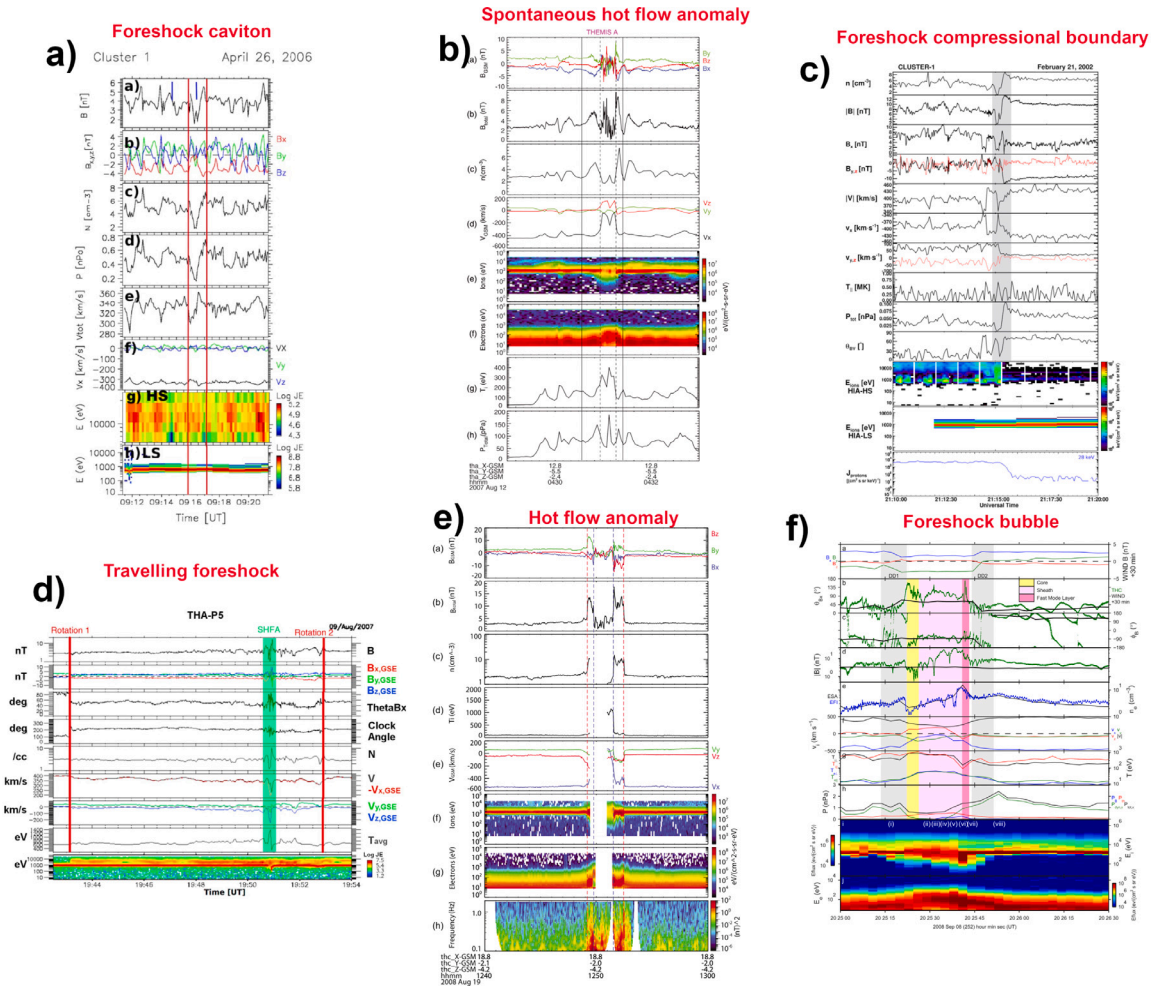

Fig. 10. Examples of (a) a foreshock caviton (adapted from Kajdič et al., 2013), (b) SHFA (adapted from Zhang et al., 2013), (c) FCB (adapted from Rojas-Castillo et al., 2013b), d) traveling foreshock (adapted from Kajdič et al., 2017), e) HFA (adapted from Zhang et al., 2013) and f) FB (adapted from Archer et al., 2015).

3.2.4. Hot flow anomalies

Hot flow anomalies (HFAs, Schwartz et al., 1985; Thomsen et al., 1986; Burgess and Schwartz, 1988; Thomsen et al., 1993; Schwartz, 1995; Jacobsen et al., 2009, see also Fig. 10e)) form when an interplanetary current sheet intersects the bow shock and the convection electric field ($-\mathbf{V}\times\mathbf{B}$) points towards it on at least one side. They are characterized by central cores that contain hot plasma flowing much slower than the ambient SW and is highly deflected from the Sun–Earth line. The plasma density and magnetic field values in the core are lower than in the SW. The core is surrounded by a rim in which magnetic field strength and plasma density are enhanced. Typical HFA extensions range between 1 and 3 R_E in the direction perpendicular to the corresponding current sheet, but they have been observed by Chu et al. (2017) to extend up to 7 R_E upstream of the bow shock.

HFAs were reported to have several effects on the near-Earth environment. They may cause strong displacements of the magnetopause (Sibeck et al., 1999; Sitar et al., 1998; Jacobsen et al., 2009; Šafránková et al., 2012) and magnetopause surface modes (Hartinger et al., 2013; Shen et al., 2018). Local magnetospheric disturbances were also observed (Sibeck et al., 1999; Sitar et al., 1998; Shen et al., 2018), as well as magnetospheric Pc3 (Eastwood et al., 2011; Zhao et al., 2017) and Pc 5 (Hartinger et al., 2013; Shen et al., 2018) pulsations. Additionally it has been shown by Jacobsen et al. (2009) that HFAs may lead to generation of field-aligned currents traveling convection vortices (e.g., Glassmeier et al., 2001; Kataoka et al., 2002) and certain types of auroras (Sibeck et al., 1998, 1999; Borodkova et al., 1998).

3.2.5. Foreshock bubbles

Foreshock bubbles (FBs, Omidi et al., 2010; Turner et al., 2013; Liu et al., 2016, see Fig. 10f)) form due to the interaction of IMF rotational discontinuities with the backstreaming ions in the foreshock region. If the convection electric field on the upstream of the rotational discontinuity has a larger earthward component than the electric field on its downstream side, foreshock ions are concentrated on the upstream side. These ions become hotter and start to expand against the SW, forming the bubble. The FBs exhibit signatures in the spacecraft data that are similar to those of HFAs, namely a hot, tenuous core with low IMF values that is surrounded by a rim where the latter two quantities are enhanced. FBs may affect the magnetopause on larger scales than HFAs since their transverse sizes are larger ($5–10 R_E$).

The FBs can be highly geoeffective (Hartinger et al., 2013; Archer et al., 2015). They can cause several phenomena, such as outward motion of the magnetopause, magnetopause undulations, transient variations of the geomagnetic field at geosynchronous orbits, and Pc5 pulsations. Archer et al. (2015) showed that FBs have a global impact on Earth's magnetosphere. These authors studied an event that was detected by ground-based magnetometers simultaneously across 7 h of magnetic local time.

Omidi et al. (2021) showed that FBs are associated with the presence of energetic ions and electrons and that their cores are filled with high energy particles. Ion energization at FBs takes place through the reflection of sunward moving particles through one or more collisions consistent with second-order Fermi acceleration.

3.3. Terrestrial magnetosheath jets and mirror-mode storms

The terrestrial magnetosheath is a region of space located between the Earth's bow shock and the magnetopause. It contains shocked solar wind plasma which has been decelerated, compressed, and heated by the bow shock. This is a highly disturbed environment populated by low frequency waves (Schwartz et al., 1997), turbulence (Rakhmanova et al., 2021) and transient structures (Plaschke et al., 2018). It is important to understand these phenomena since they can affect the geomagnetic field and be a source of certain space weather events. In this section, we will discuss briefly the characteristics of some wave modes and of small-scale transient structures known as magnetosheath jets (Plaschke et al., 2018). A recent in-depth review addressing the large-scale morphology of the magnetosheath can be found in Narita et al. (2021).

The magnetosheath is magnetically connected to the bow shock, thereby the local shock properties have a large influence on the properties of the downstream plasma. The level of fluctuations depends on shock geometry characterized by the angle between the local shock normal and the upstream IMF, θ_{Bn}.

Ion heating through the quasi-perpendicular bow shock occurs in such a way that the downstream plasma exhibits strong temperature anisotropy with $T_{perp} > T_{par}$ (Denton et al., 1995). This anisotropy makes the plasma unstable leading to the growth of ion cyclotron (IC) and mirror mode waves (MMW) (Gary, 1993). The two modes have been studied observationally by Fuselier et al. (1991) and Anderson and Fuselier (1993), who showed that IC fluctuations arise preferentially in the low-beta ($\beta \ll 1$), highly anisotropic plasmas, while mirror mode waves are more likely to be observed in the higher-beta ($\beta \geq 1$) plasmas with smaller anisotropy. These results have been corroborated using linear-Vlasov theory under magnetosheath-like conditions (Gary et al., 1993).

Mirror modes are non-propagating compressional waves with anticorrelation between magnetic field and plasma density (Hasegawa, 1969), they have periods of around 20 s (Lacombe et al., 1992). Mirror modes can be observed as isolated structures characterized by dips in the magnetic field magnitude, or as what is known as a mirror mode storm (Russell et al., 2009), which are long time intervals populated by many mirror mode waves.

Downstream of the quasi-parallel shock ($\theta_{Bn} < 45°$) the ions exhibit energies of up to ~30 keV and the plasma temperature anisotropy tends to be ~1. The plasma and IMF are characterized by much more intense and larger-amplitude fluctuations than downstream of the quasi-perpendicular shock ($\theta_{Bn} > 45°$). This occurs partly due to foreshock wave activity which is transmitted downstream. It has been shown by Kajdič et al. (2021) that, depending on the shock's Alfvénic Mach number M_A and θ_{BN}, the spectra of fluctuations in the quasi-parallel magnetosheath may be featureless and hence turbulence-like or they may exhibit bumps at frequencies similar to those in the upstream foreshock region.

In addition to plasma and IMF fluctuations, transient structures, known as magnetosheath jets (Plaschke et al., 2018) are often observed in the quasi-parallel magnetosheath. They are identified as transient enhancements of P_{dyn} or some related quantity which may reach values above those in the upstream SW. This occurs due to the enhancement in plasma density or velocity or both. Most of the jets are found in the quasi-parallel magnetosheath (Němeček et al., 1998; Archer and Horbury, 2013; Plaschke et al., 2013; Vuorinen et al., 2019), nonetheless recent studies have shown that jets can also be observed downstream of the quasi-perpendicular shock (Sibeck et al., 2021; Kajdič et al., 2021; Blanco-Cano et al., 2023).

The origin of magnetosheath jets in the quasi-parallel magnetosheath is an open question. It is possible that jets may be generated by different mechanisms (Plaschke et al., 2018). The most accepted ones are: a) generation at the quasi-parallel shock due to its inherent rippled surface (Hietala et al., 2009; Plaschke et al., 2013; Preisser et al., 2020), b) due to the interaction of interplanetary magnetic field (IMF) discontinuities with the bow shock (Archer et al., 2012), c) due to hot flow anomalies impact in the shock (HFAs, Savin et al., 2012), d) due to transmission of short large amplitude magnetic structures (SLAMS) or SW plasmoids into the magnetosheath (Karlsson et al., 2012, 2015, 2016), e) due to a combined effect of upstream plasma wave evolution and an ongoing reformation cycle of the bow shock (Raptis et al., 2022), and f) due to magnetic reconnection in the shock transition region (Preisser et al., 2020).

Jets in the quasi-perpendicular magnetosheath are much more rare and their origin has only been studied recently in a systematic manner. Kajdič et al. (2021) have shown that causes of jets in the quasi-perpendicular magnetosheath include transmitted foreshock cavities, non-reconnecting current sheets, reconnection exhausts, and mirror-mode waves. Blanco-Cano et al. (2020) and Blanco-Cano et al. (2023) also studied jets in the quasi-perpendicular magnetosheath and added flux transfer events as additional sources of jets there.

The study of jets has become very important because these events can modify the magnetosphere, leading to various phenomena in the geomagnetic environment: They can launch surface (Archer et al., 2019) or compressional (Plaschke et al., 2009) waves in the magnetopause. A recent study by Wang et al. (2022) showed that ground ULF waves can be triggered by them. Jets have also been related to reconnection (Hietala et al., 2018; Ng et al., 2021), and can lead to plasma entry into the magnetosphere (Karlsson et al., 2012; Dmitriev and Suvorova, 2015). Additionally, Han et al. (2017) "throat" auroras and an additional ionization of the ionospheric E and F1 layers (Dmitriev and Suvorova, 2022) have also been reported to be caused by jet interaction with the magnetopause.

Recent studies have shown that jets and mirror mode waves can co-exist in the quasi-perpendicular magnetosheath (Blanco-Cano et al., 2020), what is more sometimes mirror mode waves have been observed inside the jets (Kajdič et al., 2021; Blanco-Cano et al., 2023). Due to space, we will only address jet's relation to mirror modes. The recent manuscript of Krämer et al. (2023) provides a study of waves inside jets with frequencies between 0 to 4 kHz, as well as a complete list of references of previous works studying waves inside jets.

Fig. 11 shows an example of a jet studied in Blanco-Cano et al. (2023) for which the pressure enhancement is due to density and velocity increments that last for 110 s. The magnetic field inside the jet has a complex structure with a rotation in all components, compressive fluctuations, and a decrement of around 80 % at the center of the jet. MMWs are observed before and after the jet. During the whole interval an anisotropy in temperature ($T_{perp}/T_{par} > 1$) was observed and the plasma was unstable to the mirror mode except inside the jet. The MMWs permeate a large and continuous (~ 2 h) region of the magnetosheath, and can be classified as a mirror mode storm (Russell et al., 2009). Due to the rotation in the magnetic field, the origin of this jet has been related to a traveling foreshock (see previous section).

Fig. 12 shows an interval observed by MMS where two jets were found in a region with mirror mode waves. What is more, the strong compressive magnetic fluctuations are in anti–phase with the density and are identified as MMWs. The enhancement of dynamic pressure for these two jets is mainly due to an increment in velocity, with a duration of 71 and 53 s respectively. As showed in Blanco-Cano et al. (2023) the plasma beta was very high during the whole interval with values above 10, favoring the growth of the mirror mode, which was unstable even inside the jets, in contrast to the previous example.

The three jets presented above were observed very near the magnetopause, future work should investigate the joint effect of the jets and the compressive fluctuations around them on wave generation at the magnetosphere (Archer et al., 2012; Plaschke et al., 2009), and other possible geomagnetic effects, like the Alfvén waves that can be detected by ground magnetometers (Norenius et al., 2021).

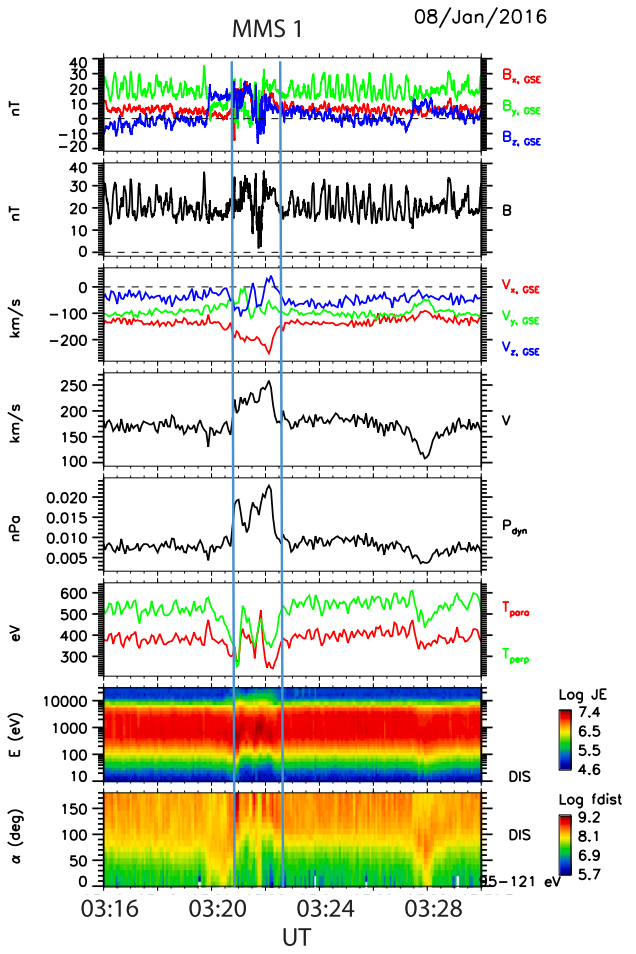

Fig. 11. MMS-1 data on January 16, 2016 showing an extended region with a mirror mode storm, where a jet is observed (delimited by vertical lines). Panels from top to bottom show components and magnitude of the magnetic field, components and magnitude of the velocity, dynamic pressure, perpendicular and parallel temperature, ion energy spectra, and ion pitch angle.

3.4. Terrestrial magnetopause Kelvin–Helmholtz vortices, magnetic reconnection, and magnetic flux ropes

The Kelvin–Helmholtz (KH) instability can grow along the low-latitude portion of the flank to tail magnetopause across which a substantial velocity shear exists. It can grow to form rolled-up vortices or overturned surface waves in a nonlinear phase (e.g., Hasegawa, 2012), and those generated under northward interplanetary magnetic field (IMF) conditions are believed to cause efficient transport of solar wind plasma into the magnetosphere through physical processes such as vortex induced magnetic reconnection (VIR) (e.g., Nakamura et al., 2017) and kinetic Alfvén wave turbulence mode-converted from the KH surface waves (Chaston et al., 2007). VIR generally occurs at the trailing (sunward-facing) edge of nonlinear KH vortices towards which plasma flows from the magnetospheric and magnetosheath sides of the magnetopause interface converges and thus current sheets can be compressed or where magnetic shear (i.e., a current sheet) is generated through three-dimensional (3D) deformation of magnetic field lines by vortical flows (e.g., Nakamura et al., 2013). If such VIR occurs at multiple sites on the tailing surface, magnetic flux ropes can be generated. There is indeed ample evidence for such KH-associated flux ropes, first from THEMIS spacecraft observations (Eriksson et al., 2009; Nakamura et al., 2013) and most recently from the Magnetospheric Multiscale (MMS) mission (Hwang et al., 2020).

Fig. 13 shows a schematic that summarizes MMS observations of a flux rope on the KH-active dawn flank magnetopause during a northward IMF period. Interestingly, two bundles of the reconnected field lines from VIR were entangled three dimensionally inside the flux rope. This presumably led to the formation near the flux rope center of another thin current sheet that can become subject to secondary local reconnection (Hwang et al., 2020; Kieokaew et al., 2020). Such 3D reconnection sequentially induced during the course of the KH instability, including a particular type of 3D VIR called midlatitude reconnection (Faganello and Califano, 2017, see also Fig. 13b), may lead to enhanced plasma transport, as suggested by Nakamura et al. (2017).

The occurrence pattern of the KH vortices such as the IMF dependence (Kavosi and Raeder, 2015) and seasonal variations (Kavosi et al., 2023) has been investigated statistically based on a combination of long-term observations, for example, by THEMIS, and methods to identify and analyze KH vortices in in-situ data (e.g., Hasegawa, 2012; Cai et al., 2018). It is now known that the magnetopause KH instability can grow for southward as well as northward IMF conditions (Hwang et al., 2011; Kavosi and Raeder, 2015). One of the key differences between the KH vortices under southward and northward IMF conditions is that those under southward IMF tend to have more irregular structures (Hwang et al., 2011) and may decay more rapidly, because of stronger interaction between the KH instability and magnetopause reconnection with high magnetic shear (unrelated to VIR) for such conditions (Nakamura et al., 2020). Another characteristic feature of the KH instability under southward IMF is that because a thin density gradient layer often exists in the magnetopause boundary layer for such conditions, the lower-hybrid drift instability (LHDI) can also be excited and may couple with the KHI instability. In 3D, such coupling can induce low-shear reconnection in the boundary layer (in addition to standard high-shear reconnection at the magnetopause), which may augment plasma mixing associated with particle diffusion in the LHDI turbulence (Nakamura et al., 2022).

MAVEN spacecraft observations at Mars showed that flux ropes can be formed through interaction between the crustal and interplanetary magnetic fields (Hara et al., 2017), and KH vortices can grow in a boundary region between the magnetosheath and the magnetic pileup region above the ionosphere (Ruhunusiri et al., 2016). Both flux ropes and KH vortices are suggested to be agents for enhanced loss of atmospheric/ionospheric materials from the space environment of unmagnetized or weakly magnetized planets (e.g., Terada et al., 2002). However, little is known about their interrelationship and how they could interact with each other at Mars. Questions that may be addressed in future investigation/measurements at Mars include: whether flux ropes and vortices can be observed simultaneously; whether they coexist or are displaced in space; and what are the effects of their possible interaction on atmospheric escape.

3.5. Terrestrial magnetotail

The contemporary widely accepted view on magnetospheric dynamics is based on the concept of reconnection (see Hesse and Cassak (2020) for an extensive review about the role of the magnetic reconnection in the Space Science). It was applied for the first time to the magnetosphere by Dungey (1961) to explain plasma entry from the solar wind and magnetospheric convection. However, considering the limitations of his model, he further stated that *"the flow is probably turbulent, particularly in the "wake" of the earth, and both Pioneer I and Explorer I observations show clear indications of some hydromagnetic form of turbulence"* (Dungey, 1962).

However, it was only in the 1980s that substantial evidence regarding various aspects of turbulence in the central region of the tail, known as the plasma sheet, began to accumulate. For instance, summarizing data from electric field measurements in the auroral region and the results of high apogee satellite observations, Antonova

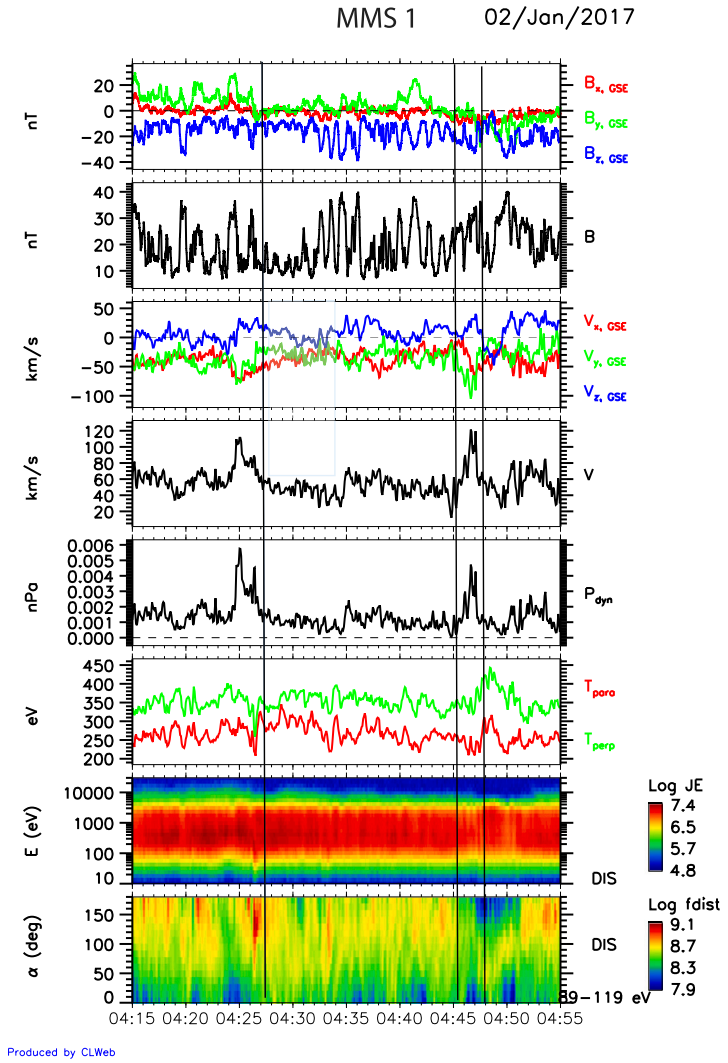

Fig. 12. MMS-1 data on January 2, 2017 showing an extended region with mirror mode waves, where two jets are observed (delimited by vertical lines). Panels are in the same format as Fig. 11.

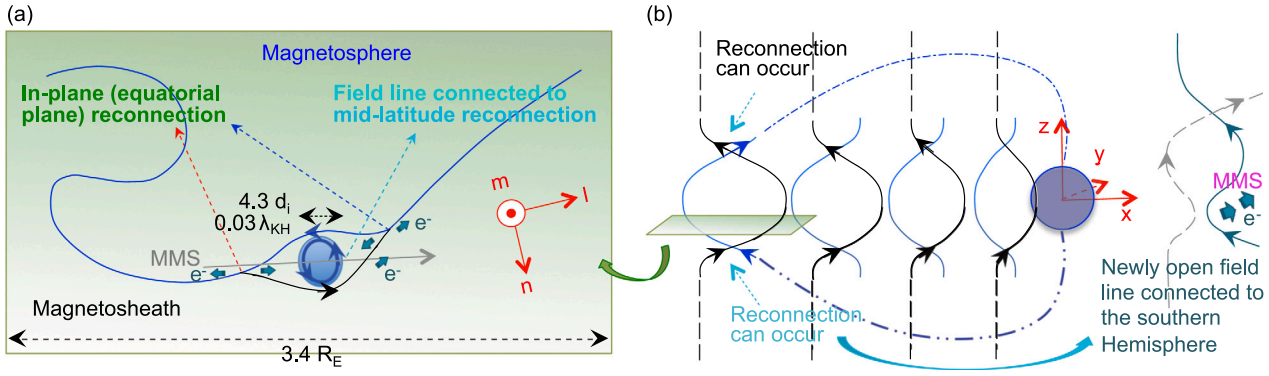

Fig. 13. Schematics of (a) a near-equatorial Kelvin–Helmholtz vortex with a magnetic flux rope at the trailing surface observed by the MMS mission, as viewed from north, and (b) possible magnetic topology of the magnetospheric (blue curves) and magnetosheath field lines (black) before (left) and after (right) vortex induced midlatitude reconnection (marked by cyan arrows), as viewed from dawn. (For interpretation of the references to color in this figure legend, the reader is referred to the web version of this article.)
Source: Adapted from Hwang et al. (2020)

(1985) inferred that the plasma sheet exhibits turbulent behavior. As a result, she argued that this turbulence would result in the significant plasma mixing. At around the same time, Montgomery (1987) also pointed out that the plasmas of the Earth's magnetotail should not behave in a laminar-flow fashion due to the high fluid and magnetic Reynolds numbers in the plasma sheet. In the late 1990s, Borovsky et al. (1997) published the first experimental study on turbulent flows in the Earth's plasma sheet, which revealed that these flows exhibited

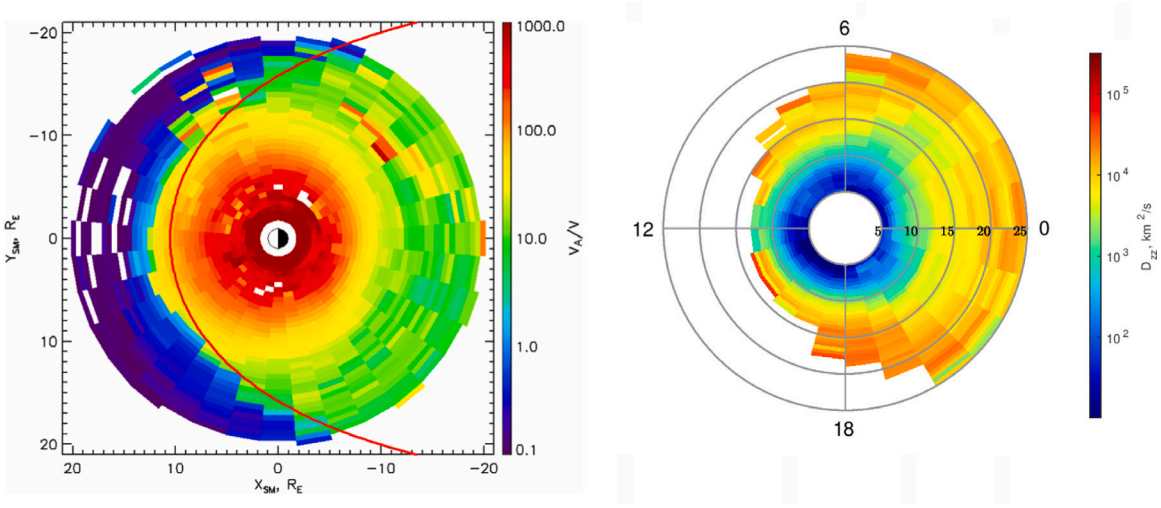

Fig. 14. Comparison between (a) Ratio between Alfvén and bulk velocities adapted from Antonova et al. (2023) and (b) Eddy diffusion coefficients, plotted using Stepanova et al. (2011) dataset.

unpredictable and random fluctuations, with amplitudes significantly larger than the mean flow velocities. They also obtained probability distributions and autocorrelation times of flow velocity, concluding that the observed properties correspond to magnetohydrodynamic (MHD) turbulence. Later, Borovsky and Funsten (2003) established that the observed turbulence is primarily formed by eddies. They determined that the typical scale of these eddies ranges from 4000 to 10000 km and may even be larger, with a mean value near 1.6 R_E. Subsequently, Keika et al. (2009), Keiling et al. (2009), and Panov et al. (2010) observed plasma vortices of such scales using data from the THEMIS mission. The turbulent flows in the magnetotail with eddies of a similar size also appear during the 3D MHD simulations of the global magnetosphere (El-Alaoui et al., 2010).

However, despite all the efforts and achievements mentioned above, the mechanisms for the formation of turbulence in the plasma sheet remain unclear and continue to be a topic of discussion. Several physical processes contribute to the generation of turbulence at different scales. For example, Antonova (2002) suggested that plasma pressure gradients are the most suitable candidates for the generation of the dawn–dusk electric field and hence large- and medium-scale harmonics of magnetospheric turbulence. Recently, Antonova and Stepanova (2021) reviewed the paradigm of the geomagnetic tail as a turbulent wake behind an obstacle and examined the role of turbulence on the MHD scales in plasma transport and mixing. Based on their findings, they proposed that the large-scale two-vortex magnetospheric convection generated by the magnetospheric plasma pressure gradients is a source of energy for turbulence development and possibly the driving or integral vortex of such turbulence.

El-Alaoui et al. (2010) described a method to couple the large-scale drivers of MHD turbulence to the local kinetic scales, suggesting the appearance of resistivity in the regions with high local currents as a source of dissipation that contributes to plasma sheet turbulence in two ways. First, on a large scale, it causes reconnection, which drives turbulent flows, and secondly, it dissipates energy on smaller scales. They also considered the influence of the Kelvin–Helmholtz instability along the flank boundaries.

Many properties of plasma sheet turbulence were determined by analyzing magnetic field fluctuations (Vörös et al., 2004; Weygand et al., 2010). In particular, comparison of the autocorrelation times of velocity fluctuations (2 min, e.g.,Borovsky et al. (1997) to the timescale of magnetic field fluctuations (8 min, e.g., Troshichev et al. (2002)) shows an inconsistency even for the distant plasma sheet. This indicates that plasma sheet turbulence is probably not pure MHD turbulence, and electrostatic modes could dominate at medium and small scales. This is an expected result considering that in collisionless plasmas, electrostatic modes develop more easily than electromagnetic ones.

Nonetheless, even for large scales the applicability of a hydrodynamic approach is not evident. The use of the ideal MHD is restricted to the fast plasma flows only. It is well known that the Hall term in the generalized Ohm's law can be neglected only for the scales $\gg L_{Hall} = \lambda_i V_A/V$, where $\lambda_i = c/\omega_{pi}$ is the ion inertial length, ω_{pi} is the ion plasma frequency, c is the speed of light, V_A is the Alfvén speed (see, for example, Priest and Forbes (2000)). Indeed, analysis of Antonova et al. (2023) showed that – in difference with the solar wind – the ratio between the Alfvén and flow velocities in the Earth's magnetosphere is too high to guarantee the unrestricted use of the frozen-in approximation. If we compare these results with the values of eddy diffusion coefficients obtained by Stepanova et al. (2011) it is evident that the transition from turbulent to laminar regime takes place at approximately 12 R_E, where $V_A/V > 10$ (see Fig. 14).

This necessitates the development of a complex system approach based on fundamental principles of plasma physics. The model of the plasma sheet should include the total pressure balance, which is valid even in the presence of turbulence. Antonova and Ovchinnikov (1999) successfully applied this approach to explain the stability of the turbulent plasma sheet (see also Stepanova et al. (2011)). Further development of these ideas would allow us to create a model that includes different types of turbulence and other phenomena observed in the tail, such as bursty bulk flows forming part of an intermittent turbulent cascade.

3.6. South Atlantic magnetic anomaly

3.6.1. The Earth's magnetic anomaly

The South Atlantic Anomaly (hereafter, SAA) is the minimum intensity of the geomagnetic field located in the South Atlantic Ocean, extending from Africa to South America (Fig. 15).

Several scenarios have been proposed to understand how the SAA was formed. One of the most recent interpretations is the theory of the flux expulsion (Tarduno et al., 2015): it is the response of the inverse geomagnetic flux patch at the Core–Mantle Boundary (CMB) of the radial component of the Earth's magnetic field, which is located approximately under the South Atlantic Ocean. Such an effect could generate the hemisphere asymmetry of the realistic Earth's magnetic field. A reduced seismic wave anomaly identifies the CMB under the South of Africa called the African Large Low Shear Velocity Province (LLSVP).

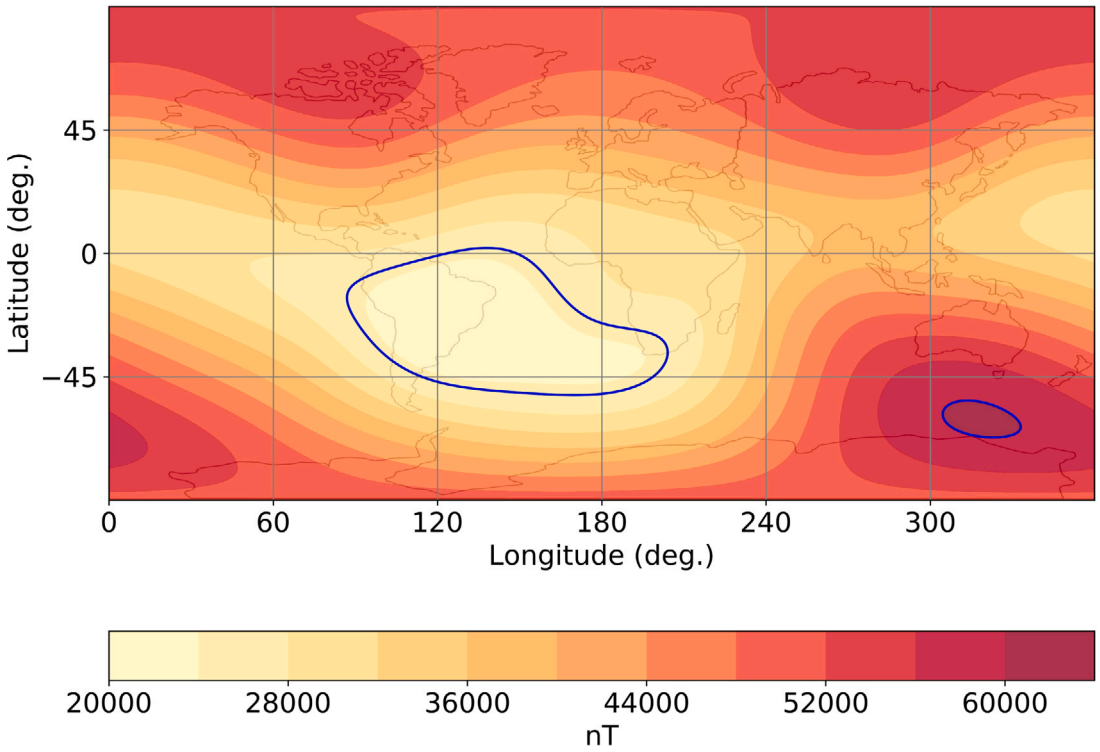

Fig. 15. The geomagnetic field intensity map at 200 km computed by IGRF-12 model. The two blue contour edges represent the locations of the maximum and the minimum magnetic field. (For interpretation of the references to color in this figure legend, the reader is referred to the web version of this article.)

The SAA research regroups different fields of disciplines: geomagnetism, particle physics, radiation physics, space engineering, etc.

The history of the evolution of the Earth's magnetic field is essential to predict the possible scenarios of the Earth's destiny in response to the sun's activity.

Huge efforts were devoted to develop several geomagnetic field models, from which we understood that the size and the shape of the SAA changed significantly over the years such as Cnossen and Matzka (2016) and Thébault et al. (2015).

The Earth possesses a strong magnetic field; thus, particles gyrate, bounce, and drift along the geomagnetic field lines. As the SAA is the location of the minimum magnetic field intensity, the mirroring altitudes of the inner radiation belt particles are reduced. Consequently, more particles have access to the anomaly zone, forming a localized particle flux. Since the geomagnetic field's variations to solar activity affect the particle dynamics, both magnetic and particle responses of the SAA could be accordingly varied.

The SAA influences the performance of the Low-Earth Orbit (LEO) missions. Generally, the onboard instruments are sensitive to particle collisions propagating inside the slabs of the spacecraft shielding. The more the probability events of the heavy and energetic particle striking, the more the damage could affect temporarily or permanently the device operation. The long-term absorbed radiation doses and the abrupt Single Event Effects (SEE) are predicted to design the spacecraft shielding and the device sensitivity.

The implication of the space weather on the SAA is considerable. The Earth's inner magnetosphere is affected by the solar wind interaction with the magnetosphere in long-term variations, e.g., solar cycles ≈ 11 years, and short-term variations, e.g., geomagnetic storms ≈ hours and days. For instance, Qin et al. (2014), Girgis and Hada (2018), Girgis et al. (2020a) studied the magnetic field response of the SAA to long-term space weather variations. Moreover, Zou et al. (2011, 2015), Dachev (2018), Girgis et al. (2020b, 2021b, 2022a) investigated the particle flux response of the SAA due to geomagnetic storms (Figs. 16 and 17) and solar cycles.

Finally, Falguere et al. (2002), Girgis et al. (2021a, 2022b) examined the radiation effects of space missions due to their passages in the SAA during magnetic storms.

3.6.2. Martian magnetic anomalies

The terrestrial magnetic anomaly research approach can be similarly applied to understand in-depth the martian magnetic anomalies. Starting by the martian magnetic field modeling, e.g. Ma et al. (2015), Langlais et al. (2019), Gao et al. (2021), it is useful to unveil its earlier evolution, to anticipate its future, and to find out how Mars lost its magnetic field (if it had), which could be a terrifying scenario if it will occur to our planet. Although Mars does not possess an active or strong magnetic field like on Earth, instead, it possesses a remnant magnetic field; therefore, no particle could be trapped. However, the solar proton trajectories could be affected by the martian magnetic field. Fig. 18 visualizes the magnetic field intensity map of Mars at an altitude of 200 km. By comparing Fig. 15 with Fig. 18, the maximum magnetic field intensity of Mars is roughly one hundred times less intense than the Earth's magnetic field at the same altitude. According to Fig. 18, one major and two minor low magnetic field intensities are located in the northern and southern hemispheres respectively.

Therefore, the particle flux patches in the northern hemisphere are (roughly) more prominent. Such phenomenon was produced by Jolitz et al. (2021), who simulated the SEP electron precipitation at Mars and produced the resulting electron flux maps. Since the martian magnetic field is not homogeneous as on Earth, it is indispensable to produce the SEP proton and electron flux maps to design the martian space missions.

As the solar emission is the primary driver of the interplanetary space weather, it affects the charging and radiation environments of the spacecraft orbiting the planet. Regular space operations could be at risk because Mars does not possess a strong magnetic field capable of protecting the planet's vicinity from the solar energetic particles. Therefore, forecasting the martian space environment is necessary to design more adequately the spacecraft shielding to develop more reliable space missions and to mitigate the hazards of the high-level solar and cosmic radiation on the martian surface operations.

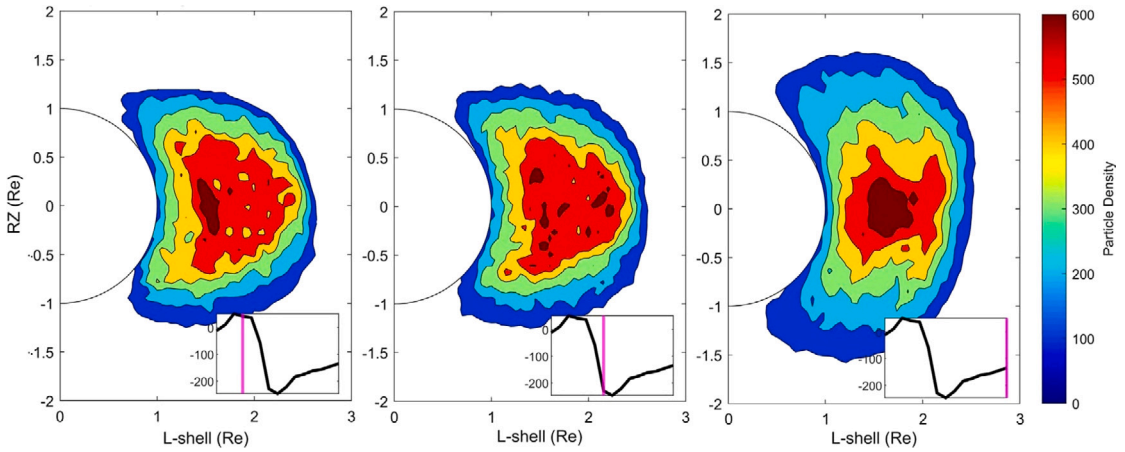

Fig. 16. Simulations of the inner proton belt density during the initial, main, and recovery phases of the geomagnetic storm of 15 May 2005 by Girgis et al. (2021b).

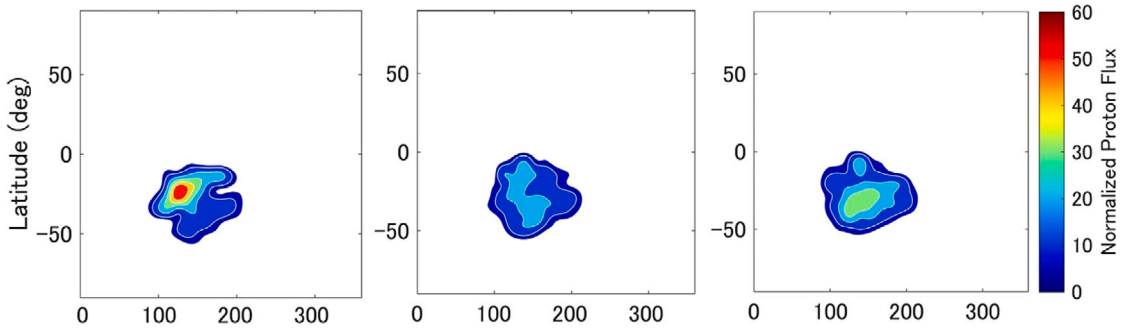

Fig. 17. The resulting proton flux maps of Fig. 16, from which we can observe the variations of the SAA proton flux during the geomagnetic storm by Girgis et al. (2021b).

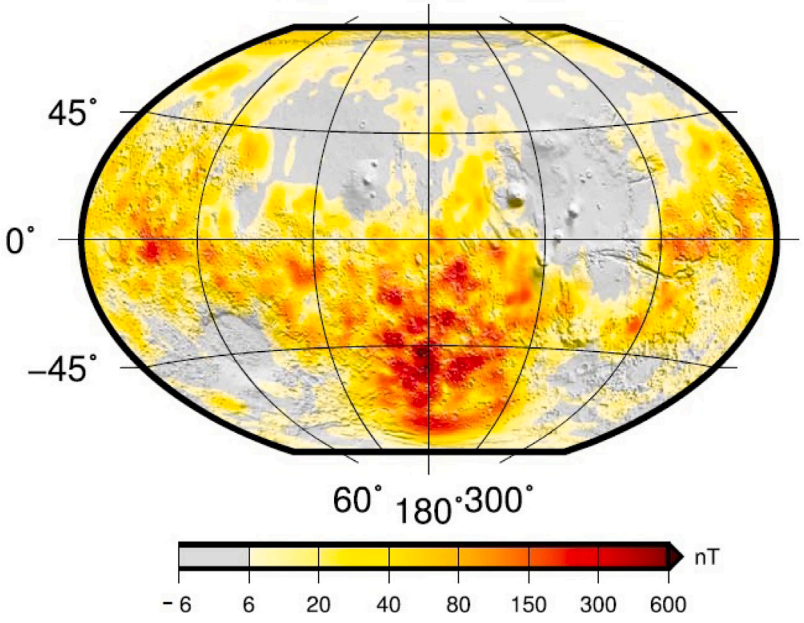

Fig. 18. The martian magnetic field intensity map at 200 km produced by Langlais et al. (2019).

4. Martian space weather, bow shock, and magnetosphere-ionosphere

4.1. Martian space weather, aurora, and ionosphere

Continuous monitoring of space weather at other planets is getting more and more attention in recent times thanks to current deployment of technology in our solar system. In the particular case of Mars, that is an essential aspect to consider in preparation for the future human exploration of the red planet, as communications between surface and orbiters are crucial and the amount of radiation reaching the surface significantly increases during major solar storms (Guo et al., 2021). Real-time forecast at Mars is challenging as we do not have continuous observations of Sun's irradiance, solar energetic particles or in-situ

upstream solar wind observations. While at Earth, dedicated upstream solar monitors such as ACE and WIND in combination with ground–based facilities and ionospheric–magnetospheric satellites changed our perspective of Space Weather and space physics in general, at Mars, this is not the case yet (Sánchez-Cano et al., 2022).

The main difference between Earth and Mars in terms of space weather is that the solar wind interaction is different with each planet. At Earth, the solar wind interaction with the ionosphere is an indirect mechanism because the solar wind first encounters Earth global magnetic field, creating the magnetosphere, which in turn is connected to the ionosphere through field-aligned-current systems. On the contrary, at Mars, the solar wind interaction with the ionosphere is a direct mechanism as the solar wind directly interacts with the high-altitude atmosphere and ionosphere, inducing a magnetosphere. This interaction at Mars is, however, not simple because of the presence of non-uniform magnetic crustal fields in a region of the surface of Mars. These fields are the remnant of a former dynamo in the planet, and they can be as strong as thousands of nanoteslas at 300 km. These fields rotate with the planet and have the capacity of interacting with the solar wind, creating a hybrid magnetosphere. In other words, Mars' magnetosphere has mixed-characteristics of both induced and intrinsic magnetospheres that also suffer changes along with the planet rotation.

The main result of the interaction between Mars' ionosphere and the solar wind is the creation of the hybrid magnetosphere with several plasma boundaries. The most external one is the bow shock, which contrary to Earth bow shock that is controlled by the solar wind dynamic pressure, at Mars the solar EUV flux is equally important, and so, the ionosphere (Hall et al., 2019). Thus, the bow shock location varies with the solar cycle and with seasons (as Mars' orbit is highly elliptical), being further away at the maximum of solar activity and at the perigee of Mars' orbit (Hall et al., 2016, 2019). Another key boundary is the magnetic pileup boundary (MPB), which is where strong, highly organized magnetic fields are found (Bertucci et al., 2004), and which thickness is of the order of an ion inertial length (Boscoboinik et al., 2020). The last boundary to be typically formed is the ionopause, which separates the cold and hot plasma populations within the ionosphere (Sánchez-Cano et al., 2020). However, its formation is sporadic because the ionosphere is mostly always magnetized as the consequence of a pressure unbalance situation between the thermal pressure of the ionosphere and the total pressure in the overlying MPB (Nagy et al., 2004).

The presence of crustal magnetic fields has a strong influence on the position of all these boundaries, which are highly dynamic and dependent on both internal and external drivers. As Garnier et al. (2022) pointed out a large-scale coupling between the crustal fields, the ionosphere and the boundary plays a dominant role in Mars' plasma dynamics. This is further observed every time that a space weather event takes places at Mars, such as after the impact of solar energetic particles or interplanetary coronal mass ejections, where atmospheric escape is highly enhanced, ionospheric scintillation occurs, or new ionospheric layers are created at low altitudes in Mars' atmosphere. The nightside is particularly affected, and it is a direct consequence of the induced magnetosphere tail, which is highly twisted (DiBraccio et al., 2018) due to the complex interaction of the interplanetary magnetic field, the draped field, and the crustal magnetic fields (Fang et al., 2015). As explained in Sánchez-Cano (2023), the different magnetic topology present in the Martian tail may be the reason for the high fluxes observed of electron precipitation in the tail, as well as the reason for the occurrence of radio HF blackouts or diffuse aurora at Mars during space weather activity.

Solar particle precipitation from large-scale solar transients often creates lower ionospheric layers both at Earth and Mars (between 60-90 km at both planets), in a region non-accessible to in-situ orbiter observations, significantly enhancing the absorption of radio HF signals passing through the region. While at Earth these layers last of the order of hours and are typically formed at high latitudes by precipitating protons (known as Polar Cap Absorption) or at all latitudes when solar flares ionize the dayside mesosphere, at Mars, they are particularly important because they typically last of the order of days and occur everywhere over the planet, day and night (Sánchez-Cano et al., 2019), and are created by solar electrons with minimum energy of 70 keV (Lester et al., 2022). It has strong implications for planetary exploration as these layers inhibit HF radio communications for several days, as well as are key to understand the transition region between the lower and upper atmosphere of Mars. Moreover, the same region of the ionosphere is also known to be susceptible to produce aurora emissions, which can be of different natures as described by Schneider et al. (2015, 2021). They can be discrete auroras that are typically found over regions of strong vertical crustal magnetic fields (Bertaux et al., 2005), diffuse auroras that are caused by global precipitation of solar energetic particles (Schneider et al., 2015), proton aurora that is caused by solar wind proton precipitation (Deighan et al., 2018), or sinuous aurora, which are often found far away from crustal fields, and whose origin is mostly unknown but believed to be related to the twisted configuration of the Martian tail (Lillis et al., 2022). From all of these emissions, the most important related to space weather is the diffuse aurora, which can become a global phenomenon during large events and last for several days (Schneider et al., 2018). It is important to note that these emissions originate from an altitude of about 60 km in the atmosphere, coincident with the altitude in which HF radio blackouts also occur during the same space weather events.

Another consequence is atmospheric escape, which is a major open question due to its implications on Mars' atmospheric evolution. It is known that space weather events, such as solar flares, can create also density enhancements in the expected ionospheric layers (Mendillo et al., 2006), and enhancements in atmospheric temperature (Thiemann et al., 2015). Coronal Mass Ejections can increase the motion of boundaries (Sánchez-Cano et al., 2017) and compress the magnetosphere up to near half of its size (Kajdič et al., 2021b). Especially important is the increase of the rate of atmospheric escape. For example, the loss rate of heavy ions from the planet is significantly enhanced (Futaana et al., 2008; Jakosky et al., 2015a), in addition to the trans-terminator flow that can be enhanced by several factors, even during the minimum of solar activity (Kajdič et al., 2021b), and as well as the hydrogen escape rate can meaningfully increase by several factors of magnitude through increases in the upper atmospheric temperature, having potential strong consequences on the evolution of Martian water loss over time (Mayyasi et al., 2018).

The ionosphere–atmosphere coupled system of Mars is the ultimate region where solar radiation is mostly dissipated (Guo et al., 2021), although under severe space weather events, large levels of radiation can reach the surface of the planet. As Guo et al. (2021) reported based on observations of the radiation detector of Mars Science Laboratory, over the time period of August 2012 to June 2020, the galactic cosmic ray dose rate at the surface of Mars increased by 50%, which is a much larger factor than dose rate measured at Earth surface. Moreover, five solar particle events were able to produce a surface radiation enhancement, being the largest one the September 2017 event, which was the largest event recorded at Mars of solar cycle 24. Since space weather radiation can be hazardous for any Mars mission, it is central that future exploration focuses on the importance of the role of the magnetosphere–thermosphere–ionosphere coupling under space weather conditions.

4.2. Martian induced magnetosphere

Mars does not possess a global, dynamo-generated magnetic field (Acuña et al., 1998). As a result, the solar wind interacts directly with the Martian atmosphere. This interaction results in the escape of planetary plasma as it receives the energy and momentum from the solar

wind (Jakosky et al., 2015b). Unlike completely unmagnetized planets such as Venus, Mars possesses regions with crustal magnetization whose fields can locally act as obstacles to the incoming flow (Connerney et al., 2001). However, crustal magnetic fields represent a second-order effect in the interaction (Nagy et al., 2004). Mars induced magnetosphere is preceded by a collisionless bow shock (Gruesbeck et al., 2018) that decelerates heats and compresses the solar wind plasma. Upstream from the shock, protons from the planet's exosphere generate waves at the local proton cyclotron frequency (Bertucci et al., 2003; Mazelle et al., 2004; Romanelli et al., 2016). The magnetosheath extends downstream from the shock. Here, the hot solar wind plasma transports a highly variable magnetic field. At the base of this region, the proximity of the planet's ionosphere and the exobase causes the solar wind plasma to decelerate and the frozen in interplanetary magnetic field piles up in front of the planet. The gradient in the magnetic field strength marks the presence of the magnetic pileup boundary (MPB), the outer edge of the induced magnetosphere. Other signatures of the MPB are the decrease in the level of fluctuations of the IMF and the onset of draping (Bertucci et al., 2003). The induced magnetosphere contains draped interplanetary magnetic field and to a minor extent (especially over the southern hemisphere) planetary crustal fields. These fields permeate a plasma that is for the most part of planetary origin. In the presence of collisions, the reconnection between planetary and interplanetary magnetic field lines provides channels for precipitating particles to produce aurorae (Schneider et al., 2015). On the nightside, the plasma and neutral dynamics near Mars is also permeated by hybrid magnetic fields. The mid-range tail follows the morphology resulting from the draping of the interplanetary magnetic field (Yeroshenko et al., 1990). Nevertheless, a twisting effect originating from the reconnection between planetary and interplanetary field lines is observed up to a few planetary radii downstream (DiBraccio et al., 2018). The far induced tail remains a poorly explored region. Mars interaction is strongly affected by the planet's changing heliocentric distance along its orbit. This introduces seasonal and secular changes in the size of the magnetosphere and the occurrence of phenomena such as the upstream waves which are in turn produced by the expansion of the planet's thermosphere. Another characteristic of the Martian magnetosphere is its size, which is comparable with the convective gyroradius of solar wind protons (Moses et al., 1988). This introduces kinetic effects that are exclusive to this induced magnetosphere.

4.3. Mesoscale transient structures upstream of Mars

In this section, we describe observations of transient upstream mesoscale structures (TUMS) detected upstream of Mars which form either due to intrinsic foreshock processes or due to the interaction of IMF directional discontinuities with either the bow shock or the backstreaming foreshock ions. It turns out that TUMS at Mars tend to exhibit smaller sizes than at Earth due to the smaller size of the Martian bow shock. Despite their size, TUMS may be an important source of space weather phenomena at Mars.

The foreshocks of Mars and Earth exhibit some similar phenomena (waves, ion populations, transient structures); however, there exist at least three fundamental differences between them: (1) Martian foreshock is much smaller than that of our planet. This is due to the fact that the Martian bow shock is also much smaller than that of the Earth. On average, its subsolar point lies only 1.6 R_M (~5400 km) from the Mars' center (Slavin and Holzer, 1981). As a consequence, ions reflected from the shock can travel significant distances along its surface, smearing the separation between its quasi-parallel and quasi-perpendicular sections (Moses et al., 1988). This means that a portion of Mars' foreshock may also be populated by ions reflected at the quasi-perpendicular section of the planet's bow shock, as has been shown by Madanian et al. (2023). (2) The ULF waves at Mars may occur due to different mechanisms. Apart from the interaction of the backstreaming ions with the incident SW particles, the ULF waves at Mars also form due to the presence of pick-up ions from Mars' hydrogen exosphere. Russell et al. (1990), for example, found evidence for such left-hand elliptically polarized waves in the foreshock of Mars. (3) The extended oxygen/hydrogen corona around the planet may have another effect: strong deceleration of the solar wind in the foreshock region. It was reported by Verigin et al. (1991) that the solar wind velocity in the foreshock of Mars diminishes by ~100 kms^{-1} (7-10 kms^{-1} at Earth, e.g., Bame et al., 1980).

Among the transient structures that have been observed upstream of Mars as well as Earth are the spontaneous hot flow anomalies (Collinson et al., 2017), foreshock cavities/traveling foreshocks (Collinson et al., 2020), hot flow anomalies (Øieroset et al., 2001; Collinson et al., 2015; Shuvalov et al., 2019) and foreshock bubbles (Madanian et al., 2023). In the following subsections, we briefly describe the observed properties of these phenomena in the near-Mars environment.

4.3.1. Spontaneous hot flow anomalies

Observations of a SHFA at Mars were first reported by Collinson et al. (2017, see Fig. 19a). The event lasted for ~11 s in the spacecraft data and was estimated to measure 7300 km or 2.3 R_M across. It was suggested that due to the low dynamic pressure inside this SHFA, the scale height of Martian topside ionosphere was changed from ~40 km to ~240 km, which means that these phenomena may have a strong impact on the ionosphere.

4.3.2. Hot flow anomalies

HFAs were the first transient upstream mesoscale structures observed upstream of Mars by Øieroset et al. (2001, see Fig. 19b) in the data of the Mars Global Surveyor (MGS) mission. The events exhibited typical HFA signatures, such as cores with turbulent magnetic field, low plasma density, and high electron temperature. No velocity measurements were provided, though.

Later, Collinson et al. (2015) observed an HFA upstream of Mars and determined its size to be 2200 km (0.64 R_M), which is much less than their typical sizes at Earth (~1-3 R_E). This is a direct consequence of the small size of the Mars' bow shock, due to which the current sheets associated with HFAs remain in contact with the shock only for ~3 min (~1 h at Earth) which gives them limited time to grow. This also means that the ion distributions inside HFAs at Mars are more similar to those inside "young" or "proto" HFAs at Earth (Zhang et al., 2010; Wang et al., 2013). Additionally, Collinson et al. (2015) showed that inside the core of the observed event, the solar wind dynamic pressure decreased from 410 pPa to 70 pPa, which could potentially disrupt the topside ionopause. A simple calculation showed that this event increased the ionopause height from ~40 km to ~110 km.

Shuvalov et al. (2019) performed a statistical study of HFAs upstream of the Mars' bow shock. In total, the authors selected 19 events and estimated that their occurrence rate was 0.6 ± 0.3 events per day. The HFA sizes were estimated to range between 0.2 R_M (~780 km) and tens of R_M.

4.3.3. Foreshock cavities

Foreshock cavities, a.k.a. traveling foreshocks at Mars have been reported by Collinson et al. (2020, see also Fig. 19c). The authors showed observations of a single event which was bounded by rims of enhanced IMF magnetic field magnitude and plasma density, while its core exhibited turbulent magnetic fields, lower plasma densities, and elevated ion and electron temperatures. There was one important difference between this event and its counterparts at Earth: the elevated temperatures inside foreshock cavities at Earth arise due to backstreaming ions that are reflected at the shock. In the case of the foreshock cavity at Mars, the temperature rise resulted from heating of the bulk SW ions.

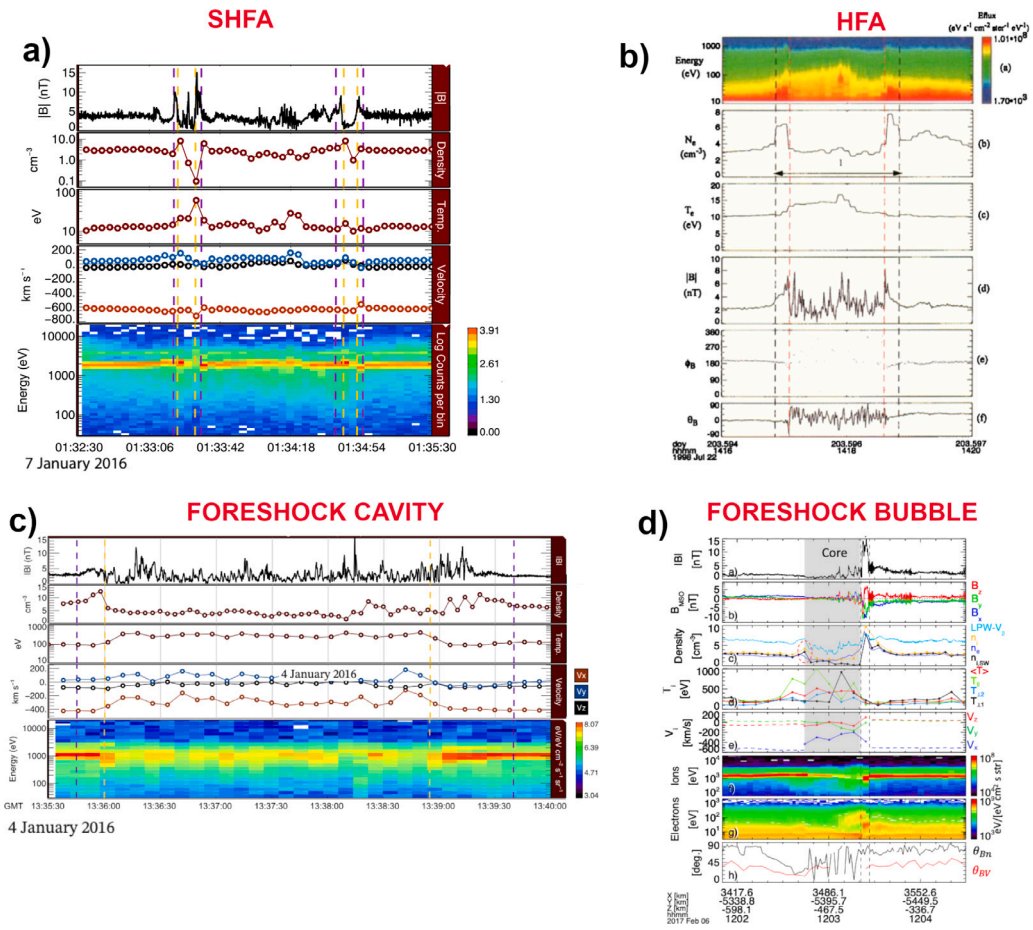

Fig. 19. Observations of upstream transient structures at Mars. (a) Spontaneous hot flow anomalies (adapted from Collinson et al., 2017), (b) hot flow anomaly (from Øieroset et al., 2001), (c) foreshock cavity (adapted from Collinson et al., 2020) and (d) foreshock bubble (from Madanian et al., 2023).

4.3.4. Foreshock bubbles

Foreshock bubbles are the most recently discovered transient structure upstream of the Martian bow shock. Madanian et al. (2023, see Fig. 19d) reported observations of three foreshock bubbles. These events show similar plasma and magnetic field signatures as their counterparts at Earth, however, an analysis of ion distributions associated with them, exhibits some important differences. Apart from the incident solar wind ions and the backstreaming ions reflected at the quasi-parallel bow shock, the authors also observed the presence of suprathermal ions reflected at the quasi-perpendicular bow shock which also interact with the associated IMF directional discontinuity. This occurs due to the small size of the Martian bow shock and a large ion gyroradius of reflected ions. Thus, the foreshock bubbles at Mars form due to the interaction of IMF directional discontinuities with ions reflected at quasi-parallel and also at quasi-perpendicular bow shock.

4.4. Martian magnetosheath

The Martian magnetosheath is found between the Mars bow shock and its Magnetic Pile-up Boundary (MPB). It is characterized as a turbulent region with thermalized solar wind plasma (Mazelle et al., 2004). The Mars magnetosheath is mainly filled by protons and alpha particles, although due to Mars extended exosphere, planetary ions are not restricted to the induced magnetosphere, where they dominate (Dubinin et al., 1997; Sauer et al., 1998; Nagy et al., 2004). The presence of planetary ions in the Martian magnetosheath, such as O^+ and O_2^+, turns the solar wind–Mars interaction much more complex (Mazelle et al., 2004).

Unlike the Earth, Mars lacks an intrinsic magnetic field and has only remnant crustal fields. Nevertheless, the interaction of the solar wind with this body is rather similar to what happens in the terrestrial case (Bertucci et al., 2011). For Mars, its interaction with the solar wind starts far from the planet due to the presence of an extended hydrogen exosphere and an oxygen corona. Such interaction results in the formation of the bow shock, foreshock, magnetosheath, and finally the magnetosphere. In contrast to such an extended exosphere and corona, Mars has a small magnetosheath with a thickness of the order of a solar wind proton gyroradius.

Mars magnetosheath has been widely studied: Mariner 4, 6, and 7, Mars 2, 3, and 5, Phobos-2, Mars Global Surveyor (MGS), Mars Express (MEx), and more recently MAVEN have been dedicated to exploring this region. Starting with the early reports on the sheath existence with Mars-2 data (Vaisberg, 1992), its exploration has never stopped. A full description of the magnetosheath is an ambitious task, so here we present some of the most important features of that region.

4.4.1. Waves

As with any other planetary magnetosheath, Mars' sheath is characterized by intense plasma wave and turbulence activity. The sources of such activity can be local instabilities triggered by the high temperature anisotropy of the sheath, and upstream waves from the Martian foreshock. As for Mars, the extended exosphere reaches the sheath space, the presence of planetary ions will modify the magnetosheath dynamics and increase the wave activity too.

Therefore, a central topic to study about the Martian sheath is wave activity. Phobos-2 discovered it is a region permeated by bi-ion magnetoacoustic waves (Dubinin et al., 1997), which may steepen

resulting in shocklets (Dubinin and Sauer, 1999). These were also observed in Mars Global Surveyor data (Acuña et al., 1998) in addition to low-frequency magnetic oscillations near the proton gyrofrequency. Such compressive magnetic field waves were anti-correlated with the electron fluxes, suggesting the presence of mirror mode waves (Bertucci et al., 2004; Espley et al., 2004).

Despite Mars Express lack of magnetic field measurements, its plasma instruments allowed it to monitor the magnetosheath plasma. Using Mars Express ELS/ASPERA-3 electron observations, Winningham et al. (2006) found that, in the Mars magnetosheath, oscillations in the electron flux showed frequency peaks between 0.01 and 0.02 Hz. Franco et al. (2020), using a much longer (2005–2016) MEX database of electron density and temperature also from the ELS/ASPERA-3 instruments, identified the major frequencies of plasma waves in the Martian magnetosheath. That analysis was conducted by employing wavelet analysis, which is a useful tool to analyze non-stationary signals since it allows mapping changes in the time-scale plane of characteristic structures of a time series by decomposing the time series into time–frequency space (Torrence and Compo, 1998). Franco et al. (2020), found that ULF waves in the Mars magnetosheath showed higher spectral power and integrated spectral energy in the frequency range between 5 and 20 mHz. Those frequencies are near the local oxygen gyrofrequency in the Mars magnetosheath identified by Espley et al. (2004) using magnetic field data from the MGS spacecraft.

In recent years the MAVEN mission has improved our knowledge regarding waves and their role in magnetosheath dynamics. Ruhunusiri et al. (2015) reported that Alfvén modes are predominant in the sheath, followed in occurrence by the mirror modes and slow mode waves. Fowler et al. (2017) found the wave power to be spread in several frequency bands with the maximum power at the ULF range (0.01-0.05 Hz), indicating partial ion thermalization and therefore contributing to the dissipation of the kinetic energy from the upstream solar wind. Even though it was also shown by Ruhunusiri et al. (2017) that the Martian magnetosheath is dominated by locally generated turbulence ruled by a spectral index between −0.4 and −1.0, the plasma heating in the sheath is not enough to fully thermalize the shocked solar wind plasma. This is in part due to the small thickness of the magnetosheath (Fowler et al., 2017).

With MAVEN keeping track of the Martian sheath, Harada et al. (2019) confirmed the presence of electromagnetic ion cyclotron waves in the magnetosheath plasma with a proton temperature anisotropy and a moderate plasma beta. More importantly, the authors showed that such waves are prone to occur for solar wind with low Mach number. On the other hand, Simon Wedlund et al. (2022) reported unmistakable identification of mirror mode structures using both plasma and magnetic field data. The mirror waves were detected mostly in marginally stable plasma with $\beta_{\parallel} \sim 1$, and they appear as a mix of dips and peaks, therefore indicating different stages of the instability. Jin et al. (2022) showed the dominance of peak-like structures in the observations, followed by coherent structures and a minor number of dip-like waves. The authors also showed that because of larger growth rates than at Earth, the mirror unstable plasma at Mars' sheath saturates more rapidly. That results in a large number of peak-like structures behind the shock. Later on, Simon Wedlund et al. (2023) showed that mirror waves were abundant not only behind the planetary shock, mainly at large solar zenith angles, but also close to the induced magnetospheric boundary. Taking data from 6 years of the MAVEN mission, the authors found that the detection probability of mirror mode-like structures is higher for low extreme ultraviolet (EUV) solar flux levels, while for high solar EUV conditions the probability of detection increases in the tail region.

Magnetic holes (MH), defined as large depressions in the magnetic field magnitude, appear in the solar wind for high plasma beta conditions. Though their origin is not fully understood, there is strong evidence that they are related to mirror instability (Winterhalter et al., 1995). Such structures are also present in the Martian environment. Wu et al. (2021) found small-scale MH in the magnetosheath of Mars with durations below 1 s and sizes below a proton gyroradius. With an occurrence rate of 1.5 events per hour, MH are not only common but ubiquitous in the Martian sheath.

4.4.2. Effect of magnetosheath waves in martian ionosphere

It has been found that plasma waves can penetrate through planetary magnetospheres and ionospheres and interact with their atmospheres, with important consequences for their atmospheres evolution and possible habitability conditions (Potapov and Polyushkina, 2010; Collinson et al., 2018). Thus, it is an important issue to determine how far a plasma wave could propagate in the magnetospheric space environment. One useful parameter to compute this is the correlation length (CL), which corresponds to the distance from a point beyond which there is no further correlation of a physical property associated with that point (Mela and Louie, 2001). The CL is computed by applying an exponential fit in the parameter auto-correlation curve followed by a linear regression, which provides the CL in a temporal scale. In order to obtain the correlation length in a spatial scale, the temporal correlation length must be multiplied by the solar wind or local plasma velocity (de Souza Franco et al., 2019). Therefore, the CL allows the study of temporal and spatial scales at which oscillations in plasmas are correlated around Mars. de Souza Franco et al. (2019) computed the CL around Mars using more than 10 years of ELS/ASPERA-3/MEX data (2004–2015). It was found that at the dayside of the Martian magnetosheath, the correlation length (6.0×10^3 km) is approximately five times larger than the magnetosheath size (1.29×10^3 km). This can be considered an indication that wave fluctuations at the magnetosheath are correlated with oscillations in the planetary ionosphere, due to ULF waves that can penetrate into the ionopause. Further, it indicates that wave trains from the dayside magnetosheath/Magnetic pile-up region may cause resonance effects at the planetary ionopause and that the ionospheric plasma could react to these oscillations. This effect could consequently contribute to the enhanced ion escape from the Mars atmosphere.

Franco et al. (2023) performed a statistical study on 70 selected potential cases of wave propagation through the Martian ionopause using MEX data. For those cases, these authors found that the most energetic frequencies (periods with higher wavelet integrated spectral power) in the ionosphere were in the same range of the main frequencies found in the magnetosheath. Further, most part of the events presented moderate correlation ($0.4 < r < 0.7$) between magnetosheath (ASPERA-3) and ionosphere (MARSIS) electron density. The solar cycle seems to influence the wave penetration events, which tend to occur mainly in the descending/maximum solar cycle phases, probably due to the higher occurrence of large scale structures in the solar wind, such as CIRs and ICMEs. Other factors that act in the propagation events are the Mars local time, since the events are more frequent on the dayside, and the solar wind pressure, with most occurrence for moderate condition (≥0.5 and <1.0) nPa.

As mentioned before, turbulence in the plasma environment of Mars was studied by Ruhunusiri et al. (2017). Their results suggest that although transients in the Martian upstream region can propagate through the magnetosheath, it is locally generated fluctuations that dominate in the magnetosheath. Besides the spectral index, another important parameter to study plasma turbulence is the kurtosis, which is defined as a standardized fourth central moment of a data distribution (Bolzan and Echer, 2014), and gives a measure of the deviation from the Gaussianity of that distribution. When the distribution shows a heavy tail to extreme values, it means that intermittent processes are important in that system. The kurtosis is equal to 3 for normal distributions, while for time series that include intermittent values, it can be much higher than 3. Franco et al. (2022) conducted a statistical study of wave activity in the Martian magnetosheath using 12 years (2005–2016) of MEX magnetosheath crossings. The kurtosis analysis results indicated intermittent behavior in the electron density

and electron temperature data in the Mars magnetosheath. Further, higher values of kurtosis were found in the scales near the upstream proton gyrofrequency, supporting the hypothesis that upstream events have a significant contribution to the energy transfer process to the inner magnetosphere. In agreement with the results from Franco et al. (2023), that showed that the wave propagation into the ionopause of Mars occurs especially for the descending and maximum solar cycle phases, intermittence computed by kurtosis parameter was also higher during these solar cycle phases. Therefore, it seems that intermittent phenomena can contribute to the energy exchange among scales within the Martian magnetospheric environment, favoring the occurrence of wave propagation events.

4.4.3. Particles

The Martian magnetosheath is populated with shock-heated solar wind plasma, i.e. thermalized ions and electrons. However, part of this last population was found to be removed from the Martian sheath as the flux of energetic electrons of 100 eV strongly decreases within the sheath near the transition with the magnetic pileup boundary (Crider et al., 2000). Based on MAVEN data, Schwartz et al. (2019) explained the erosion of electrons as a result of the entrance, trapping, and escape of solar wind electrons crossing the bow shock. The decrease of energetic electrons with increasing depth into the sheath is a natural consequence of the three processes in addition to an electrostatic field which in turn will provide extra acceleration inside the sheath (Horaites et al., 2021).

Another interesting feature of the Martian magnetosheath is the fact that here the solar wind plasma flows asymmetrically (Dubinin et al., 2018; Halekas et al., 2017). Such asymmetry can be explained in terms of a two-fluid description: the solar wind protons and the oxygen ions which experience solar wind mass loading derived from the hot oxygen corona (Romanelli et al., 2020).

4.4.4. Other structures

Energetic ions accelerated by the quasi-parallel shock can be injected into the magnetosheath along the magnetic field lines. As a result of such pressure enhancements, the decrease in plasma pressure increases the ion density. This produces anti-correlated spatial oscillations in plasma density and temperature which are known as magnetosheath filamentary structures (Omidi et al., 2014). Such structures have been reported to exist on Mars according to Dubinin and Fraenz (2016).

Solitary bipolar electric field structures have also been identified in Mars magnetosheath and are characterized by short duration (0.5 ms) bipolar electric pulses (1-25 mV/m) (Thaller et al., 2022; Kakad et al., 2022). Though electric fields will accelerate particles by a potential drop, such bipolar structures barely energize the sheath ions and therefore play a minor role in the proton dynamics in the magnetosheath.

More recently, Dubinin et al. (2023) reported the observations of mini-induced magnetospheres in the Mars sheath whose sizes range from hundreds to thousands of kilometers. Such magnetospheric cavities are linked to small sheath regions where the density of oxygen ions from the ion escaping plume is similar to the solar wind proton density, resembling the interaction between the solar wind plasma and an ion cloud in a similar way to how the SW interacts with Venus or Mars itself. The observed mini-magnetospheres have the similar characteristics of an induced planetary magnetosphere (Halekas et al., 2021; Brain, 2021): magnetic field draping, magnetic barrier, magnetospheric cavity, tail and even a current sheet.

5. Imaging planetary magnetosphere–ionosphere

5.1. Introduction

There are many reasons to study the solar wind's interaction with both magnetized and unmagnetized planetary obstacles. By doing so, we learn crucial information about fundamental plasma physics processes that operate throughout the universe, such as magnetic reconnection, charged particle acceleration, ion-neutral interactions, and turbulence. We understand the phenomena that make heliophysics a unique research discipline, one in which plasmas organize themselves into vast nearly uniform regions separated by narrow transitions or boundary layers, one in which field-aligned currents, streaming particles, and propagating waves teleconnect remote regions, and one in which microscale processes on electron and ion gyroradii scales can have global consequences. However, there are other, entirely practical, reasons to study the solar wind's interaction with planetary obstacles. Space weather, which includes hazardous phenomena such as radiation hazards, atmospheric drag, and communication disruptions, affects both humans and their technological systems. Safeguarding human endeavors on the ground, in the Earth's upper atmosphere, journeys through interplanetary space, and visits to other planets demands the ability to predict space weather accurately.

As described elsewhere in this paper, the past 60+ years of the space age have seen the frequent use of in situ and occasional use of remote observations to define the geography of the major plasma regimes surrounding Earth, including its ionosphere and plasmasphere, ring current, plasma sheet, magnetotail lobes, cusps, magnetosheath, and foreshock. The same observations have been used to identify the boundaries delimiting these regions, e.g., the plasmapause, the earthward edge and boundary layers of the plasma sheet, the magnetopause, and the bow shock. The left panel of Fig. 20 illustrates the locations of some of these structures. Correlative studies have associated solar wind with magnetospheric and ionospheric phenomena. Consequently, we now have a basic understanding of how solar wind variability drives the global interaction. However, a host of processes that govern the flow of energy into and through the global system have been proposed, and we do not yet know which of them (e.g. bursty or continuous, patchy or extended reconnection) predominate as a function of location and solar wind and magnetospheric conditions. We incorporate what knowledge we do learn into increasingly accurate first principal global simulations. Unlike Earth, Mars is a planet with no global intrinsic magnetic field. Yet in situ observations provide evidence for many of the same phenomena that occur at Earth: an ionosphere, plasma sheet, aurora, magnetotail, a kind of iono- or magneto-pause at the inner edge of a magnetosheath magnetic pile up region, a bow shock, and a foreshock. The right panel of Fig. 20 illustrates the locations of some of the structures seen at Mars. Once again, increasingly complex and comprehensive numerical simulations now incorporate what we know to predict conditions in the immediate vicinity of the planet. The interactions at both planets are highly dynamic. Simultaneous global measurements are essential to identify and establish the intricate relationships between phenomena happening in different portions of the magnetosphere, to track the flow of mass, energy, and momentum through the planetary systems, and to verify and validate the predictions of global models. Here we face a great challenge. Space is vast, and there are no immediate prospects for constellation class missions making global multipoint measurements of plasma and magnetic field phenomena throughout planetary systems in the same manner that ground observatories (and balloons launched from these same ground observatories) are used to construct continental- and global-scale terrestrial weather maps. On the other hand, one or several well-instrumented remote sensing observatories might readily obtain simultaneous global observations in a cost-effective manner (Branduardi-Raymont et al., 2022), much in the same way that geosynchronous spacecraft currently track terrestrial weather patterns over continental scales, thereby obtaining quantitative information concerning cloud cover, moisture content, and atmospheric temperatures. We begin by exploring some of the rapidly developing instrument technologies now available for global imaging at Earth and Mars. Next we consider key research tasks at Earth and Mars. Finally we address prospects for future imaging missions

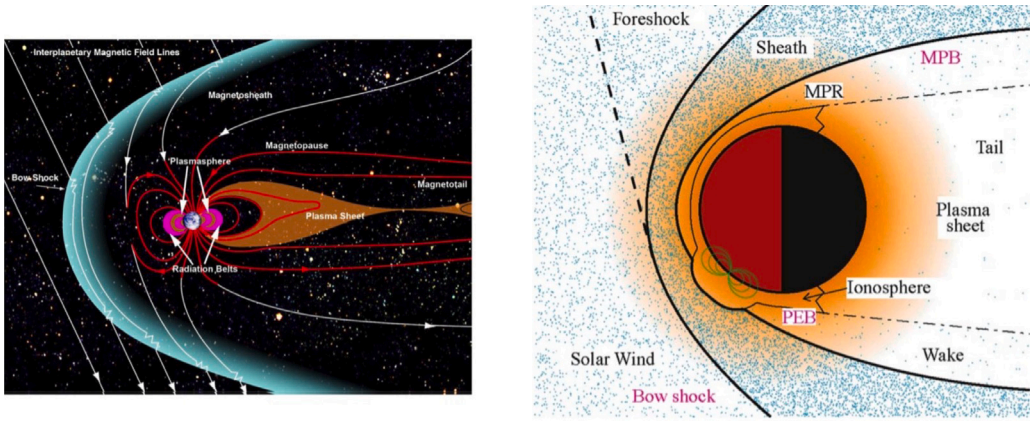

Fig. 20. Some of the plasma regimes at Earth (left) and Mars (right). The panel on the left is courtesy of NASA/GSFC. At Mars (Brain, 2006), the panel on the right illustrates a magnetic pile-up boundary (MPB), and a photoelectron boundary (PEB) separating the planetary ionosphere from the magnetic pileup region (MPR).
Source: Adapted from Brain (2006).

5.2. Imaging technologies

Here we consider 6 imaging technologies suitable for use as global imagers on planetary missions, pointing to papers that describing the instrument technology and past observations. Soft X-ray imagers observe the low energy (0.05 to 2 keV) line emission X-rays emitted isotropically when high charge state solar wind ions (e.g., C^{6+}, O^{7+}, O^{8+}, Fe^{12+}) encounter and exchange electrons with exospheric neutrals (Walsh et al., 2016; Sibeck et al., 2018). Emission intensities are proportional to the line-of-sight integral of the product of local neutral and plasma densities multiplied by an effective interaction velocity, whether bulk, thermal, or some combination therefore. At Earth and Mars, this happens primarily within the dayside magnetosheath, where the exosphere extends well beyond the magneto- or iono-pause to encounter high density shocked solar wind plasma. At Earth, it also happens within the cusps, where high density shocked solar wind plasma penetrates deep into the exosphere. Only weak emissions are expected in the solar wind region outside the bow shock, where both plasma and exospheric densities are low. Similarly, only weak or no emissions are expected within the Earth's magnetosphere, where the heavy ion population is primarily singly-charged and therefore unable to emit soft X-rays via charge exchange. A soft X-ray halo generated by charge exchange encircles remote Chandra and XMM images of Mars (Dennerl, 2002, 2006; Dennerl et al., 2006). Soft X-ray emissions provide information concerning the composition of high charge state solar wind ions, but not their energies. Energetic neutral atom (ENA) imagers observe the neutral atoms generated when singly charged ions (e.g., H^+ or O^+) exchange electrons with neutral atoms in the Earth's exosphere (Moore et al., 2000; Pollock et al., 2000; McComas et al., 2009; Mitchell et al., 2016) or Martian atmosphere (Barabash et al., 2006; Futaana et al., 2006; Galli et al., 2006). The newly generated neutral atoms proceed in the same directions as those of the original ions. Consequently, plasmas with much greater thermal than bulk velocities like those in the subsolar magnetosheath emit neutrals nearly isotropically, whereas plasmas with much greater bulk than thermal velocities emit beams of neutrals in the direction of bulk motion (Zhang et al., 2023). Potential targets include the magnetosheath and cusps (~1 keV neutrals), the plasma sheet (~5 keV neutrals), and the ring current (10-300 keV ions). Intensities depend upon the line of sight integral of ion velocities in the direction of the observing spacecraft multiplied by the product of exospheric neutral and ion phase space densities at the energetic to be detected. ENA observations provide crucial information concerning the composition and energy of singly-charged hydrogen and oxygen populations inside and outside the magnetosphere. Far Ultraviolet (FUV) and visible imagers observe the line or band-integrated auroral emissions generated when precipitating ions and electrons excite neutral atoms in the Earth's upper atmosphere. Satellite-borne FUV imagers can observe the global configuration of the Earth's auroral oval via observations of oxygen lines at 130.4 or 135.6 nm due to primarily to electron, but also to ion, precipitation, a Doppler-shifted hydrogen emission line at 121.8 nm due to proton precipitation, or entire bands from 140 to 160 (LBH) or 160 to 180 (LBHI) nm to observe Lyman–Birge–Hopfield emissions (Torr et al., 1995). By contrast, ground-based imagers typically provide detailed spatial resolution of emission lines including the red (oxygen atoms, 630.0 nm), green (oxygen atoms, 557.7 nm), and blue (nitrogen molecules, 427.8 nm) lines due to both ion and electron precipitation (Vallance Jones, 1974) and hydrogen emission lines at (121.8, 486.1, or 656.3 nm) due to proton precipitation (Eather, 1967). Ratios of line intensities provide information concerning the spectrum (i.e. energy or temperatures) of the precipitating electrons. Targets at earth include the ionospheric projections of the dayside cusp, magnetopause, low-latitude boundary layer, and plasma sheet. Discrete (Bertaux et al., 2005) and diffuse aurora have also been seen at Mars (Schneider et al., 2015). Where Martian magnetic fields are present, discrete auroral occurrence depends upon the orientation of the interplanetary magnetic field. Where they are absent, occurrence depends upon the solar wind dynamic pressure (Girazian et al., 2022). Extreme Ultraviolet (EUV) imagers observe resonantly scattered emissions from the He+ ions in the plasmasphere at 30.4 nm. They have been used successfully on the IMAGE (Sandel et al., 2003) and Chang'E-3 (He et al., 2013) missions to identify the location and motion of the plasmapause, from which crucial information can be obtained concerning electric fields within the inner magnetosphere (Goldstein et al., 2004). Observations at 83.4 nm can be used to image O^+ and O^{++} ions (Goldstein et al., 2022). Lyman-alpha imagers observe far ultraviolet emissions from the exosphere at 121.6 nm. The LAICA instrument on PROCYON took a single image demonstrating the feasibility of imaging the exosphere out to distances beyond 20 R_E from Earth (Kameda et al., 2017). Cucho-Padin et al. (2022) showed how these images could be used to reconstruct the three-dimensional structure of neutral densities in planetary exospheres. Accurate models of these exospheric neutral densities are needed for accurate predictions of the strength of the soft X-ray and ENA signals produced by charge exchange in planetary environments. Finally, Meier et al. (2009) have discussed the feasibility of using Thomson-scattered white sunlight to image terrestrial plasma electron density structures, including the plasmasphere and magnetosheath together with their boundaries. The instrument design would build upon a heritage of coronagraph and heliospheric imagers that track coronal mass ejections and corotating interaction regions in the solar wind. The same technique could be applied to image the Martian ionosphere and magnetosheath.

5.3. Objectives at Earth

The Earth presents an obstacle to the oncoming supersonic and superAlfvénic solar wind (Sibeck and Murphy, 2021). As a result, a bow shock forms upstream from Earth. It serves to slow, compress, and deflect the incoming solar wind plasma to flow through the magnetosheath surrounding the magnetosphere. Only a small fraction of the incoming solar wind mass, energy, and momentum succeeds in crossing the magnetopause, namely the outer boundary of the magnetosphere. Some of the magnetosheath plasma crosses the magnetopause and penetrates deep into the magnetosphere via the cusps, but particles in the cusps then either precipitate into the Earth's atmosphere or are reflected back upward to flow downstream in the antisunward direction. The overall interaction with the solar wind stretches the Earth's magnetic field antisunward into a magnetotail configuration with very tenuous north and south lobes separated by a denser plasma sheet. The same interaction creates an electric field that sculpts the magnetospheric extension of the Earth's ionosphere, namely the plasmasphere. The northern and southern auroral ovals separate regions of open magnetic field lines connected to the interplanetary magnetic field from closed magnetic field lines with both ends on Earth. The plasma sheet itself provides a source population of particles for energization and the ring current formation deep within the magnetosphere at distances of 3-5 earth radii (R_E) from Earth. Ring current particles may exit the magnetosphere via encounters with the magnetopause, precipitation into the atmosphere, or conversion into energetic neutral atoms, thereby completing the global flow of particles and energy cycle. While there is general agreement about the cycle described above, there is little consensus regarding the details involved at each step along the way (Sibeck et al., 2023). Magnetic reconnection controls the flow of mass, energy, and momentum across the magnetopause, its storage in the magnetotail lobes, and its release in the magnetotail plasma sheet. We do not know when reconnection is steady or impulsive, patchy or extensive at either the dayside magnetopause or deep within the magnetotail. We do not know the relative significance of steady and bursty particle injection into the ring current. And we do not know the relative significance of proposed ring current loss mechanisms. Yet each of the proposed interaction mechanisms leaves a tell-tale signature in magnetospheric particle populations, and these tell-tale signatures can be observed remotely by global imagers in space and on the ground. For example, bursty and steady reconnection produce step-like and gradual inward magnetopause erosion (soft X-rays) and equatorward dayside auroral motion (FUV imager), respectively. Transient brightenings in the dayside aurora move poleward into the polar cap. Steady and bursty nightside reconnection brighten and move the nightside auroral oval poleward (FUV and visible aurora) and inject ions deep into the magnetosphere (ENA) steadily and abruptly, respectively. Ring current ions leave the magnetosphere on the duskside and never appear on the dawnside (ENA and soft X-ray imagers), precipitate into the ionosphere to create proton aurora (ENA and FUV), or exchange charges with exospheric neutrals to create energetic neutral atoms (ENA). magnetopause motion and auroral brightening. Enhanced ring current strengths (ENA) generate northward magnetic fields in the magnetotail that may inhibit substorm onset (FUV and visible aurora) and may push out the dayside magnetopause (soft X-ray imager). The top panel of Fig. 21 shows a comparison of simulated soft X-ray and ENA images for the Earth at the red lines indicating three selected times in the top panel (Connor et al., 2021).

5.4. Objectives at Mars

At Mars, the key scientific question concerns atmospheric loss (Chicarro et al., 2004; Jakosky et al., 2015b). Proposed mechanisms include thermal escape, bombardment and hydrodynamic outflow, the removal of pick-up ions generated by photoionization or charge exchange, or the formation of detached blobs of ionospheric plasma generated by either the Kelvin–Helmholtz instability at the ionopause or magnetic reconnection with ionospheric or remnant crustal magnetic fields. Even in the absence of solar wind stripping, ambipolar electric fields may cause a planet to lose heavy ions. There is evidence for enhanced escape of ionospheric ions from unmagnetized planets during space weather storms (Luhmann et al., 2007; Edberg et al., 2011; Collinson et al., 2015; Jakosky et al., 2015a). Lyman-α imagers observe the integrated line-of-sight emissions from exospheric neutrals and can be used to quantify the escape rate of neutral hydrogen (Chaffin et al., 2018). ENA images of neutral ions provide a direct measure of the rate at which ionospheric ions are lost by charge exchange. Neutrals backscattered from the planetary atmosphere (Futaana et al., 2006) can be used to sound the upper atmospheres of unmagnetized planets (Kallio et al., 2006). Charge exchange in the Martian magnetosheath emits soft X-rays (Gunell et al., 2004). Remote sensing observations can also be used to address more basic questions regarding the solar wind's interaction with Mars. Continuous global images of the bow shock and ionopause in the soft X-rays and ENAs generated by charge exchange can map these boundaries and determine their response to varying solar wind Mach number, dynamic pressure, IMF orientation, season, crustal magnetic fields and solar extreme ultraviolet radiation (Brain, 2006). The observations can be used to distinguish between the predictions of different models (Gunell et al., 2006). They can help determine the cause(s) of discrete and diffuse aurora (Girazian et al., 2022), identify magnetic flux ropes (i.e., plasma blobs) generated at locations with crustal magnetic fields (Brain et al., 2010) and determine the significance of these ropes to plasma loss (Albee et al., 2001). The bottom panel of Fig. 21 shows predicted ENA emissions at Mars from spacecraft at a variety of solar zenith angles (Gunell et al., 2006).

5.5. Summary

A host of new imaging techniques are now available to provide cost effective global measurements of the tell-tale plasma density structures at Earth and Mars that diagnose proposed solar wind-planetary interaction and atmospheric loss mechanisms. A single spacecraft with a comprehensive payload can track the flow of solar wind energy through the Earth's magnetosphere or determine the rate of atmospheric loss at Mars. Such an imaging mission is a natural partner for missions that make in situ observations because the in situ missions provide global context whilst the in situ missions validate the inferences made from the images. A pair of such spacecraft could provide continuous observations of the auroral oval and conduct global tomography enabling the reconstruction of plasma and neutral density structures in the exosphere, magnetosheath, plasma sheet, and ring current.

6. Conclusion

High spatial and temporal resolution is required in future space missions (Larkin et al., 2024). A number of multi-point techniques have improved spatial and temporal resolution in multi-spacecraft data analysis. The curlometer technique (Dunlop et al., 2021) initially developed to analyze 4-spacecraft *Cluster* magnetic field data has been adapted to 4-spacecraft *MMS*, 3-5 spacecraft *THEMIS*, and 2-3 spacecraft *Swarm* constellations; and the extension of this technique to larger arrays of spacecraft has been considered. The curlometer technique has been successfully applied to study large-scale magnetospheric structures in the cross-tail current sheet, the ring current, the current layer at the magnetopause and field-aligned currents, as well as transient and small-scale current structures such as reconnected magnetic flux tubes or depolarization fronts and energy transfer processes. In addition, the curlometer technique has been applied to determine the current density in magnetic exhausts in solar wind turbulence (Chian et al., 2016). The wave telescope technique (Narita et al., 2022) is a multi-spacecraft wave analysis method based on the adaptive filter theory that provides

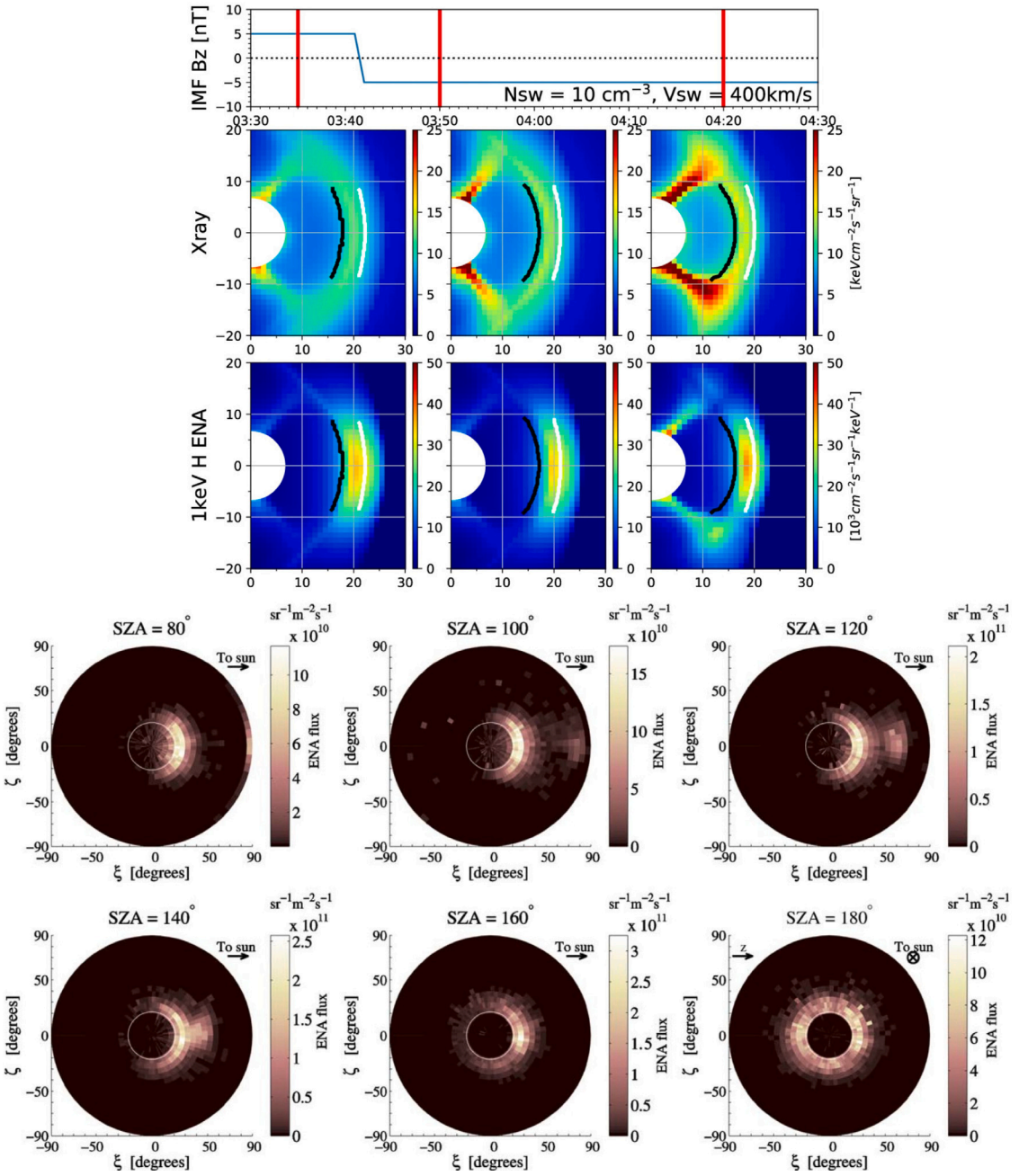

Fig. 21. Top: simulated images of the soft X-ray emission generated by charge exchange at Earth map out the bow shock, magnetopause, and cusps (Connor et al., 2021). Bottom: Simulated images of ENA emission from Mars map out the magnetosheath from different solar zenith angles (Gunell et al., 2006).
Source: Adapted from Connor et al. (2021) and Gunell et al. (2006).

an algorithm for computing the wavelengths and propagation directions without any prior assumption of wave modes or plasma model. This technique has been successfully applied to wave and turbulence studies of the *Cluster* fluxgate magnetometer data, leading to new insights of dispersion relations, phase velocity diagrams, propagation patterns, energy spectra, helicities, and higher-order statistics.

Terrestrial and Martian space weather is governed by a wealth of complex and nonlinear dynamical processes in the solar-planetary space environment, from the solar interior-photosphere-chromosphere-corona-wind to the planetary foreshock-magnetosheath–magnetopause–magnetosphere–ionosphere–atmosphere. In this paper, we have given a brief overview of some physical processes in complex Sun–Earth and Sun–Mars systems. Note that this brief overview is by no means a comprehensive review of the subject. Our goal is to boost space weather research and teaching activities, and to strengthen international collaboration involving universities and space research centers. In particular, we hope this paper will provide some guidelines for devising future space missions and to promote world harmony and peace through the joint development of space science and technology.

CRediT authorship contribution statement

Abraham Chian: Conceptualization, Writing – original draft, Writing – review & editing. **Rodrigo Miranda:** Writing – original draft, Writing – review & editing. **Cesar Bertucci:** Writing – original draft. **Xóchitl Blanco-Cano:** Writing – original draft. **Joe Borovsky:** Writing – original draft. **Sergio Dasso:** Writing – original draft. **Ezequiel Echer:** Writing – original draft. **Adriane Franco:** Writing – original draft.

Kirolosse M. Girgis: Writing – original draft. **J. Américo González-Esparza:** Writing – original draft. **Tohru Hada:** Writing – original draft. **Hiroshi Hasegawa:** Writing – original draft. **Syau-Yun Hsieh:** Writing – original draft. **Primoz Kajdič:** Writing – original draft. **Christian Mazelle:** Writing – original draft. **Erico Rempel:** Writing – original draft, Writing – review & editing. **Diana Rojas-Castillo:** Writing – original draft. **Beatriz Sánchez-Cano:** Writing – original draft. **David Sibeck:** Writing – original draft. **Marina Stepanova:** Writing – original draft. **José Valdés-Galicia:** Writing – original draft. **Juan Valdivia:** Writing – original draft.

Data availability

Data will be made available on request.

Acknowledgments

This paper is dedicated to the memory of Bertrand Lembege for his pioneer works on collisionless shocks in space plasmas, and for his passion for friendship and music. R.M. acknowledges the financial support from Brazilian agencies CNPq under grants 407341/2022-6, 407493/2022-0, COPEI/UnB under grant 7178, and FAP DF under grant 0193-00002206/2023-12. ELR acknowledges the financial support of Brazilian agency CNPq under grant 306920/2020-4. The work of D.R.-C. was supported by PAPIIT DGAPA Grant IA105223. B.S.-C. acknowledges support through UK-STFC Ernest Rutherford Fellowship ST/V004115/1. D.S. was funded by NASA's THEMIS program. S.-Y.H. was supported by NASA grant 80NSSC23K1241.

References

Acuña, M.H., Connerney, J.E.P., Wasilewski, P., Lin, R.P., Anderson, K.A., Carlson, C.W., McFadden, J., Curtis, D.W., Mitchell, D., Reme, H., Mazelle, C., Sauvaud, J.A., D'Uston, C., Cros, A., Medale, J.L., Bauer, S.J., Cloutier, P., Mayhew, M., Winterhalter, D., Ness, N.F., 1998. Magnetic field and plasma observations at Mars: Initial results of the Mars Global Surveyor mission. Science 279, 1676–1680. http://dx.doi.org/10.1126/science.279.5357.1676.

Ala-Lahti, M., Dimmock, A.P., Pulkkinen, T.I., Good, S.W., Yordanova, E., Turc, L., Kilpua, E.K.J., 2021. Transmission of an ICME sheath into the earth's magnetosheath and the occurrence of traveling foreshocks. J. Geophys. Res. (Space Phys.) 126 (12), e29896. http://dx.doi.org/10.1029/2021JA029896.

Albee, A.L., Arvidson, R.E., Palluconi, F., Thorpe, T., 2001. Overview of the Mars Global Surveyor mission. Journal of Geophysical Research: Planets 106 (E10), 23291–23316. http://dx.doi.org/10.1029/2000JE001306.

Alves, M.V., Echer, E., Gonzalez, W.D., 2006. Geoeffectiveness of corotating interaction regions as measured by Dst index. J. Geophys. Res. Space Phys. 111 (A7), 1–9.

Anderson, B.J., Fuselier, S.A., 1993. Magnetic pulsations from 0.1 to 4.0 Hz and associated plasma properties in the Earth's subsolar magnetosheath and plasma depletion layer. J. Geophys. Res. 98 (A2), 1461–1480. http://dx.doi.org/10.1029/92JA02197.

Angelopoulos, V., Mukai, T., Kokubun, S., 1999. Evidence for intermittency in Earth's plasma sheet and implications for self-organized criticality. Phys. Plasmas (ISSN: 1070-664X) 6 (11), 4161–4168. http://dx.doi.org/10.1063/1.873681.

Antiochos, S.K., Mikić, Z., Titov, V.S., Lionello, R., Linker, J.A., 2011. A model for the sources of the slow solar wind. Astrophys. J. 731 (2), 112. http://dx.doi.org/10.1088/0004-637X/731/2/112.

Antonova, E.E., 1985. The nonadiabatic character of diffusion and the equalization of concentration and temperature in the plasma sheet of the earth magnetosphere. Geomagn. Aeron. 25, 623–627.

Antonova, E.E., 2002. Magnetostatic equilibrium and turbulent transport in earth's magnetosphere: A review of experimental observation data and theoretical approach. Geomagn. Aeron. 3, 117–130.

Antonova, E.E., Ovchinnikov, I.L., 1999. Magnetostatically equilibrated plasma sheet with developed medium-scale turbulence: structure and implications for substorm dynamics. J. Geophys. Res. Space Phys. 104 (A8), 17289–17297. http://dx.doi.org/10.1029/1999JA900141.

Antonova, E.E., Stepanova, M.V., 2021. The impact of turbulence on physics of the geomagnetic tail. Front. Astron. Space Sci. 8, 622570. http://dx.doi.org/10.3389/fspas.2021.622570.

Antonova, E.E., Stepanova, M.V., Kirpichev, I.P., 2023. Main features of magnetospheric dynamics in the conditions of pressure balance. J. Atmos. Sol.-Terr. Phys. (ISSN: 1364-6826) 242, 105994. http://dx.doi.org/10.1016/j.jastp.2022.105994.

Archer, M.O., Hietala, H., Hartinger, M.D., Plaschke, F., Angelopoulos, V., 2019. Direct observations of a surface eigenmode of the dayside magnetopause. Nature Commun. 10 (1), 615. http://dx.doi.org/10.1038/s41467-018-08134-5.

Archer, M.O., Horbury, T.S., 2013. Magnetosheath dynamic pressure enhancements: occurrence and typical properties. Ann. Geophys. 31 (2), 319–331. http://dx.doi.org/10.5194/angeo-31-319-2013.

Archer, M.O., Horbury, T.S., Eastwood, J.P., 2012. Magnetosheath pressure pulses: Generation downstream of the bow shock from solar wind discontinuities. J. Geophys. Res. (Space Phys.) 117 (A5), A05228. http://dx.doi.org/10.1029/2011JA017468.

Archer, M.O., Turner, D.L., Eastwood, J.P., Schwartz, S.J., Horbury, T.S., 2015. Global impacts of a Foreshock Bubble: Magnetosheath, magnetopause and ground-based observations. Planet. Space Sci. 106, 56–66. http://dx.doi.org/10.1016/j.pss.2014.11.026.

Bale, S.D., Badman, S.T., Bonnell, J.W., Bowen, T.A., Burgess, D., Case, A.W., Cattell, C.A., Chandran, B.D.G., Chaston, C.C., Chen, C.H.K., et al., 2019. Highly structured slow solar wind emerging from an equatorial coronal hole. Nature 576 (7786), 237–242.

Bame, S.J., Asbridge, J.R., Feldman, W.C., Gosling, J.T., Paschmann, G., Skopke, N., 1980. Deceleration of the solar wind upstream from the earth's bow shock and the origin of diffuse upstream ions. J. Geophys. Res. 85 (A6), 2981–2990. http://dx.doi.org/10.1029/JA085iA06p02981.

Bandt, C., 2005. Ordinal time series analysis. Ecol. Model. 182 (3–4), 229–238.

Barabash, S., Lundin, R., Andersson, H., Brinkfeldt, K., Grigoriev, A., Gunell, H., Holmström, M., Yamauchi, M., Asamura, K., Bochsler, P., et al., 2006. The analyzer of space plasmas and energetic atoms (ASPERA-3) for the Mars express mission. Space Sci. Rev. 126, 113–164.

Bertaux, J.-L., Leblanc, F., Witasse, O., Quemerais, E., Lilensten, J., Stern, S.A., Sandel, B., Korablev, O., 2005. Discovery of an aurora on Mars. Nature 435 (7043), 790–794.

Bertucci, C., Duru, F., Edberg, N., Fraenz, M., Martinecz, C., Szego, K., Vaisberg, O., 2011. The induced magnetospheres of Mars, venus, and titan. Space Sci. Rev. 162 (1–4), 113–171. http://dx.doi.org/10.1007/s11214-011-9845-1.

Bertucci, C., Mazelle, C., Crider, D., Mitchell, D., Sauer, K., Acuña, M., Connerney, J., Lin, R., Ness, N., Winterhalter, D., 2004. MGS MAG/ER observations at the magnetic pileup boundary of Mars: draping enhancement and low frequency waves. Adv. Space Res. (ISSN: 0273-1177) 33 (11), 1938–1944. http://dx.doi.org/10.1016/j.asr.2003.04.054, Comparative Magnetospheres.

Bertucci, C., Mazelle, C., Crider, D.H., Vignes, D., Acuña, M.H., Mitchell, D.L., Lin, R.P., Connerney, J.E.P., Rème, H., Cloutier, P.A., Ness, N.F., Winterhalter, D., 2003. Magnetic field draping enhancement at the Martian magnetic pileup boundary from Mars global surveyor observations. Geophys. Res. Lett. 30 (2), 1099. http://dx.doi.org/10.1029/2002GL015713.

Billingham, L., Schwartz, S.J., Sibeck, D.G., 2008. The statistics of foreshock cavities: results of a Cluster survey. Ann. Geophys. 26, 3653–3667. http://dx.doi.org/10.5194/angeo-26-3653-2008.

Billingham, L., Schwartz, S.J., Wilber, M., 2011. Foreshock cavities and internal foreshock boundaries. Planet. Space Sci. 59, 456–467. http://dx.doi.org/10.1016/j.pss.2010.01.012.

Blanco-Cano, X., 2010. Bow shocks in the solar wind: Lessons towards understanding interplanetary shocks. AIP Conf. Proc. 1216 (1), 459–465. http://dx.doi.org/10.1063/1.3395903.

Blanco-Cano, X., Battarbee, M., Turc, L., Dimmock, A.P., Kilpua, E.K.J., Hoilijoki, S., Ganse, U., Sibeck, D.G., Cassak, P.A., Fear, R.C., Jarvinen, R., Juusola, L., Pfau-Kempf, Y., Vainio, R., Palmroth, M., 2018. Cavitons and spontaneous hot flow anomalies in a hybrid-Vlasov global magnetospheric simulation. Ann. Geophys. 36 (4), 1081–1097. http://dx.doi.org/10.5194/angeo-36-1081-2018.

Blanco-Cano, X., Omidi, N., Russell, C.T., 2009. Global hybrid simulations: Foreshock waves and cavitons under radial interplanetary magnetic field geometry. J. Geophys. Res. 114, A01216. http://dx.doi.org/10.1029/2008JA013406.

Blanco-Cano, X., Preisser, L., Kajdič, P., Rojas-Castillo, D., 2020. Magnetosheath microstructure: Mirror mode waves and jets during southward IP magnetic field. J. Geophys. Res. (Space Phys.) 125 (9), e27940. http://dx.doi.org/10.1029/2020JA027940.

Blanco-Cano, X., Rojas-Castillo, D., Kajdič, P., Preisser, L., 2023. Jets and mirror mode waves in earth's magnetosheath. J. Geophys. Res. Space Phys. http://dx.doi.org/10.1029/2022JA031221, e2022JA031221.

Blunier, S., Toledo, B., Rogan, J., Valdivia, J.A., 2021. A nonlinear system science approach to find the robust solar wind drivers of the multivariate magnetosphere. Space Weather (ISSN: 1542-7390, 1542-7390) 19 (6), http://dx.doi.org/10.1029/2020SW002634, e2020SW002634.

Bolzan, M., Echer, E., 2014. A multifractal approach applied to the magnetic field turbulence in Jupiter's magnetosheath. Planet. Space Sci. (ISSN: 0032-0633) 91, 77–82. http://dx.doi.org/10.1016/j.pss.2013.12.004.

Borodkova, N.L., Sibeck, D.G., Zastenker, G.N., Romanov, S.A., Sauvaud, J.A., 1998. Fast deformation of dayside magnetopause. Cosmic Res. 36 (3), 245.

Borovsky, J.E., 2008. Flux tube texture of the solar wind: Strands of the magnetic carpet at 1 AU? J. Geophys. Res. Space Phys. 113 (A8).

Borovsky, J.E., 2021. Magnetospheric plasma systems science and solar wind plasma systems science: The plasma-wave interactions of multiple particle populations. Front. Astron. Space Sci. 8, 200. http://dx.doi.org/10.3389/fspas.2021.780321.

Borovsky, J.E., Elphic, R.C., Funsten, H.O., Thomsen, M.F., 1997. The Earth's plasma sheet as a laboratory for flow turbulence in high-β MHD. J. Plasma Phys. 57 (1), 1–34. http://dx.doi.org/10.1017/S0022377896005259.

Borovsky, J.E., Funsten, H.O., 2003. MHD turbulence in the Earth's plasma sheet: Dynamics, dissipation, and driving. J. Geophys. Res. (Space Phys.) 108 (A5), 1284.

Borovsky, J.E., Valdivia, J.A., 2018. The Earth's magnetosphere: A systems science overview and assessment. Surv. Geophys. 39 (5), 817–859. http://dx.doi.org/10.1007/s10712-018-9487-x, ISSN: 0169-3298, 1573-0956.

Boscoboinik, G., Bertucci, C., Gomez, D., Morales, L., Mazelle, C., Halekas, J., Gruesbeck, J., Mitchell, D., Jakosky, B., Penou, E., 2020. The magnetic structure of the subsolar MPB current layer from MAVEN observations: Implications for the hall electric force. Geophys. Res. Lett. 47 (21), http://dx.doi.org/10.1029/2020GL089230, e2020GL089230.

Brain, D.A., 2006. Mars global surveyor measurements of the martian solar wind interaction. Space science reviews 126 (1-4), 77–112.

Brain, D.A., 2021. Induced magnetospheres. In: Magnetospheres in the Solar System. American Geophysical Union (AGU), ISBN: 9781119815624, pp. 441–451. http://dx.doi.org/10.1002/9781119815624.ch28.

Brain, D.A., Baker, A.H., Briggs, J., Eastwood, J.P., Halekas, J.S., Phan, T.-D., 2010. Episodic detachment of martian crustal magnetic fields leading to bulk atmospheric plasma escape. Geophysical Research Letters 37, L14108, http://dx.doi.org/10.1029/2010GL043916.

Branduardi-Raymont, G., Berthomier, M., Bogdanova, Y.V., Carter, J.A., Collier, M., Dimmock, A., Dunlop, M., Fear, R.C., Forsyth, C., Hubert, B., et al., 2022. Exploring solar-terrestrial interactions via multiple imaging observers. Exp. Astron. 54 (2–3), 361–390.

Brio, M., Wu, C.C., 1988. An upwind differencing scheme for the equations of ideal magnetohydrodynamics. J. Comput. Phys. 75, 400–422. http://dx.doi.org/10.1016/0021-9991(88)90120-9.

Bruno, R., 2019. Intermittency in solar wind turbulence from fluid to kinetic scales. Earth Space Sci. 6, 656.

Bruno, R., Carbone, V., 2013. The solar wind as a turbulence laboratory. Living Rev. Sol. Phys. 10, 2.

Bruno, R., Carbone, V., Veltri, P., Pietropaolo, E., Bavassano, B., 2001. Identifying intermittency events in the solar wind. Planet. Space Sci. 49 (12), 1201–1210.

Burgess, D., Schwartz, S.J., 1988. Colliding plasma structures: Current sheet and perpendicular shock. J. Geophys. Res. Space Phys. 93 (A10), 11327–11340. http://dx.doi.org/10.1029/JA093iA10p11327.

Burlaga, L.F., 2001. Lognormal and multifractal distributions of the heliospheric magnetic field. J. Geophys. Res.-Space Phys. 106, 15917.

Burlaga, L.F., F.-Viñas, A., 2004. Multi-scale probability distributions of solar wind speed fluctuations at 1 AU described by a generalized Tsallis distribution. Geophys. Res. Lett. 31 (16), L16807. http://dx.doi.org/10.1029/2004GL020715.

Burlaga, L., Sittler, E., Mariani, F., Schwenn, R., 1981. Magnetic loop behind an interplanetary shock: Voyager, Helios, and IMP 8 observations. J. Geophys. Res. Space Phys. 86 (A8), 6673–6684. http://dx.doi.org/10.1029/JA086iA08p06673.

Cai, D., Lembege, B., Hasegawa, H., Nishikawa, K.-I., 2018. Identifying 3D vortex structures at/around the magnetopause using a tetrahedral satellite configuration. J. Geophys. Res. Space Phys. 123, 10158–10176. http://dx.doi.org/10.1029/2018JA025547.

Chaffin, M.S., Chaufray, J.Y., Deighan, J., Schneider, N.M., Mayyasi, M., Clarke, J.T., Thiemann, E., Jain, S.K., Crismani, M.M.J., Stiepen, A., Eparvier, F.G., McClintock, W.E., Stewart, A.I.F., Holsclaw, G.M., Montmessin, F., Jakosky, B.M., 2018. Mars H escape rates derived from MAVEN/IUVS Lyman alpha brightness measurements and their dependence on model assumptions. Journal of Geophysical Research: Planets 123 (8), 2192–2210. http://dx.doi.org/10.1029/2018JE005574.

Chang, T.T.S., 2015. An introduction to space plasma complexity. Cambridge Atmospheric and Space Science Series. Cambridge University Press, http://dx.doi.org/10.1017/CBO9780511980251.

Chao, J.K., Lyu, L.H., Wu, B.H., Lazarus, A.J., Chang, T.S., Lepping, R.P., 1993. Observations of an intermediate shock in interplanetary space. J. Geophys. Res. 98 (A10), 17443–17450. http://dx.doi.org/10.1029/93JA01609.

Chaston, C.C., Wilber, M., Mozer, F.S., Fujimoto, M., Goldstein, M.L., Acuna, M., Reme, H., Fazakerley, A., 2007. Mode conversion and anomalous transport in Kelvin-Helmholtz vortices and kinetic Alfvén waves at the Earth's magnetopause. Phys. Rev. Lett. 99, 175004.

Chian, A.C.-L., Borotto, F.A., Hada, T., Miranda, R.A., Muñoz, P.R., Rempel, E.L., 2022. Nonlinear dynamics in space plasma turbulence: temporal stochastic chaos. Rev. Mod. Plasma Phys. 6 (1), 1–56. http://dx.doi.org/10.1007/s41614-022-00095-z.

Chian, A.C.-L., Feng, H.Q., Loew, M.H., Miranda, R.A., Muñoz, P.R., Sibeck, D.G., Wu, D.J., 2016. Genesis of interplanetary intermittent turbulence: a case study of rope-rope magnetic reconnection. Astrophys. J. 832, 179.

Chian, A.C.-L., Miranda, R.A., 2009. Cluster and ACE observations of phase synchronization in intermittent magnetic field turbulence: a comparative study of shocked and unshocked solar wind. Ann. Geophys. 27 (4), 1789–1801.

Chian, A.C.-L., Rempel, E.L., Aulanier, G., Schmieder, B., Shadden, S.C., Welsch, B.T., Yeates, A.R., 2014. Detection of coherent structures in photospheric turbulent flows. Astrophys. J. 786 (1), 51.

Chian, A.C.-L., Rempel, E.L., Silva, S.S.A., Bellot Rubio, L., Gošić, M., 2023. Intensification of magnetic field in merging magnetic flux tubes driven by supergranular vortical flows. Mon. Not. R. Astron. Soc. 518 (4), 4930–4942.

Chian, A.C.-L., Silva, S.S.A., Rempel, E.L., Gošić, M., Bellot-Rubio, L.R., Kusano, K., Miranda, R.A., Requerey, I.S., 2019. Supergranular turbulence in the quiet sun: Lagrangian coherent structures. Mon. Not. R. Astron. Soc. 488 (3), 3076–3088.

Chian, A.C.-L., Silva, S.S.A., Rempel, E.L., Rubio, L.R.B., Gošić, M., Kusano, K., Park, S.-H., 2020. Lagrangian chaotic saddles and objective vortices in solar plasmas. Phys. Rev. E 102 (6), 060201.

Chicarro, A., Martin, P., Trautner, R., 2004. The Mars Express mission: an overview. In: Wilson, A., Chicarro, A. (Eds.), Mars Express: the Scientific Payload, vol. 1240. ESA Special Publication, pp. 3–13.

Chu, C., Zhang, H., Sibeck, D., Otto, A., Zong, Q., Omidi, N., McFadden, J.P., Fruehauff, D., Angelopoulos, V., 2017. THEMIS satellite observations of hot flow anomalies at Earth's bow shock. Ann. Geophys. 35 (3), 443–451. http://dx.doi.org/10.5194/angeo-35-443-2017.

Cid, C., Saiz, E., Cerrato, Y., 2008. Comment on "interplanetary conditions leading to superintense geomagnetic storms Dst ≤ -250 nT during solar cycle 23" by Echer et al.. Geophys. Res. Lett. 35, L21107. http://dx.doi.org/10.1029/2008GL034731.

Cnossen, I., Matzka, J., 2016. Changes in solar quiet magnetic variations since the Maunder Minimum: A comparison of historical observations and model simulations. J. Geophys. Res. Space Phys. 121, 10.520–10.535. http://dx.doi.org/10.1002/2016JA023211.

Collinson, G., Halekas, J., Grebowsky, J., Connerney, J., Mitchell, D., Espley, J., DiBraccio, G., Mazelle, C., Sauvaud, J.-A., Fedorov, A., Jakosky, B., 2015. A hot flow anomaly at Mars. Geophys. Res. Lett. 42 (21), 9121–9127, https://doi-org.pbidi.unam.mx:2443/10.1002/2015GL065079.

Collinson, G., Sibeck, D., Omidi, N., Frahm, R., Zhang, T., Mitchell, D., Halekas, J., Espley, J., Futaana, Y., Jakosky, B., 2020. Foreshock cavities at Venus and Mars. J. Geophys. Res. Space Phys. 125 (8), http://dx.doi.org/10.1029/2020JA028023, e2020JA028023, 2020JA028023.

Collinson, G., Sibeck, D., Omidi, N., Grebowsky, J., Halekas, J., Mitchell, D., Espley, J., Zhang, T., Persson, M., Futaana, Y., Jakosky, B., 2017. Spontaneous hot flow anomalies at Mars and Venus. J. Geophys. Res. Space Phys. 122 (10), 9910–9923. http://dx.doi.org/10.1002/2017JA024196.

Collinson, G., Wilson III, L.B., Omidi, N., Sibeck, D., Espley, J., Fowler, C.M., Mitchell, D., Grebowsky, J., Mazelle, C., Ruhunusiri, S., Halekas, J., Frahm, R., Zhang, T., Futaana, Y., Jakosky, B., 2018. Solar wind induced waves in the skies of Mars: Ionospheric compression, energization, and escape resulting from the impact of ultralow frequency magnetosonic waves generated upstream of the martian bow shock. J. Geophys. Res. Space Phys. 123 (9), 7241–7256. http://dx.doi.org/10.1029/2018JA025414.

Connerney, J.E.P., Acuña, M.H., Wasilewski, P.J., Kletetschka, G., Ness, N.F., Rème, H., Lin, R.P., Mitchell, D.L., 2001. The global magnetic field of Mars and implications for crustal evolution. Geophys. Res. Lett. 28 (21), 4015–4018. http://dx.doi.org/10.1029/2001GL013619.

Connor, H.K., Sibeck, D.G., Collier, M.R., Baliukin, I.I., Branduardi-Raymont, G., Brandt, P.C., Buzulukova, N.Y., Collado-Vega, Y.M., Escoubet, C.P., Fok, M.-C., et al., 2021. Soft X-ray and ENA imaging of the earth's dayside magnetosphere. J. Geophys. Res. Space Phys. 126 (3), e2020JA028816.

Consolini, G., De Michelis, P., 1998. Non-Gaussian distribution function of AE-index fluctuations: Evidence for time intermittency. Geophys. Res. Lett. 25 (21), 4087–4090. http://dx.doi.org/10.1029/1998GL900073.

Cranmer, S.R., 2009. Coronal holes. Living Rev. Sol. Phys. 6, 3. http://dx.doi.org/10.12942/lrsp-2009-3.

Crider, D., Cloutier, P., Law, C., Walker, P., Chen, Y., Acuña, M., Connerney, J., Mitchell, D., Lin, R., Anderson, K., Carlson, C., McFadden, J., Rème, H., Mazelle, C., d'Uston, C., Sauvaud, J., Vignes, D., Brain, D., Ness, N., 2000. Evidence of electron impact ionization in the magnetic pileup boundary of Mars. Geophys. Res. Lett. 27 (1), 45–48. http://dx.doi.org/10.1029/1999GL003625.

Cucho-Padin, G., Kameda, S., Sibeck, D.G., 2022. The Earth's outer exospheric density distributions derived from PROCYON/LAICA UV observations. J. Geophys. Res. Space Phys. 127 (6), e2021JA030211.

Dachev, T.P., 2018. South-atlantic anomaly magnetic storms effects as observed outside the international space station in 2008–2016. J. Atmos. Sol.-Terr. Phys. 179, 251–260. http://dx.doi.org/10.1016/j.jastp.2018.08.009.

Daglis, I.A., Chang, L.C., Dasso, S., Gopalswamy, N., Khabarova, O.V., Kilpua, E., Lopez, R., Marsh, D., Matthes, K., Nandy, D., Seppälä, A., Shiokawa, K., Thiéblemont, R., Zong, Q., 2021. Predictability of variable solar-terrestrial coupling. Ann. Geophys. 39 (6), 1013–1035. http://dx.doi.org/10.5194/angeo-39-1013-2021.

Dal Lago, A., Gonzalez, W.D., Balmaceda, L.A., Vieira, L.E.A., Echer, E., Guarnieri, F.L., Santos, J., Silva, M., Lucas, A., Clua de Gonzalez, A., Schwenn, R., Schuch, N.J., 2006. The 1722 October (1999) solar-interplanetary-geomagnetic event: Very intense geomagnetic storm associated with a pressure balance between interplanetary coronal mass ejection and a high-speed stream. J. Geophys. Res. 111, A07S14. http://dx.doi.org/10.1029/2005JA011394.

Dasso, S., Mandrini, C.H., Démoulin, P., Luoni, M.L., 2006. A new model-independent method to compute magnetic helicity in magnetic clouds. Astron. Astrophys. 455, 349–359. http://dx.doi.org/10.1051/0004-6361:20064806.

Dasso, S., Mandrini, C.H., Démoulin, P., Luoni, M.L., Gulisano, A.M., 2005. Large scale MHD properties of interplanetary magnetic clouds. Adv. Space Res. 35, 711–724. http://dx.doi.org/10.1016/j.asr.2005.02.096.

Dasso, S., Mandrini, C.H., Schmieder, B., Cremades, H., Cid, C., Cerrato, Y., Saiz, E., De moulin, P., Zhukov, A.N., Rodriguez, L., Aran, A., Menvielle, M., Poedts, S., 2009. Linking two consecutive nonmerging magnetic clouds with their solar sources. J. Geophys. Res. 114, A02109. http://dx.doi.org/10.1029/2008JA013102.

de Carvalho Barreto, I.D., Stosic, T., Cezar Menezes, R.S., Alves da Silva, A.S., Rosso, O.A., Stosic, B., 2023. Hydrological changes caused by the construction of dams and reservoirs: The CECP analysis. Chaos 33 (2), 023115.

de Souza Franco, A.M., Fränz, M., Echer, E., Alves Bolzan, M.J., 2019. Correlation length around Mars: A statistical study with MEX and MAVEN observations. Earth Planet. Phys. 3 (6), 560–569. http://dx.doi.org/10.26464/epp2019051.

De Sterck, H., Low, B.C., Poedts, S., 1998. Complex magnetohydrodynamic bow shock topology in field-aligned low-beta flow around a perfectly conducting cylinder. Phys. Plasmas 5, 4015–4027. http://dx.doi.org/10.1063/1.873124.

De Sterck, H., Low, B.C., Poedts, S., 1999. Characteristic analysis of a complex two-dimensional magnetohydrodynamic bow shock flow with steady compound shocks. Phys. Plasmas 6, 954–969. http://dx.doi.org/10.1063/1.873336.

De Sterck, H., Poedts, S., 2001. Disintegration and reformation of intermediate-shock segments in three-dimensional MHD bow shock flows. J. Geophys. Res. 106 (A12), 30,023–30,037. http://dx.doi.org/10.1029/2000JA000205.

Deighan, J., Jain, S., Chaffin, M.S., Fang, X., Halekas, J.S., Clarke, J.T., Schneider, N.M., Stewart, A.I.F., Chaufray, J.-Y., Evans, J.S., et al., 2018. Discovery of a proton aurora at Mars. Nat. Astron. 2 (10), 802–807.

Démoulin, P., Janvier, M., Masías-Meza, J.J., Dasso, S., 2016. Quantitative model for the generic 3D shape of ICMEs at 1 AU. Astron. Astrophys. 595, A19. http://dx.doi.org/10.1051/0004-6361/201628164.

Dennerl, K., 2002. Discovery of X–rays from Mars with Chandra. Astron. Astrophys. 394 (3), 1119–1128.

Dennerl, K., 2006. X-Rays from Mars. Space Sci. Rev. 126 (1–4), 403.

Dennerl, K., Lisse, C.M., Bhardwaj, A., Burwitz, V., Englhauser, J., Gunell, H., Holmström, M., Jansen, F., Kharchenko, V., Rodríguez-Pascual, P.M., 2006. First observation of Mars with XMM-Newton-high resolution X-ray spectroscopy with RGS. Astron. Astrophys. 451 (2), 709–722.

Denton, M.H., Borovsky, J.E., Stepanova, M., Valdivia, J.A., 2016. Preface: Unsolved problems of magnetospheric physics: UNSOLVED PROBLEMS MAGNETOSPHERIC PHYSICS. J. Geophys. Res. Space Phys. (ISSN: 21699380) 121 (11), 10,783–10,785. http://dx.doi.org/10.1002/2016JA023362.

Denton, R.E., Li, X., Phan, T.-D., 1995. Bounded anisotropy fluid model for ion temperature evolution applied to AMPTE/IRM magnetosheath data. J. Geophys. Res. Space Phys. 100 (A8), 14925–14933. http://dx.doi.org/10.1029/95JA00656.

DiBraccio, G.A., Luhmann, J.G., Curry, S.M., Espley, J.R., Xu, S., Mitchell, D.L., Ma, Y., Dong, C., Gruesbeck, J.R., Connerney, J.E.P., Harada, Y., Ruhunusiri, S., Halekas, J.S., Soobiah, Y., Hara, T., Brain, D.A., Jakosky, B.M., 2018. The twisted configuration of the martian magnetotail: MAVEN observations. Geophys. Res. Lett. 45 (10), 4559–4568. http://dx.doi.org/10.1029/2018GL077251.

Dmitriev, A.V., Suvorova, A.V., 2015. Large-scale jets in the magnetosheath and plasma penetration across the magnetopause: THEMIS observations. J. Geophys. Res. (Space Phys.) 120 (6), 4423–4437. http://dx.doi.org/10.1002/2014JA020953.

Dmitriev, A.V., Suvorova, A.V., 2022. Atmospheric effects of magnetosheath jets. Atmosphere 14 (1), 45. http://dx.doi.org/10.3390/atmos14010045.

Dredger, P.M., Lopez, R.E., Hamrin, M., 2023. A case study in support of closure of bow shock current through the ionosphere utilizing multi–point observations and simulation. Front. Astron. Space Sci. 10, http://dx.doi.org/10.3389/fspas.2023.1098388, 1098388.

Dubinin, E., Fraenz, M., 2016. Ultra-low-frequency waves at venus and Mars: Keiling/low-frequency waves in space plasmas. In: Low-Frequency Waves in Space Plasmas. American Geophysical Union (AGU), ISBN: 9781119054955, pp. 343–364. http://dx.doi.org/10.1002/9781119055006.ch20.

Dubinin, E., Fraenz, M., Pätzold, M., Halekas, J.S., Mcfadden, J., Connerney, J.E.P., Jakosky, B.M., Vaisberg, O., Zelenyi, L., 2018. Solar wind deflection by mass loading in the martian magnetosheath based on MAVEN observations. Geophys. Res. Lett. 45 (6), 2574–2579. http://dx.doi.org/10.1002/2017GL076813.

Dubinin, E., Fraenz, M., Pätzold, M., Tellmann, S., DiBraccio, G., McFadden, J., 2023. The mini induced magnetospheres at Mars. Geophys. Res. Lett. 50 (3), http://dx.doi.org/10.1029/2022GL102324, e2022GL102324, 2022GL102324.

Dubinin, E., Modolo, R., Fraenz, M., Woch, J., Duru, F., Akalin, F., Gurnett, D., Lundin, R., Barabash, S., Plaut, J.J., Picardi, G., 2008. Structure and dynamics of the solar wind/ionosphere interface on Mars: MEX-ASPERA-3 and MEX-MARSIS observations. Geophys. Res. Lett. 35 (11), L11103. http://dx.doi.org/10.1029/2008GL033730.

Dubinin, E., Sauer, K., 1999. The martian magnetosphere - a laboratory for bi-ion plasma investigations. Astrophys. Space Sci. 264, 273–288. http://dx.doi.org/10.1023/A:1002459902486.

Dubinin, E., Sauer, K., Baumgärtel, K., Lundin, R., 1997. The martian magnetosheath: Phobos-2 observations. Adv. Space Res. (ISSN: 0273-1177) 20 (2), 149–153. http://dx.doi.org/10.1016/S0273-1177(97)00525-5, Planetary Ionospheres and Magnetospheres.

Dungey, J.W., 1961. Interplanetary magnetic field and the auroral zones. Phys. Rev. Lett. 6, 47–48. http://dx.doi.org/10.1103/PhysRevLett.6.47.

Dungey, J.W., 1962. The interplanetary magnetic field and the auroral zones. Scientific Report 157, The Pennsylvania State University, Ionospheric Research, pp. 1–29.

Dunlop, M.W., Dong, X.-C., Wang, T.-Y., Eastwood, J.P., Robert, P., Haaland, S., Yang, Y.-Y., Escoubet, P., Rong, Z.-J., Shen, C., Fu, H.-S., De Keyser, J., 2021. Curlometer technique and applications. J. Geophys. Res. Space Phys. 126 (11), http://dx.doi.org/10.1029/2021JA029538, e2021JA029538.

Eastwood, J.P., Lucek, E.A., Mazelle, C., Meziane, K., Narita, Y., Pickett, J., Treumann, R.A., 2005. The foreshock. Space Sci. Rev. 118 (1–4), 41–94. http://dx.doi.org/10.1007/s11214-005-3824-3.

Eastwood, J.P., Schwartz, S.J., Horbury, T.S., Carr, C.M., Glassmeier, K.-H., Richter, I., Koenders, C., Plaschke, F., Wild, J.A., 2011. Transient Pc3 wave activity generated by a hot flow anomaly: Cluster, Rosetta, and ground-based observations. J. Geophys. Res. Space Phys. 116 (A8), A08224. http://dx.doi.org/10.1029/2011JA016467.

Eather, R.H., 1967. Auroral proton precipitation and hydrogen emissions. Rev. Geophys. 5 (3), 207–285.

Echer, E., Bolzan, M.J.A., Franco, A.M.S., 2020. Statistical analysis of solar wind parameter variation with heliospheric distance: Ulysses observations in the ecliptic plane. Adv. Space Res. 65, 2846–2856.

Echer, E., Gonzalez, W.D., Tsurutani, B.T., 2008. Interplanetary conditions causing intense geomagnetic storms (Dst=- 100 nT) during solar cycle 23 (1996 – 2006). J. Geophys. Res. 113, A05221. http://dx.doi.org/10.1029/2007JA012744.

Echer, E., Tsurutani, B.T., Gonzalez, W.D., 2013. Interplanetary origins of moderate (-100 nT < Dst ≤ -50 nT) geomagnetic storms during solar cycle 23 (19962008). J. Geophys. Res. Space Phys. 118, 385–392. http://dx.doi.org/10.1029/2012JA018086.

Edberg, N.J.T., Nilsson, H., Futaana, Y., Stenberg, G., Lester, M., Cowley, S.W.H., Luhmann, J.G., McEnulty, T.R., Opgenoorth, H.J., Fedorov, A., et al., 2011. Atmospheric erosion of venus during stormy space weather. J. Geophys. Res. Space Phys. 116 (A9), A09308. http://dx.doi.org/10.1029/2011JA016749.

El-Alaoui, M., Ashour-Abdalla, M., Richard, R.L., Goldstein, M.L., Weygand, J.M., Walker, R.J., 2010. Global magnetohydrodynamic simulation of reconnection and turbulence in the plasma sheet. J. Geophys. Res. Space Phys. 115, A12236. http://dx.doi.org/10.1029/2010JA015653.

El-Alaoui, M., Richard, R.L., Ashour-Abdalla, M., Goldstein, M.L., Walker, R.J., 2013. Dipolarization and turbulence in the plasma sheet during a substorm: THEMIS observations and global MHD simulations. J. Geophys. Res. Space Phys. 118 (12), 7752–7761. http://dx.doi.org/10.1002/2013JA019322.

Engebretson, M.J., Zanetti, L.J., Potemra, T.A., Baumjohann, W., Luehr, H., Acuna, M.H., 1987. Simultaneous observation of Pc 3-4 pulsations in the solar wind and in the Earth's magnetosphere. J. Geophys. Res. 92 (A9), 10053–10062. http://dx.doi.org/10.1029/JA092iA09p10053.

Enžl, J., Přech, L., Šafránková, J., Němeček, Z., 2014. Statistical study of reconnection exhausts in the solar wind. Astrophys. J. 796 (1), 21.

Eriksson, S., Hasegawa, H., Teh, W.-L., et al., 2009. Magnetic island formation between large-scale flow vortices at an undulating postnoon magnetopause for northward interplanetary magnetic field. J. Geophys. Res. 114, A00C17. http://dx.doi.org/10.1029/2008JA013505.

Espley, J.R., Cloutier, P.A., Brain, D.A., Crider, D.H., AcuñA, M.H., 2004. Observations of low-frequency magnetic oscillations in the Martian magnetosheath, magnetic pileup region, and tail. J. Geophys. Res. (Space Phys.) 109 (A7), A07213. http://dx.doi.org/10.1029/2003JA010193.

Faganello, M., Califano, F., 2017. Magnetized kelvin-Helmholtz instability: theory and simulations in the earth's magnetosphere context. J. Plasma Phys. 83, 535830601. http://dx.doi.org/10.1017/S0022377817000770.

Falguere, D., Boscher, D., Nuns, T., Duzellier, S., Bourdarie, S., Ecoffet, R., Barde, S., Cueto, J., Alonzo, C., Hoffman, C., 2002. In-flight observations of the radiation environment and its effects on devices in the SAC-C polar orbit. IEEE Trans. Nucl. Sci. 49 (6), 2782–2787. http://dx.doi.org/10.1109/TNS.2002.805380.

Fang, X., Ma, Y., Brain, D., Dong, Y., Lillis, R., 2015. Control of Mars global atmospheric loss by the continuous rotation of the crustal magnetic field: A time-dependent MHD study. J. Geophys. Res. Space Phys. 120 (12), 10,926–10,944. http://dx.doi.org/10.1002/2015JA021605.

Feng, H.Q., Lin, C.C., Chao, J.K., Wu, D.J., Lyu, L.H., Lee, L.C., 2007. From Rankine-Hugoniot relation fitting procedure: tangential discontinuity or intermediate /slow shock? J. Geophys. Res. 112 (A10), A10104. http://dx.doi.org/10.1029/2007JA012311.

Feng, F., Wang, J.M., 2008. Observations of a 2-3 type interplanetary intermediate shock. Solar phys. 247, 195–201. http://dx.doi.org/10.1007/s11207-007-9087-2.

Fowler, C.M., Andersson, L., Halekas, J., Espley, J.R., Mazelle, C., Coughlin, E.R., Ergun, R.E., Andrews, D.J., Connerney, J.E.P., Jakosky, B., 2017. Electric and magnetic variations in the near-Mars environment. J. Geophys. Res. Space Phys. 122 (8), 8536–8559. http://dx.doi.org/10.1002/2016JA023411.

Franco, A.M.S., Echer, E., Bolzan, M.J.A., Fraenz, M., 2022. Study of fluctuations in the Martian magnetosheath using a kurtosis technique: Mars Express observations. Earth Planet. Phys. (ISSN: 2096-3955) 6 (RA275-Franco-F), 28. http://dx.doi.org/10.26464/epp2022006.

Franco, A.M.d., Echer, E., Fraenz, M., Bolzan, M.J.A., 2023. ULF waves propagating through the martian magnetosheath into the ionosphere: A statistical study using Mars Express observations. Braz. J. Phys. 53 (1), 14. http://dx.doi.org/10.1007/s13538-022-01213-5.

Franco, A., Fränz, M., Echer, E., Bolzan, M., 2020. Wavelet analysis of low frequency plasma oscillations in the magnetosheath of Mars. Adv. Space Res. (ISSN: 0273-1177) 65 (9), 2090–2098. http://dx.doi.org/10.1016/j.asr.2019.09.009, Magnetosphere, Ionosphere and their connection to Space Weather.

Fuselier, S.A., Klumpar, D.M., Shelley, E.G., Anderson, B.J., Coates, A.J., 1991. He^{2+} and H^{+} dynamics in the subsolar magnetosheath and plasma depletion layer. J. Geophys. Res. 96 (A12), 21095–21104. http://dx.doi.org/10.1029/91JA02145.

Futaana, Y., Barabash, S., Grigoriev, A., Holmström, M., Kallio, E., Gunell, H., Brinkfeldt, K., Lundin, R., Andersson, H., Yamauchi, M., et al., 2006. First ENA observations at Mars: ENA emissions from the Martian upper atmosphere. Icarus 182 (2), 424–430.

Futaana, Y., Barabash, S., Yamauchi, M., McKenna-Lawlor, S., Lundin, R., Luhmann, J., Brain, D., Carlsson, E., Sauvaud, J.-A., Winningham, J., Frahm, R., Wurz, P., Holmström, M., Gunell, H., Kallio, E., Baumjohann, W., Lammer, H., Sharber, J., Hsieh, K., Andersson, H., Grigoriev, A., Brinkfeldt, K., Nilsson, H., Asamura, K., Zhang, T., Coates, A., Linder, D., Kataria, D., Curtis, C., Sandel, B., Fedorov, A., Mazelle, C., Thocaven, J.-J., Grande, M., Koskinen, H.E., Sales, T., Schmidt, W., Riihela, P., Kozyra, J., Krupp, N., Woch, J., Fränz, M., Dubinin, E., Orsini, S., Cerulli-Irelli, R., Mura, A., Milillo, A., Maggi, M., Roelof, E., Brandt, P., Szego, K., Scherrer, J., Bochsler, P., 2008. Mars Express and Venus Express multi-point observations of geoeffective solar flare events in December 2006. Planet. Space Sci. (ISSN: 0032-0633) 56 (6), 873–880. http://dx.doi.org/10.1016/j.pss.2007.10.014, Mars Express/Venus Express.

Galli, A., Wurz, P., Barabash, S., Grigoriev, A., Gunell, H., Lundin, R., Holmström, M., Fedorov, A., 2006. Energetic hydrogen and oxygen atoms observed on the nightside of Mars. Space Science Reviews 126 (1-4), 267–297. http://dx.doi.org/10.1007/s11214-006-9088-8.

Gao, J.W., Rong, Z.J., Klinger, L., Li, X.Z., Liu, D., Wei, Y., 2021. A spherical harmonic martian crustal magnetic field model combining data sets of MAVEN and MGS. Earth Space Sci. 8 (10), http://dx.doi.org/10.1029/2021ea001860, e2021EA001860.

Garnier, P., Jacquey, C., Gendre, X., Génot, V., Mazelle, C., Fang, X., Gruesbeck, J.R., Sánchez-Cano, B., Halekas, J.S., 2022. The influence of crustal magnetic fields on the martian bow shock location: A statistical analysis of MAVEN and Mars Express observations. J. Geophys. Res. Space Phys. 127 (5), http://dx.doi.org/10.1029/2021JA030146, e2021JA030146, 2021JA030146.

Gary, S.P., 1993. Theory of Space Plasma Microinstabilities. Cambridge University Press.

Gary, S.P., Fuselier, S.A., Anderson, B.J., 1993. Ion anisotropy instabilities in the magnetosheath. J. Geophys. Res. 98 (A2), 1481–1488. http://dx.doi.org/10.1029/92JA01844.

Geyer, P., Temmer, M., Guo, J., Heinemann, S.G., 2021. Properties of stream interaction regions at Earth and Mars during the declining phase of solar cycle 24. Astron. Astrophys. 649, 1–20.

Girazian, Z., Schneider, N.M., Milby, Z., Fang, X., Halekas, J., Weber, T., Jain, S., Gérard, J.-C., Soret, L., Deighan, J., et al., 2022. Discrete aurora at Mars: Dependence on upstream solar wind conditions. J. Geophys. Res. Space Phys. 127 (4), e2021JA030238.

Girgis, K.M., Hada, T., 2018. Long-term variations of the solar wind effects on south atlantic anomaly (SAA) using tsyganenko model. In: International Exchange and Innovation Conference on Engineering & Sciences. IEICES, Vol. 4, Kyushu University, Fukuoka, pp. 36–41. http://dx.doi.org/10.15017/1960662.

Girgis, K.M., Hada, T., Matsukiyo, S., 2020a. Solar wind parameter and seasonal variation effects on the south atlantic anomaly using tsyganenko models. Earth Planets Space 72 (100), 1–17. http://dx.doi.org/10.1186/s40623-020-01221-2.

Girgis, K.M., Hada, T., Matsukiyo, S., 2020b. Space weather effects on proton flux variations in the South Atlantic Anomaly: A numerical study performed by test particle simulations. In: European Geosciences Union (EGU) General Assembly 2020. 10.5194/egusphere-egu2020-1551, http://dx.doi.org/10.5194/egusphere-egu2020-1551.

Girgis, K.M., Hada, T., Matsukiyo, S., 2021a. Estimation of single event upset (SEU) rates inside the SAA during the geomagnetic storm event of 15 May 2005. In: 2021 IEEE International Conference on Wireless for Space and Extreme Environments (WiSEE). IEEE, Cleveland, OH, USA, pp. 27–30. http://dx.doi.org/10.1109/WiSEE50203.2021.9613828.

Girgis, K.M., Hada, T., Matsukiyo, S., 2022a. Seasonal variation and geomagnetic storm index effects on the proton flux response in the South Atlantic Anomaly by test particle simulations. J. Atmos. Sol.-Terr. Phys. (ISSN: 1364-6826) 228 (105808), 1–9. http://dx.doi.org/10.1016/j.jastp.2021.105808.

Girgis, K.M., Hada, T., Matsukiyo, S., Yoshikawa, A., 2021b. Inner radiation belt simulations of the proton flux response in the South Atlantic Anomaly during the Geomagnetic Storm of 15 May 2005. J. Space Weather Space Climate 11 (48), 1–10. http://dx.doi.org/10.1051/swsc/2021031.

Girgis, K.M., Hada, T., Matsukiyo, S., Yoshikawa, A., 2022b. Radiation analysis of LEO mission in the South Atlantic Anomaly during Geomagnetic Storm. IEEE J. Radio Frequency Identification 6, 292–298. http://dx.doi.org/10.1109/JRFID.2022.3163441.

Glassmeier, K.H., Motschmann, U., Dunlop, M., Balogh, A., Acuña, M.H., Carr, C., Musmann, G., Fornaçon, K.H., Schweda, K., Vogt, J., Georgescu, E., Buchert, S., 2001. Cluster as a wave telescope - first results from the fluxgate magnetometer. Ann. Geophys. 19 (10), 1439–1447. http://dx.doi.org/10.5194/angeo-19-1439-2001.

Goldstein, J., Gallagher, D.L., Sandel, B.R., Davis, M., Molyneux, P., Veach, T., Fletcher, G., Gullikson, E., Windt, D., Allred, D.D., et al., 2022. The future of plasmaspheric extreme ultraviolet (EUV) imaging. In: Understanding the Space Environment Through Global Measurements. Elsevier, pp. 231–286.

Goldstein, J., Wolf, R.A., Sandel, B.R., Reiff, P.H., 2004. Electric fields deduced from plasmapause motion in IMAGE EUV images. Geophys. Res. Lett. 31 (1), L01801. http://dx.doi.org/10.1029/2003GL018797.

Gomes, L.F., Gomes, T.F.P., Rempel, E.L., Gama, S., 2023. Origin of multifractality in solar wind turbulence: the role of current sheets. Mon. Not. R. Astron. Soc. 519, 3623.

Gomes, T.F.G., Rempel, E.L., Ramos, F.M., Silva, S.S.A., Muñoz, P.R., 2019. Extreme value theory in the solar wind: the role of current sheets. Mon. Not. R. Astron. Soc. 490, 1879.

Gonzalez, W.D., Echer, E., Gonzalez, A.L., Tsurutani, B.T., 2007. Interplanetary origin of intense geomagnetic storms (Dst < -100 nT) during solar cycle 23. Geophys. Res. Lett. 34, 1–4. http://dx.doi.org/10.1029/2006GL028879.

Gonzalez, W.D., Echer, E., Tsurutani, B.T., Gonzalez, A.L., Lago, A., 2011. Interplanetary origin of intense, superintense and extreme geomagnetic storms. Space Sci. Rev. 158, 69–89. http://dx.doi.org/10.1007/s11214-010-9715-2.

Gonzalez, W.D., Joselyn, J.A., Kamide, Y., Kroehl, H.W., Rostoker, G., Tsurutani, B.T., Vasyliunas, V.M., 1994. What is a geomagnetic storm? J. Geophys. Res. 99, 5771–5792. http://dx.doi.org/10.1029/93JA02867.

Gonzalez, W.D., Tsurutani, B.T., 1987. Criteria of interplanetary parameters causing intense magnetic storms (Dst=- 100 nT). Planet. Space Sci. 35, 1101.

Gonzalez, W.D., Tsurutani, B.T., Clua de Gonzalez, A..L., 1999. Interplanetary origin of geomagnetic storms. Space Sci. Rev. 88, 529–562. http://dx.doi.org/10.1023/A:1005160129098.

Gonzalez-Esparza, J.A., 2000. Solar-cycle variations of interaction regions: in-ecliptic observations from 1 to 5 AU. Geofísica Internacional 39 (1), 41–46. http://dx.doi.org/10.22201/igeof.00167169p.2000.39.1.294.

González-Esparza, J.A., Smith, E.J., 1996. Solar cycle dependence of the solar wind dynamics: Pioneer Voyager, and Ulysses from 1 to 5 AU. J. Geophys. Res. Space Phys. 101 (A11), 24359–24371. http://dx.doi.org/10.1029/96JA02458.

González-Esparza, J.A., Smith, E.J., 1997. Three-dimensional nature of interaction regions: Pioneer, Voyager, and Ulysses solar cycle variations from 1 to 5 AU. J. Geophys. Res. Space Phys. 102 (A5), 9781–9792. http://dx.doi.org/10.1029/97JA00516.

Gosling, J.T., McComas, D.J., Phillips, J.L., Bame, S.J., 1991. Geomagnetic activity associated with earth passage of interplanetary shock disturbances and coronal mass ejections. J. Geophys. Res. Space Phys. 96 (A5), 7831–7839, https://doi-org.pbidi.unam.mx:2443/10.1029/91JA00316.

Gosling, J.T., Phan, T.D., 2013. Magnetic reconnection in the solar wind at current sheets associated with extremely small field shear angles. Astrophys. J. Lett. 763 (2), L39.

Greco, A., Chuychai, P., Matthaeus, W.H., Servidio, S., Dmitruk, P., 2008. Intermittent MHD structures and classical discontinuities. Geophys. Res. Lett. 35 (19), L19111. http://dx.doi.org/10.1029/2008GL035454.

Greco, A., Matthaeus, W.H., Servidio, S., Chuychai, P., Dmitruk, P., 2009. Statistical analysis of discontinuities in solar wind ACE data and comparison with intermittent MHD turbulence. Astrophys. J. 691 (2), L111.

Greenstadt, E.W., Olson, J.V., 1977. A contribution to ULF activity in the Pc 3-4 range correlated with IMF radial orientation. J. Geophys. Res. 82 (32), 4991. http://dx.doi.org/10.1029/JA082i032p04991.

Gruesbeck, J.R., Espley, J.R., Connerney, J.E.P., DiBraccio, G.A., Soobiah, Y.I., Brain, D., Mazelle, C., Dann, J., Halekas, J., Mitchell, D.L., 2018. The three-dimensional bow shock of Mars as observed by MAVEN. J. Geophys. Res. (Space Phys.) 123 (6), 4542–4555. http://dx.doi.org/10.1029/2018JA025366.

Guarnieri, F.L., 2006. The nature of auroras during high-intensity long-duration continuous AE activity (HILDCAA) events: 1998 to 2001. In: Tsurutani, B., McPherron, R., Lu, G., Sobral, J., Gopalswamy, N. (Eds.), Recurrent Magnetic Storms: Corotating Solar Wind Streams. American Geophysical Union (AGU), ISBN: 9781118666456, pp. 235–243. http://dx.doi.org/10.1029/167GM19.

Gunell, H., Holmström, M., Barabash, S., Kallio, E., Janhunen, P., Nagy, A.F., Ma, Y., 2006. Planetary ENA imaging: Effects of different interaction models for Mars. Planet. Space Sci. 54 (2), 117–131.

Gunell, H., Holmström, M., Kallio, E., Janhunen, P., Dennerl, K., 2004. X rays from solar wind charge exchange at Mars: a comparison of simulations and observations. Geophysical Research Letters 31 (22), http://dx.doi.org/10.1029/2004GL020953.

Guo, J., Zeitlin, C., Wimmer-Schweingruber, R.F., Hassler, D.M., Ehresmann, B., Rafkin, S., Freiherr von Forstner, J.L., Khaksarighiri, S., Liu, W., Wang, Y., 2021. Radiation environment for future human exploration on the surface of Mars: the current understanding based on MSL/RAD dose measurements. Astron. Astrophys. Rev. 29 (8), 1–81. http://dx.doi.org/10.1007/s00159-021-00136-5.

Hada, T., 1994. Evolutionary conditions in the dissipative MHD system: stability of intermediate MHD shock waves. Geophys. Res. Lett. 21 (21), 2275–2278. http://dx.doi.org/10.1029/94GL02239.

Hajra, R., Echer, E., Tsurutani, B.T., Gonzalez, W.D., 2013. Solar cycle dependence of high-IntensityLong-duration continuous AE activity (HILDCAA) events, relativistic electron predictors? J. Geophys. Res. Space Phys. 118, 5626–5638.

Hajra, R., Echer, E., Tsurutani, B.T., Gonzalez, W.D., 2014. Relativistic eletron acceleration during high-intensity, long-duration, continuous AE activity (HILDCAA) events: Solar cycle phase dependences. Geophys. Res. Lett. 41, 1876–1881.

Hajra, R., Franco, A.M.S., Echer, E., Bolzan, M.J.A., 2021. Long term variation of the geomagnetic activity: A comparison between the strong and the weak solar activity cycles and implications for the space climate. J. Geophys. Res. Space Phys. 126, 1–14. http://dx.doi.org/10.1029/2020JA028695.

Halekas, J.S., Luhmann, J.G., Dubinin, E., Ma, Y., 2021. Induced magnetospheres. In: Magnetospheres in the Solar System. American Geophysical Union (AGU), ISBN: 9781119815624, pp. 391–406. http://dx.doi.org/10.1002/9781119815624.ch25.

Halekas, J.S., Ruhunusiri, S., Harada, Y., Collinson, G., Mitchell, D.L., Mazelle, C., McFadden, J.P., Connerney, J.E.P., Espley, J.R., Eparvier, F., Luhmann, J.G., Jakosky, B.M., 2017. Structure, dynamics, and seasonal variability of the Mars-solar wind interaction: MAVEN Solar Wind Ion Analyzer in-flight performance and science results. J. Geophys. Res. (Space Phys.) 122 (1), 547–578. http://dx.doi.org/10.1002/2016JA023167.

Hall, B.E.S., Lester, M., Sánchez-Cano, B., Nichols, J.D., Andrews, D.J., Edberg, N.J.T., Opgenoorth, H.J., Fränz, M., Holmström, M., Ramstad, R., Witasse, O., Cartacci, M., Cicchetti, A., Noschese, R., Orosei, R., 2016. Annual variations in the Martian bow shock location as observed by the Mars Express mission. J. Geophys. Res. Space Phys. 121 (11), 11,474–11,494. http://dx.doi.org/10.1002/2016JA023316.

Hall, B.E.S., Sánchez-Cano, B., Wild, J.A., Lester, M., Holmström, M., 2019. The martian bow shock over solar cycle 23–24 as observed by the Mars Express mission. J. Geophys. Res. Space Phys. 124 (6), 4761–4772. http://dx.doi.org/10.1029/2018JA026404.

Han, D.S., Hietala, H., Chen, X.C., Nishimura, Y., Lyons, L.R., Liu, J.J., Hu, H.Q., Yang, H.G., 2017. Observational properties of dayside throat aurora and implications on the possible generation mechanisms. J. Geophys. Res. (Space Phys.) 122 (2), 1853–1870. http://dx.doi.org/10.1002/2016JA023394.

Hara, T., Brain, D.A., Mitchell, D.L., et al., 2017. MAVEN observations of a giant ionospheric flux rope near Mars resulting from interaction between the crustal and interplanetary draped magnetic fields. J. Geophys. Res. Space Phys. 122, 828–842. http://dx.doi.org/10.1002/2016JA023347.

Harada, Y., Ruhunusiri, S., Halekas, J.S., Espley, J., DiBraccio, G.A., Mcfadden, J.P., Mitchell, D.L., Mazelle, C., Collinson, G., Brain, D.A., Hara, T., Nosé, M., Oimatsu, S., Yamamoto, K., Jakosky, B.M., 2019. Locally generated ULF waves in the martian magnetosphere: MAVEN observations. J. Geophys. Res. Space Phys. 124 (11), 8707–8726. http://dx.doi.org/10.1029/2019JA027312.

Hartinger, M.D., Turner, D.L., Plaschke, F., Angelopoulos, V., Singer, H., 2013. The role of transient ion foreshock phenomena in driving Pc5 ULF wave activity. J. Geophys. Res. (Space Phys.) 118, 299–312. http://dx.doi.org/10.1029/2012JA018349.

Hasegawa, A., 1969. Drift mirror instability of the magnetosphere. Phys. Fluids 12, 2642–2650. http://dx.doi.org/10.1063/1.1692407.

Hasegawa, H., 2012. Structure and dynamics of the magnetopause and its boundary layers. Monogr. Environ. Earth Planets 1 (2), 71–119. http://dx.doi.org/10.5047/meep.2012.00102.0071.

He, F., Zhang, X.-X., Chen, B., Fok, M.-C., Zou, Y.-L., 2013. Moon-based EUV imaging of the Earth's plasmasphere: Model simulations. J. Geophys. Res. Space Phys. 118 (11), 7085–7103.

Hesse, M., Cassak, P.A., 2020. Magnetic reconnection in the space sciences: Past, present, and future. J. Geophys. Res. Space Phys. 125 (2), http://dx.doi.org/10.1029/2018JA025935, e2018JA025935, 2018JA025935.

Hietala, H., Laitinen, T.V., Andréeová, K., Vainio, R., Vaivads, A., Palmroth, M., Pulkkinen, T.I., Koskinen, H.E.J., Lucek, E.A., Rème, H., 2009. Supermagnetosonic jets behind a collisionless quasiparallel shock. Phys. Rev. Lett. 103 (24), 245001. http://dx.doi.org/10.1103/PhysRevLett.103.245001.

Hietala, H., Phan, T.D., Angelopoulos, V., Oieroset, M., Archer, M.O., Karlsson, T., Plaschke, F., 2018. In situ observations of a magnetosheath high-speed jet triggering magnetopause reconnection. Geophys. Res. Lett. 45 (4), 1732–1740. http://dx.doi.org/10.1002/2017GL076525.

Horaites, K., Andersson, L., Schwartz, S.J., Xu, S., Mitchell, D.L., Mazelle, C., Halekas, J., Gruesbeck, J., 2021. Observations of energized electrons in the martian magnetosheath. J. Geophys. Res. Space Phys. 126 (4), http://dx.doi.org/10.1029/2020JA028984, e2020JA028984, 2020JA028984.

Houston, S.J., Jess, D.B., Keppens, R., Stangalini, M., Keys, P.H., Grant, S.D.T., Jafarzadeh, S., McFetridge, L.M., Murabito, M., Ermolli, I., Giorgi, F., 2020. Magnetohydrodynamic nonlinearities in sunspot atmospheres: chromospheric detections of intermediate shocks. Astrophys. J. 892 (49), 1–14. http://dx.doi.org/10.3847/1538-4357/ab7a90.

Hwang, K.-J., Dokgo, K., Choi, E., Burch, J.L., Sibeck, D.G., Giles, B.L., et al., 2020. Magnetic reconnection inside a flux rope induced by Kelvin-Helmholtz vortices. J. Geophys. Res. Space Phys. 125, http://dx.doi.org/10.1029/2019JA027665, e2019JA027665.

Hwang, K.-J., Kuznetsova, M.M., Sahraoui, F., Goldstein, M.L., Lee, E., Parks, G.K., 2011. Kelvin-Helmholtz waves under southward interplanetary magnetic field. J. Geophys. Res. 116, A08210. http://dx.doi.org/10.1029/2011JA016596.

Inoue, T., Inutsuka, S., 2007. Evolutionary conditions in dissipative MHD systems revisited. Progr. Theor. Phys. 118 (1), 47–58. http://dx.doi.org/10.1143/PTP.118.47.

Jacobs, J.A., Kato, Y., Matsushita, S., Troitskaya, V.A., 1964. Classification of geomagnetic micropulsations. J. Geophys. Res. 69 (1), 180–181. http://dx.doi.org/10.1029/JZ069i001p00180.

Jacobsen, K.S., Phan, T.D., Eastwood, J.P., Sibeck, D.G., Moen, J.I., Angelopoulos, V., McFadden, J.P., Engebretson, M.J., Provan, G., Larson, D., Fornaçon, K.-H., 2009. THEMIS observations of extreme magnetopause motion caused by a hot flow anomaly. J. Geophys. Res. 114, A08210. http://dx.doi.org/10.1029/2008JA013873.

Jakosky, B.M., Grebowsky, J.M., Luhmann, J.G., Connerney, J., Eparvier, F., Ergun, R., Halekas, J., Larson, D., Mahaffy, P., Mcfadden, J., et al., 2015a. MAVEN observations of the response of Mars to an interplanetary coronal mass ejection. Science 350 (6261), aad0210.

Jakosky, B.M., Lin, R.P., Grebowsky, J.M., Luhmann, J.G., Mitchell, D.F., Beutelschies, G., Priser, T., Acuna, M., Andersson, L., Baird, D., Baker, D., Bartlett, R., Benna, M., Bougher, S., Brain, D., Carson, D., Cauffman, S., Chamberlin, P., Chaufray, J.Y., Cheatom, O., Clarke, J., Connerney, J., Cravens, T., Curtis, D., Delory, G., Demcak, S., DeWolfe, A., Eparvier, F., Ergun, R., Eriksson, A., Espley, J., Fang, X., Folta, D., Fox, J., Gomez-Rosa, C., Habenicht, S., Halekas, J., Holsclaw, G., Houghton, M., Howard, R., Jarosz, M., Jedrich, N., Johnson, M., Kasprzak, W., Kelley, M., King, T., Lankton, M., Larson, D., Leblanc, F., Lefevre, F., Lillis, R., Mahaffy, P., Mazelle, C., McClintock, W., McFadden, J., Mitchell, D.L., Montmessin, F., Morrissey, J., Peterson, W., Possel, W., Sauvaud, J.A., Schneider, N., Sidney, W., Sparacino, S., Stewart, A.I.F., Tolson, R., Toublanc, D., Waters, C., Woods, T., Yelle, R., Zurek, R., 2015b. The Mars Atmosphere and Volatile Evolution (MAVEN) mission. Space Sci. Rev. 195 (1–4), 3–48. http://dx.doi.org/10.1007/s11214-015-0139-x.

Jeffrey, A., Taniuti, T., 1964. Non-Linear Wave Propagation. Academic Press, ISBN: 9780080957807.

Jin, T., Lei, L., Yiteng, Z., Lianghai, X., Fuhao, Q., 2022. Statistical analysis of the distribution and evolution of mirror structures in the martian magnetosheath. Astrophys. J. 929 (2), 165. http://dx.doi.org/10.3847/1538-4357/ac5f00.

Jolitz, R.D., Dong, C.F., Rahmati, A., Brain, D.A., Lee, C.O., Lillis, R.J., Curry, S.M., Jakosky, B.M., 2021. Test particle model predictions of SEP electron transport and precipitation at Mars. J. Geophys. Res. Space Phys. 126 (8), http://dx.doi.org/10.1029/2021ja029132, e2021JA029132.

Kajdič, P., Blanco-Cano, X., Omidi, N., Rojas-Castillo, D., Sibeck, D.G., Billingham, L., 2017. Traveling foreshocks and transient foreshock phenomena. J. Geophys. Res. Space Phys. (ISSN: 2169-9402) 122 (9), 9148–9168. http://dx.doi.org/10.1002/2017JA023901, 2017JA023901.

Kajdič, P., Raptis, S., Blanco-Cano, X., Karlsson, T., 2021. Causes of jets in the quasi-perpendicular magnetosheath. Geophys. Res. Lett. 48 (13), http://dx.doi.org/10.1029/2021GL093173, e2021GL093173, 2021GL093173.

Kajdič, P., Raptis, S., Blanco-Cano, X., Karlsson, T., 2021a. Causes of jets in the quasi-perpendicular magnetosheath. Geophys. Res. Lett. 48 (13), http://dx.doi.org/10.1029/2021GL093173, e2021GL093173, 2021GL093173.

Kajdič, P., Sánchez-Cano, B., Neves-Ribeiro, L., Witasse, O., Bernal, G.C., Rojas-Castillo, D., Nilsson, H., Fedorov, A., 2021b. Interaction of space weather phenomena with Mars plasma environment during solar minimum 23/24. J. Geophys. Res. Space Phys. 126 (2), http://dx.doi.org/10.1029/2020JA028442, e2020JA028442, 2020JA028442.

Kajdič, P., Blanco-Cano, X., Omidi, N., Meziane, K., Russell, C.T., Sauvaud, J.-A., Dandouras, I., Lavraud, B., 2013. Statistical study of foreshock cavitons. Ann. Geophys. 31, 2163–2178. http://dx.doi.org/10.5194/angeo-31-2163-2013.

Kajdič, P., Blanco-Cano, X., Omidi, N., Russell, C.T., 2011. Multi-spacecraft study of foreshock cavitons upstream of the quasi-parallel bow shock. Planet. Space Sci. 59, 705–714. http://dx.doi.org/10.1016/j.pss.2011.02.005.

Kakad, B., Kakad, A., Aravindakshan, H., Kourakis, I., 2022. Debye-scale solitary structures in the martian magnetosheath. Astrophys. J. 934 (2), 126. http://dx.doi.org/10.3847/1538-4357/ac7b8b.

Kallio, E., Barabash, S., Brinkfeldt, K., Gunell, H., Holmström, M., Futaana, Y., Schmidt, W., Säles, T., Koskinen, H., Riihelä, P., Lundin, R., Andersson, H., Yamauchi, M., Grigoriev, A., Winningham, J., Frahm, R., Sharber, J., Scherrer, J., Coates, A., Linder, D., Kataria, D., Kozyra, J., Luhmann, J., Roelof, E., Williams, D., Livi, S., Brandt, P.C., Curtis, C., Hsieh, K., Sandel, B., Grande, M., Carter, M., Sauvaud, J.-A., Fedorov, A., Thocaven, J.-J., McKenna-Lawler, S., Orsini, S., Cerulli-Irelli, R., Maggi, M., Wurz, P., Bochsler, P., Krupp, N., Woch, J., Fränz, M., Asamura, K., Dierker, C., 2006. Energetic Neutral Atoms (ENA) at Mars: properties of the hydrogen atoms produced upstream of the martian bow shock and implications for ENA sounding technique around non-magnetized planets. Icarus (ISSN: 0019-1035) 182 (2), 448–463. http://dx.doi.org/10.1016/j.icarus.2005.12.019.

Kameda, S., Ikezawa, S., Sato, M., Kuwabara, M., Osada, N., Murakami, G., Yoshioka, K., Yoshikawa, I., Taguchi, M., Funase, R., et al., 2017. Ecliptic north-south symmetry of hydrogen geocorona. Geophys. Res. Lett. 44 (23), 11–706.

Kantrowitz, A.R., Petschek, H.E., 1964. MHD characteristics and shock waves, in Plasma Physics in Theory and Application. McGraw-Hill.

Karlsson, T., Brenning, N., Nilsson, H., Trotignon, J.G., Vallières, X., Facsko, G., 2012. Localized density enhancements in the magnetosheath: Three-dimensional morphology and possible importance for impulsive penetration. J. Geophys. Res. (Space Phys.) 117 (A3), A03227. http://dx.doi.org/10.1029/2011JA017059.

Karlsson, T., Kullen, A., Liljeblad, E., Brenning, N., Nilsson, H., Gunell, H., Hamrin, M., 2015. On the origin of magnetosheath plasmoids and their relation to magnetosheath jets. J. Geophys. Res. (Space Phys.) 120 (9), 7390–7403. http://dx.doi.org/10.1002/2015JA021487.

Karlsson, T., Liljeblad, E., Kullen, A., Raines, J.M., Slavin, J.A., Sundberg, T., 2016. Isolated magnetic field structures in Mercury's magnetosheath as possible analogues for terrestrial magnetosheath plasmoids and jets. Planet. Space Sci. 129, 61–73. http://dx.doi.org/10.1016/j.pss.2016.06.002.

Kataoka, R., Fukunishi, H., Lanzerotti, L.J., Rosenberg, T.J., Weatherwax, A.T., Engebretson, M.J., Watermann, J., 2002. Traveling convection vortices induced by solar wind tangential discontinuities. J. Geophys. Res. Space Phys. 107 (A12), SMP 22–1–SMP 22–12. http://dx.doi.org/10.1029/2002JA009459.

Katırcıoğlu, F.T., Kaymaz, Z., Sibeck, D.G., Dandouras, I., 2009. Magnetosheath cavities: case studies using Cluster observations. Ann. Geophys. 27 (10), 3765–3780. http://dx.doi.org/10.5194/angeo-27-3765-2009.

Kavosi, S., Raeder, J., 2015. Ubiquity of Kelvin-Helmholtz waves at Earth's magnetopause. Nature Commun. 6, 7019. http://dx.doi.org/10.1038/ncomms8019.

Kavosi, S., Raeder, J., Johnson, J.R., Nykyri, K., Farrugia, C.J., 2023. Seasonal and diurnal variations of Kelvin-Helmholtz instability at the Earth's magnetopause. Nature Commun. 14, 2513. http://dx.doi.org/10.1038/s41467-023-37485-x.

Keika, K., Nakamura, R., Volwerk, M., et al., 2009. Observations of plasma vortices in the vicinity of flow-braking: a case study. Ann. Geophys. 27, 3009–3017. http://dx.doi.org/10.5194/angeo-27-3009-2009.

Keiling, A., Angelopoulos, V., Weygand, J.M., et al., 2009. THEMIS ground-space observations during the development of auroral spirals. Ann. Geophys. 27, 4317–4332.

Kennel, C.F., Blandford, R.D., Coppi, P., 1989. MHD intermediate shock discontinuities. Part 1. Rankine-Hugoniot conditions. J. Plasma Phys. 42 (2), 299–319. http://dx.doi.org/10.1017/S0022377800014379.

Kieokaew, R., Lavraud, B., Foullon, C., Toledo-Redondo, S., Fargette, N., Hwang, K.-J., et al., 2020. Magnetic reconnection inside a flux transfer event-like structure in magnetopause kelvin-Helmholtz waves. J. Geophys. Res. Space Phys. 125, http://dx.doi.org/10.1029/2019JA027527, e2019JA027527.

Klein, K.-L., Dalla, S., 2017. Acceleration and propagation of solar energetic particles. Space Sci. Rev. 212 (3–4), 1107–1136. http://dx.doi.org/10.1007/s11214-017-0382-4.

Klimas, A.J., Valdivia, J.A., Vassiliadis, D., Baker, D.N., Hesse, M., Takalo, J., 2000. Self-organized criticality in the substorm phenomenon and its relation to localized reconnection in the magnetospheric plasma sheet. J. Geophys. Res. Space Phys. (ISSN: 01480227) 105 (A8), 18765–18780. http://dx.doi.org/10.1029/1999JA000319.

Koga, D., Chian, A.C.-L., Miranda, R.A., Rempel, E.L., 2007. Intermittent nature of solar wind turbulence near the Earth's bow shock: Phase coherence and non-Gaussianity. Phys. Rev. E 75 (4), 046401.

Krämer, E., Hamrin, M., Gunell, H., Karlsson, T., Steinvall, K., Goncharov, O., André, M., 2023. Waves in magnetosheath jets – classification and the search for generation mechanisms using MMS burst mode data. J. Geophys. Res. Space Phys. 128 (7), http://dx.doi.org/10.1029/2023JA031621, e2023JA031621, 2023JA031621.

Krieger, A.S., Timothy, A.F., Roelof, E.C., 1973. A coronal hole and its identification as the source of a high velocity solar wind stream. Sol. Phys. 29 (2), 505–525. http://dx.doi.org/10.1007/BF00150828.

La Belle-Hamer, A.L., Otto, A., Lee, L.C., 1994. Magnetic reconnection in the presence of sheared plasma flow: intermediate shock formation. Phys. Plasmas 1, 706–713. http://dx.doi.org/10.1063/1.870816.

Lacombe, C., Pantellini, F., Hubert, D., Harvey, C.C., Mangeney, A., Belmont, G., Russell, C.T., 1992. Mirror and Alfvénic waves observed by ISEE 1-2 during crossings of the Earth's bow shock. Ann. Geophys. 10, 772–784.

Lanabere, V., Dasso, S., Démoulin, P., Janvier, M., Rodriguez, L., Masías-Meza, J.J., 2020. Magnetic twist profile inside magnetic clouds derived with a superposed epoch analysis. Astron. Astrophys. 635, A85. http://dx.doi.org/10.1051/0004-6361/201937404.

Lanabere, V., Démoulin, P., Dasso, S., 2022. A robust estimation of the twist distribution in magnetic clouds. Astron. Astrophys. 668, A160. http://dx.doi.org/10.1051/0004-6361/202245062.

Langlais, B., Thébault, E., Houliez, A., Purucker, M.E., Lillis, R.J., 2019. A new model of the crustal magnetic field of Mars using MGS and MAVEN. J. Geophys. Res.: Planets 124 (6), 1542–1569. http://dx.doi.org/10.1029/2018je005854.

Larkin, C.J., Lundén, V., Schulz, L., Baumgartner-Steinleitner, M., Brekkum, M., Cegla, A., Dazzi, P., Iuliis, A.D., Gesch, J., Lennerstrand, S., Nesbit-Östman, S., Pires, V.D., Palanca, I.T., Teubenbacher, D., Enengl, F., Hallmann, M., 2024. M5 — Mars magnetospheric multipoint measurement mission: A multi-spacecraft plasma physics mission to Mars. Adv. Space Res. (ISSN: 0273-1177) 73 (6), 3235–3255. http://dx.doi.org/10.1016/j.asr.2023.11.032.

Leamon, R.J., Smith, C.W., Ness, N.F., Matthaeus, W.H., Wong, H.K., 1998. Observational constraints on the dynamics of the interplanetary magnetic field dissipation range. J. Geophys. Res. Space Phys. 103 (A3), 4775–4787.

Lee, C., Hara, T., Halekas, J.S., Thiemann, E., Chamberlin, P., Eparvier, F., Lillis, R.J., Larson, D.E., Dunn, P.A., Espley, J.R., et al., 2017. MAVEN observations of the solar cycle 24 space weather conditions at Mars. J. Geophys. Res. Space Phys. 122 (3), 2768–2794.

Lester, M., Sanchez-Cano, B., Potts, D., Lillis, R., Cartacci, M., Bernardini, F., Orosei, R., Perry, M., Putzig, N., Campbell, B., Blelly, P.-L., Milan, S., Opgenoorth, H., Witasse, O., Redrojo, E.M.M., Russell, A., 2022. The impact of energetic particles on the martian ionosphere during a full solar cycle of radar observations: Radar blackouts. J. Geophys. Res. Space Phys. 127 (2), http://dx.doi.org/10.1029/2021JA029535, e2021JA029535, 2021JA029535.

Lillis, R.J., Deighan, J., Brain, D., Fillingim, M., Jain, S., Chaffin, M., England, S., Holsclaw, G., Chirakkil, K., Al Matroushi, H., Lootah, F., Al Mazmi, H., Thiemann, E., Eparvier, F., Schneider, N., Curry, S., 2022. First synoptic images of FUV discrete aurora and discovery of sinuous aurora at Mars by EMM EMUS. Geophys. Res. Lett. 49 (16), http://dx.doi.org/10.1029/2022GL099820, e2022GL099820, 2022GL099820.

Lin, Y., Lee, L.C., 1999. Reconnection layers in two-dimensional magnetohydrodynamics and comparison with the one-dimensional Riemann problem. Phys. Plasmas 6, 3131–3146. http://dx.doi.org/10.1063/1.873553.

Lin, Y., Lee, L.C., Kennel, C.F., 1992. The role of intermediate shocks in magnetic reconnection. Geophys. Res. Lett. 19 (3), 229–232. http://dx.doi.org/10.1029/91GL03008.

Liu, T.Z., Turner, D.L., Angelopoulos, V., Omidi, N., 2016. Multipoint observations of the structure and evolution of foreshock bubbles and their relation to hot flow anomalies. J. Geophys. Res. (ISSN: 2169-9402) 121 (6), 5489–5509. http://dx.doi.org/10.1002/2016JA022461, 2016JA022461.

Lopez, R.E., 2018. The bow shock current system. In: Electric Currents in Geospace and beyond. American Geophysical Union (AGU), ISBN: 9781119324522, pp. 477–496. http://dx.doi.org/10.1002/9781119324522.ch28.

Luhmann, J.G., Kasprzak, W.T., Russell, C.T., 2007. Space weather at venus and its potential consequences for atmosphere evolution. J. Geophys. Res.: Planets 112 (E4), E04S10. http://dx.doi.org/10.1029/2006JE002820.

Lundquist, S., 1950. Magnetohydrostatic fields. Ark. Fys. 2, 361–365.

Ma, Y.J., Russell, C.T., Fang, X., Dong, Y., Nagy, A.F., Toth, G., Halekas, J.S., Connerney, J.E.P., Espley, J.R., Mahaffy, P.R., Benna, M., McFadden, J.P., Mitchell, D.L., Jakosky, B.M., 2015. MHD model results of solar wind interaction with Mars and comparison with MAVEN plasma observations. Geophys. Res. Lett. 42 (21), 9113–9120. http://dx.doi.org/10.1002/2015gl065218.

Madanian, H., Omidi, N., Sibeck, D.G., Andersson, L., Ramstad, R., Xu, S., Gruesbeck, J.R., Schwartz, S.J., Frahm, R.A., Brain, D.A., Kajdic, P., Eparvier, F.G., Mitchell, D.L., Curry, S.M., 2023. Transient foreshock structures upstream of Mars: Implications of the small martian bow shock. Geophys. Res. Lett. 50 (8), http://dx.doi.org/10.1029/2022GL101734, e2022GL101734.

Marsch, E., Tu, C.Y., 1997. Intermittency, non-Gaussian statistics and fractal scaling of MHD fluctuations in the solar wind. Nonlinear Process. Geophys. 4, 101.

Matthaeus, W.H., Goldstein, M.L., Smith, C., 1982. Evaluation of magnetic helicity in homogeneous turbulence. Phys. Rev. Lett. 48 (18), 1256.

Matthaeus, W.H., Montgomery, D., 1980. Selective decay hypothesis at high mechanical and magnetic Reynolds numbers. New York Acad. Sci., Annals 357, 203–222.

Mayyasi, M., Bhattacharyya, D., Clarke, J., Catalano, A., Benna, M., Mahaffy, P., Thiemann, E., Lee, C.O., Deighan, J., Jain, S., Chaffin, M., Crismani, M., McClintock, W., Stewart, I., Holsclaw, G., Stiepen, A., Montmessin, F., Schneider, N., Jakosky, B., 2018. Significant space weather impact on the escape of hydrogen from Mars. Geophys. Res. Lett. 45 (17), 8844–8852. http://dx.doi.org/10.1029/2018GL077727.

Mazelle, C., Winterhalter, D., Sauer, K., Trotignon, J., Acuña, M., Baumgärtel, K., Bertucci, C., Brain, D., Brecht, S., Delva, M., Dubinin, E., Oieroset, M., Slavin, J., 2004. Bow shock and upstream phenomena at Mars. Space Sci. Rev. 111, 115–181. http://dx.doi.org/10.1023/B:SPAC.0000032717.98679.d0,

McComas, D.J., Allegrini, F., Baldonado, J., Blake, B., Brandt, P.C., Burch, J., Clemmons, J., Crain, W., Delapp, D., DeMajistre, R., et al., 2009. The two wide-angle imaging neutral-atom spectrometers (TWINS) NASA mission-of-opportunity. Space Sci. Rev. 142, 157–231.

Meier, R.R., Englert, C., Chua, D., Socker, D., Picone, J.M., Carter, T., Huba, J., Slinker, S., Krall, J., Vincent, W., 2009. Geospace imaging using Thomson scattering. J. Atmos. Sol.-Terr. Phys. 71 (1), 132–142.

Mela, K., Louie, J.N., 2001. Correlation length and fractal dimension interpretation from seismic data using variograms and power spectra. Geophysics 66 (5), 1372–1378. http://dx.doi.org/10.1190/1.1487083.

Mendes, O., Adhikari, B., Domingues, M.O., Echer, E., Takeshi, R.S., 2022. Interrelationships of similar magnetic effects at low and high latitudes during high-intensity long-duration auroral activity events: Case studies. Braz. J. Phys. 52 (5), 156.

Mendillo, M., Withers, P., Hinson, D., Rishbeth, H., Reinisch, B., 2006. Effects of solar flares on the ionosphere of Mars. Science 311 (5764), 1135–1138. http://dx.doi.org/10.1126/science.112209.

Meng, X., Tsurutani, B.T., Mannucci, A.J., 2019. The solar and interplanetary causes of superstorms (minimum Dst ≤ -250 nT) during the space age. J. Geophys. Res. 124, 3926–3948. http://dx.doi.org/10.1029/2018JA026425.

Miranda, R.A., Rempel, E.L., Chian, A.C.-L., 2015. On–off intermittency and amplitude-phase synchronization in Keplerian shear flows. Mon. Not. R. Astron. Soc. 448 (1), 804–813.

Miranda, R.A., Valdivia, J.A., Chian, A.C.-L., Muñoz, P.R., 2021. Complexity of magnetic-field turbulence at reconnection exhausts in the solar wind at 1 au. Astrophys. J. 923 (2), 132.

Mistry, R., Eastwood, J.P., Phan, T.D., Hietala, H., 2017. Statistical properties of solar wind reconnection exhausts. J. Geophys. Res. Space Phys. 122 (6), 5895–5909.
Mitchell, D.G., Brandt, P.C., Westlake, J.H., Jaskulek, S.E., Andrews, G.B., Nelson, K.S., 2016. Energetic particle imaging: The evolution of techniques in imaging high-energy neutral atom emissions. J. Geophys. Res. Space Phys. 121 (9), 8804–8820.
Montgomery, D., 1987. Remarks on the MHD problem of generic magnetospheres and magnetotails. In: Magnetotail Physics. Springer, p. 203.
Moore, T.E., Chornay, D.J., Collier, M.R., Herrero, F.A., Johnson, J., Johnson, M.A., Keller, J.W., Laudadio, J.F., Lobell, J.F., Ogilvie, K.W., et al., 2000. The low-energy neutral atom imager for IMAGE. Space Sci. Rev. 91 (1–2), 155.
Moses, S.L., Coroniti, F.V., Scarf, F.L., 1988. Expectations for the microphysics of the Mars-solar wind interaction. Geophys. Res. Lett. 15 (5), 429–432, https://doi-org.pbidi.unam.mx:2443/10.1029/GL015i005p00429.
Nagy, A., Winterhalter, D., Sauer, K., Cravens, T., Brecht, S., Mazelle, C., Crider, D., Kallio, E., Zakharov, A., Dubinin, E., Verigin, M., Galina, K., Axford, W., Bertucci, C., Trotignon, J., 2004. The plasma environment of Mars. Space Sci. Rev. 111, 33–114. http://dx.doi.org/10.1023/B:SPAC.0000032718.47512.92,
Nakamura, T.K.M., Blasl, K.A., Hasegawa, H., et al., 2022. Multi-scale evolution of Kelvin-Helmholtz waves at the Earth's magnetopause during southward IMF periods. Phys. Plasmas 29, 012901. http://dx.doi.org/10.1063/5.0067391.
Nakamura, T.K.M., Daughton, W., Karimabadi, H., Eriksson, S., 2013. Three-dimensional dynamics of vortex-induced reconnection and comparison with THEMIS observations. J. Geophys. Res. Space Phys. 118, 5742–5757. http://dx.doi.org/10.1002/jgra.50547.
Nakamura, T.K.M., Hasegawa, H., Daughton, W., Eriksson, S., Li, W.Y., Nakamura, R., 2017. Turbulent mass transfer caused by vortex induced reconnection in collisionless magnetospheric plasmas. Nature Commun. 8, 1582. http://dx.doi.org/10.1038/s41467-017-01579-0.
Nakamura, T.K.M., Plaschke, F., Hasegawa, H., Liu, Y.-H., Hwang, K.-J., Blasl, K.A., Nakamura, R., 2020. Decay of Kelvin-Helmholtz vortices at the Earth's magnetopause under pure southward IMF conditions. Geophys. Res. Lett. 47, http://dx.doi.org/10.1029/2020GL087574, e2020GL087574.
Narita, Y., Glassmeier, K.-H., Motschmann, U., 2022. The wave telescope technique. J. Geophys. Res. Space Phys. 127 (2), http://dx.doi.org/10.1029/2021JA030165, e2021JA030165.
Narita, Y., Plaschke, F., Vörös, Z., 2021. The magnetosheath. In: Magnetospheres in the Solar System. American Geophysical Union (AGU), ISBN: 9781119815624, pp. 137–152. http://dx.doi.org/10.1002/9781119815624.ch9.
Ness, N.F., Scearce, C.S., Seek, J.B., 1964. Initial results of the IMP 1 magnetic field experiment. J. Geophys. Res. (ISSN: 2156-2202) 69 (17), 3531–3569. http://dx.doi.org/10.1029/JZ069i017p03531.
Ng, J., Chen, L.-J., Omelchenko, Y.A., 2021. Bursty magnetic reconnection at the Earth's magnetopause triggered by high-speed jets. Phys. Plasmas 28 (9), 092902. http://dx.doi.org/10.1063/5.0054394.
Norenius, L., Hamrin, M., Goncharov, O., Gunell, H., Opgenoorth, H., Pitkänen, T., Chong, S., Partamies, N., Baddeley, L., 2021. Ground-based magnetometer response to impacting magnetosheath jets. J. Geophys. Res. Space Phys. 126 (8), http://dx.doi.org/10.1029/2021JA029115, e2021JA029115, 2021JA029115.
Němeček, Z., Šafránková, J., Přech, L., Sibeck, D.G., Kokubun, S., Mukai, T., 1998. Transient flux enhancements in the magnetosheath. Geophys. Res. Lett. 25, 1273–1276. http://dx.doi.org/10.1029/98GL50873.
Øieroset, M., Mitchell, D.L., Phan, T.D., Lin, R.P., Acuña, M.H., 2001. Hot diamagnetic cavities upstream of the Martian bow shock. Geophys. Res. Lett. 28 (5), 887–890. http://dx.doi.org/10.1029/2000GL012289.
Omidi, N., 2007. Formation of cavities in the foreshock. In: Shaikh, D., Zank, G.P. (Eds.), Turbulence and Nonlinear Processes in Astrophysical Plasmas. In: American Institute of Physics Conference Series, Vol. 932, pp. 181–190. http://dx.doi.org/10.1063/1.2778962.
Omidi, N., Eastwood, J.P., Sibeck, D.G., 2010. Foreshock bubbles and their global magnetospheric impacts. J. Geophys. Res. 115, A06204. http://dx.doi.org/10.1029/2009JA014828.
Omidi, N., Lee, S.H., Sibeck, D.G., 2021. Ion acceleration by foreshock bubbles. J. Geophys. Res. (Space Phys.) 126 (5), e28924. http://dx.doi.org/10.1029/2020JA028924.
Omidi, N., Sibeck, D.G., Blanco-Cano, X., 2009. Foreshock compressional boundary. J. Geophys. Res. 114, A08205. http://dx.doi.org/10.1029/2008JA013950.
Omidi, N., Sibeck, D., Blanco-Cano, X., Rojas-Castillo, D., Turner, D., Zhang, H., Kajdič, P., 2013. Dynamics of the foreshock compressional boundary and its connection to foreshock cavities. J. Geophys. Res. 118, 823–831. http://dx.doi.org/10.1002/jgra.50146.
Omidi, N., Sibeck, D., Gutynska, O., Trattner, K.J., 2014. Magnetosheath filamentary structures formed by ion acceleration at the quasi-parallel bow shock. J. Geophys. Res. Space Phys. 119 (4), 2593–2604. http://dx.doi.org/10.1002/2013JA019587.
Panov, E.V., Nakamura, R., Baumjohann, W., et al., 2010. Plasma sheet thickness during a bursty bulk flow reversal. J. Geophys. Res. Space Phys. 115, A05213. http://dx.doi.org/10.1029/2009JA014755.
Pinto, V., Stepanova, M., Antonova, E.E., Valdivia, J.A., 2011. Estimation of the eddy-diffusion coefficients in the plasma sheet using THEMIS satellite data. J. Atmos. Sol.-Terr. Phys. (ISSN: 1364-6826) 73 (11), 1472–1477. http://dx.doi.org/10.1016/j.jastp.2011.05.007.
Plaschke, F., Glassmeier, K.H., Sibeck, D.G., Auster, H.U., Constantinescu, O.D., Angelopoulos, V., Magnes, W., 2009. Magnetopause surface oscillation frequencies at different solar wind conditions. Ann. Geophys. 27 (12), 4521–4532. http://dx.doi.org/10.5194/angeo-27-4521-2009.
Plaschke, F., Hietala, H., Angelopoulos, V., 2013. Anti-sunward high-speed jets in the subsolar magnetosheath. Ann. Geophys. 31 (10), 1877–1889. http://dx.doi.org/10.5194/angeo-31-1877-2013.
Plaschke, F., Hietala, H., Archer, M., Blanco-Cano, X., Kajdič, P., Karlsson, T., Lee, S.H., Omidi, N., Palmroth, M., Roytershteyn, V., Schmid, D., Sergeev, V., Sibeck, D., 2018. Jets downstream of collisionless shocks. Space Sci. Rev. 214 (5), 81. http://dx.doi.org/10.1007/s11214-018-0516-3.
Pollock, C.J., Asamura, K., Baldonado, J., Balkey, M.M., Barker, P., Burch, J.L., Korpela, E.J., Cravens, J., Dirks, G., Fok, M.-C., et al., 2000. Medium energy neutral atom (MENA) imager for the IMAGE mission. Space Sci. Rev. 1 (91), 113–154.
Potapov, A., Polyushkina, T., 2010. Experimental evidence for direct penetration of ULF waves from the solar wind and their possible effect on acceleration of radiation belt electrons. Geomagn. Aeron. 50, 950–957. http://dx.doi.org/10.1134/S0016793210080049.
Preisser, L., Blanco-Cano, X., Kajdič, P., Burgess, D., Trotta, D., 2020. Magnetosheath jets and plasmoids: Characteristics and formation mechanisms from hybrid simulations. Astrophys. J. Lett. 900 (1), L6. http://dx.doi.org/10.3847/2041-8213/abad2b.
Priest, E., Forbes, T., 2000. Introduction. In: Magnetic Reconnection: MHD Theory and Applications. Cambridge University Press, pp. 1–47. http://dx.doi.org/10.1017/CBO9780511525087.002.
Qin, M., Zhang, X., Ni, B., Song, H., Zou, H., Sun, Y., 2014. Solar cycle variations of trapped proton flux in the inner radiation belt. J. Geophys. Res. Space Phys. 119 (12), 9658–9669. http://dx.doi.org/10.1002/2014JA020300.
Raath, J.L., Olivier, C.P., Engelbrecht, N.E., 2022. A permutation entropy analysis of voyager interplanetary magnetic field observations. J. Geophys. Res. Space Phys. 127 (6), e2021JA030200.
Rakhmanova, L., Riazantseva, M., Zastenker, G., 2021. Plasma and magnetic field turbulence in the earth's magnetosheath at ion scales. Front. Astron. Space Sci. (ISSN: 2296-987X) 7, http://dx.doi.org/10.3389/fspas.2020.616635.
Raptis, S., Karlsson, T., Vaivads, A., Lindberg, M., Johlander, A., Trollvik, H., 2022. On magnetosheath jet kinetic structure and plasma properties. Geophys. Res. Lett. 49 (21), http://dx.doi.org/10.1029/2022GL100678, e2022GL100678.
Rawat, R., Echer, E., Gonzalez, W.D., 2018. How different are the solar wind-interplanetary conditions and the consequent geomagnetic activity during the ascending and early descending phases of the solar cycles 23 and 24? J. Geophys. Res. 123, 6621–6638. http://dx.doi.org/10.1029/2018JA025683.
Rempel, E.L., Chian, A.C.-L., Beron-Vera, F.J., Szanyi, S., Haller, G., 2017. Objective vortex detection in an astrophysical dynamo. Mon. Not. R. Astron. Soc.: Lett. 466 (1), L108–L112.
Rempel, E.L., Chian, A.C.-L., Brandenburg, A., 2011. Lagrangian coherent structures in nonlinear dynamos. Astrophys. J. Lett. 735 (1), L9.
Rempel, E.L., Chian, A.C.-L., de SA Silva, S., Fedun, V., Verth, G., Miranda, R.A., Gošić, M., 2023. Lagrangian coherent structures in space plasmas. Reviews of Modern Plasma Physics 7 (1), 32. http://dx.doi.org/10.1007/s41614-023-00136-1.
Rempel, E.L., Proctor, M.R.E., Chian, A.C.-L., 2009. A novel type of intermittency in a non-linear dynamo in a compressible flow. Mon. Not. R. Astron. Soc. 400 (1), 509–517.
Richardson, I.G., 2006. The formation of CIRs at stream-stream interfaces and resultant geomagnetic activity. In: Recurrent Magnetic Storms: Corotating Solar Wind Streams. American Geophysical Union (AGU), ISBN: 9781118666456, pp. 45–58. http://dx.doi.org/10.1029/167GM06.
Richardson, I.G., 2018. Solar wind stream interaction regions throughout the heliosphere. Living Rev. Sol. Phys. 15 (1), 1. http://dx.doi.org/10.1007/s41116-017-0011-z.
Rojas-Castillo, D., Blanco-Cano, X., Kajdič, P., Omidi, N., 2013a. Compressional boundaries in the Earth's foreshock. Solar Wind 13 1539, 434–437. http://dx.doi.org/10.1063/1.4811078.
Rojas-Castillo, D., Blanco-Cano, X., Kajdič, P., Omidi, N., 2013b. Foreshock compressional boundaries observed by Cluster. J. Geophys. Res. 118, 698–715. http://dx.doi.org/10.1029/2011JA017385.
Romanelli, N., DiBraccio, G., Halekas, J., Dubinin, E., Gruesbeck, J., Espley, J., Poh, G., Ma, Y., Luhmann, J.G., 2020. Variability of the solar wind flow asymmetry in the martian magnetosheath observed by MAVEN. Geophys. Res. Lett. 47 (22), http://dx.doi.org/10.1029/2020GL090793, e2020GL090793, 10.1029/2020GL090793.
Romanelli, N., Mazelle, C., Chaufray, J.Y., Meziane, K., Shan, L., Ruhunusiri, S., Connerney, J.E.P., Espley, J.R., Eparvier, F., Thiemann, E., Halekas, J.S., Mitchell, D.L., McFadden, J.P., Brain, D., Jakosky, B.M., 2016. Proton cyclotron waves occurrence rate upstream from Mars observed by MAVEN: Associated variability of the Martian upper atmosphere. J. Geophys. Res. (Space Phys.) 121 (11), 11,113–11,128. http://dx.doi.org/10.1002/2016JA023270.
Rosso, O.A., Larrondo, H.A., Martin, M.T., Plastino, A., Fuentes, M.A., 2007. Distinguishing noise from chaos. Phys. Rev. Lett. 99 (15), 154102.

Ruhunusiri, S., Halekas, J.S., Connerney, J.E.P., Espley, J.R., McFadden, J.P., Larson, D.E., Mitchell, D.L., Mazelle, C., Jakosky, B.M., 2015. Low-frequency waves in the martian magnetosphere and their response to upstream solar wind driving conditions. Geophys. Res. Lett. 42 (21), 8917–8924. http://dx.doi.org/10.1002/2015GL064968.

Ruhunusiri, S., Halekas, J.S., Espley, J.R., Mazelle, C., Brain, D., Harada, Y., DiBraccio, G.A., Livi, R., Larson, D.E., Mitchell, D.L., Jakosky, B.M., Howes, G.G., 2017. Characterization of turbulence in the Mars plasma environment with MAVEN observations. J. Geophys. Res. Space Phys. 122 (1), 656–674. http://dx.doi.org/10.1002/2016JA023456.

Ruhunusiri, S., Halekas, J.S., McFadden, J.P., Connerney, J.E.P., Espley, J.R., Harada, Y., Livi, R., Seki, K., Mazelle, C., Brain, D., et al., 2016. MAVEN observations of partially developed Kelvin-Helmholtz vortices at Mars. Geophys. Res. Lett. 43, 4763–4773. http://dx.doi.org/10.1002/2016GL068926.

Russell, C.T., Blanco-Cano, X., Jian, L.K., Luhmann, J.G., 2009. Mirror-mode storms: STEREO observations of protracted generation of small amplitude waves. Geophys. Res. Lett. 36 (5), .. http://dx.doi.org/10.1029/2008GL037113.

Russell, C.T., Luhmann, J.G., Odera, T.J., Stuart, W.F., 1983. The rate of occurrence of dayside Pc 3,4 pulsations: The L-value dependence of the IMF cone angle effect. Geophys. Res. Lett. 10 (8), 663–666. http://dx.doi.org/10.1029/GL010i008p00663.

Russell, C.T., Luhmann, J.G., Schwingenschuh, K., Riedler, W., Yeroshenko, Y., 1990. Upstream waves at Mars: Phobos observations. Geophys. Res. Lett. 17 (6), 897–900. http://dx.doi.org/10.1029/GL017i006p00897.

Šafránková, J., Goncharov, O., Němeček, Z., Přech, L., Sibeck, D.G., 2012. Asymmetric magnetosphere deformation driven by hot flow anomaly(ies). Geophys. Res. Lett. 39 (15), L15107. http://dx.doi.org/10.1029/2012GL052636.

Sánchez-Cano, B., 2023. Mars' ionosphere: The key for systematic exploration of the red planet. Front. Astron. Space Sci, 9, 1101945. http://dx.doi.org/10.3389/fspas.2022.1101945.

Sánchez-Cano, B., Blelly, P.-L., Lester, M., Witasse, O., Cartacci, M., Orosei, R., Opgenoorth, H., Lillis, R., Leblanc, F., Milan, S.E., Conroy, P., Floury, N., Plane, J.M.C., Cicchetti, A., Noschese, R., Kopf, A.J., 2019. Origin of the extended Mars radar blackout of september 2017. J. Geophys. Res. Space Phys. 124 (6), 4556–4568. http://dx.doi.org/10.1029/2018JA026403.

Sánchez-Cano, B., Hall, B.E.S., Lester, M., Mays, M.L., Witasse, O., Ambrosi, R., Andrews, D., Cartacci, M., Cicchetti, A., Holmström, M., Imber, S., Kajdič, P., Milan, S.E., Noschese, R., Odstrcil, D., Opgenoorth, H., Plaut, J., Ramstad, R., Reyes-Ayala, K.I., 2017. Mars plasma system response to solar wind disturbances during solar minimum. J. Geophys. Res. Space Phys. 122 (6), 6611–6634. http://dx.doi.org/10.1002/2016JA023587.

Sánchez-Cano, B., Lester, M., Andrews, D.J., Opgenoorth, H., Lillis, R., Leblanc, F., Fowler, C.M., Fang, X., Vaisberg, O., Mayyasi, M., et al., 2022. Mars' plasma system. Scientific potential of coordinated multipoint missions: "the next generation". Exp. Astron. 54 (2–3), 641–676.

Sánchez-Cano, B., Narvaez, C., Lester, M., Mendillo, M., Mayyasi, M., Holmstrom, M., Halekas, J., Andersson, L., Fowler, C.M., McFadden, J.P., Durward, S., 2020. Mars' ionopause: A matter of pressures. J. Geophys. Res. Space Phys. 125 (9), http://dx.doi.org/10.1029/2020JA028145, e2020JA028145, 2020JA028145.

Sandel, B.R., Goldstein, J., Gallagher, D.L., Spasojevic, M., 2003. Extreme ultraviolet imager observations of the structure and dynamics of the plasmasphere. Magnetospheric Imaging—The Image Prime Mission 25–46.

Sauer, K., Dubinin, E., Baumgärtel, K., 1998. Nonlinear MHD waves and discontinuities in the Martian magnetosheath. Observations and 2D bi-ion MHD simulations. Earth Planets Space 50 (9), 793–801. http://dx.doi.org/10.1186/BF03352171.

Savin, S., Amata, E., Zelenyi, L., Lutsenko, V., Safrankova, J., Nemecek, Z., Borodkova, N., Buechner, J., Daly, P.W., Kronberg, E.A., Blecki, J., Budaev, V., Kozak, L., Skalsky, A., Lezhen, L., 2012. Super fast plasma streams as drivers of transient and anomalous magnetospheric dynamics. Ann. Geophys. 30 (1), 1–7. http://dx.doi.org/10.5194/angeo-30-1-2012.

Schneider, N.M., Deighan, J.I., Jain, S.K., Stiepen, A., Stewart, A.I.F., Larson, D., Mitchell, D.L., Mazelle, C., Lee, C.O., Lillis, R.J., et al., 2015. Discovery of diffuse aurora on Mars. Science 350 (6261), aad0313.

Schneider, N.M., Jain, S.K., Deighan, J., Nasr, C.R., Brain, D.A., Larson, D., Lillis, R., Rahmati, A., Halekas, J.S., Lee, C.O., Chaffin, M.S., Stiepen, A., Crismani, M., Evans, J.S., Stevens, M.H., Lo, D.Y., McClintock, W.E., Stewart, A.I.F., Yelle, R.V., Clarke, J.T., Holsclaw, G.M., Lefevre, F., Montmessin, F., Jakosky, B.M., 2018. Global aurora on Mars during the september 2017 space weather event. Geophys. Res. Lett. 45 (15), 7391–7398. http://dx.doi.org/10.1029/2018GL077772.

Schneider, N.M., Milby, Z., Jain, S.K., Gérard, J.-C., Soret, L., Brain, D.A., Weber, T., Girazian, Z., McFadden, J., Deighan, J., Jakosky, B.M., 2021. Discrete aurora on Mars: Insights into their distribution and activity from MAVEN/IUVS observations. J. Geophys. Res. Space Phys. 126 (10), http://dx.doi.org/10.1029/2021JA029428, e2021JA029428, 2021JA029428.

Schwartz, S.J., 1995. Hot flow anomalies near the Earth's bow shock. Adv. Space Res. 15, 107–116. http://dx.doi.org/10.1016/0273-1177(95)00025-A.

Schwartz, S.J., Andersson, L., Xu, S., Mitchell, D.L., Akbari, H., Ergun, R.E., Mazelle, C., Thaller, S.A., Sales, A.R.N., Horaites, K., DiBraccio, G.A., Meziane, K., 2019. Collisionless electron dynamics in the magnetosheath of Mars. Geophys. Res. Lett. 46 (21), 11,679–11,688. http://dx.doi.org/10.1029/2019GL085037.

Schwartz, S.J., Burgess, D., 1984. On the theoretical/observational comparison of field-aligned ion beams in the earth's foreshock. J. Geophys. Res. 89 (A4), 2381–2384. http://dx.doi.org/10.1029/JA089iA04p02381.

Schwartz, S.J., Burgess, D., Moses, J., 1997. Low-frequency waves in the Earth's magnetosheath: present status . Ann. Geophys. 14 (11), 1134–1150.

Schwartz, S.J., Chaloner, C.P., Christiansen, P.J., Coates, A.J., Hall, D.S., Johnstone, A.D., Gough, M.P., Norris, A.J., Rijnbeek, R.P., Southwood, D.J., Woolliscroft, L.J.C., 1985. An active current sheet in the solar wind. Nature 318 (6043), 269–271.

Schwartz, S.J., Sibeck, D., Wilber, M., Meziane, K., Horbury, T.S., 2006. Kinetic aspects of foreshock cavities. Geophys. Res. Lett. 33, L12103. http://dx.doi.org/10.1029/2005GL025612.

Shen, X.-C., Shi, Q., Wang, B., Zhang, H., Hudson, M.K., Nishimura, Y., Hartinger, M.D., Tian, A., Zong, Q.-G., Rae, I.J., Degeling, A.W., 2018. Dayside magnetospheric and ionospheric responses to a foreshock transient on 25 june 2008: 1. FLR observed by satellite and ground-based magnetometers. J. Geophys. Res. Space Phys. 123 (8), 6335–6346. http://dx.doi.org/10.1029/2018JA025349.

Shuvalov, S.D., Ermakov, V.N., Zorina, V.O., Kim, K.I., 2019. Propagation properties of hot flow anomalies at Mars: MAVEN observations. Planet. Space Sci. (ISSN: 0032-0633) 179, 104717. http://dx.doi.org/10.1016/j.pss.2019.104717.

Sibeck, D.G., Allen, R., Aryan, H., Bodewits, D., Brandt, P., Branduardi-Raymont, G., Brown, G., Carter, J.A., Collado-Vega, Y.M., Collier, M.R., et al., 2018. Imaging plasma density structures in the soft X-rays generated by solar wind charge exchange with neutrals. Space Sci. Rev. 214, 1–124.

Sibeck, D.G., Borodkova, N.L., Schwartz, S.J., Owen, C.J., Kessel, R., Kokubun, S., Lepping, R.P., Lin, R., Liou, K., Lühr, H., McEntire, R.W., Meng, C.-I., Mukai, T., Nemecek, Z., Parks, G., Phan, T.D., Romanov, S.A., Safrankova, J., Sauvaud, J.-A., Singer, H.J., Solovyev, S.I., Szabo, A., Takahashi, K., Williams, D.J., Yumoto, K., Zastenker, G.N., 1999. Comprehensive study of the magnetospheric response to a hot flow anomaly. J. Geophys. Res. 104, 4577–4594. http://dx.doi.org/10.1029/1998JA900021.

Sibeck, D.G., Borodkova, N.L., Zastenker, G.N., Romanov, S.A., Sauvaud, J.-A., 1998. Gross deformation of the dayside magnetopause. Geophys. Res. Lett. 25, 453–456. http://dx.doi.org/10.1029/98GL00134.

Sibeck, D.G., Lee, S.H., Omidi, N., Angelopoulos, V., 2021. Foreshock cavities: Direct transmission through the bow shock. J. Geophys. Res. (Space Phys.) 126 (5), e29201. http://dx.doi.org/10.1029/2021JA029201.

Sibeck, D.G., Murphy, K.R., 2021. Large-scale structure and dynamics of the magnetosphere. Magnetos. Sol. Syst. 15–36.

Sibeck, D.G., Murphy, K.R., Porter, F.S., Connor, H.K., Walsh, B.M., Kuntz, K.D., Zesta, E., Valek, P., Baker, C.L., Goldstein, J., et al., 2023. Quantifying the global solar wind-magnetosphere interaction with the solar-terrestrial observer for the response of the magnetosphere (STORM) mission concept. Front. Astron. Space Sci. 10, 1138616.

Simon Wedlund, C., Volwerk, M., Mazelle, C., Halekas, J., Rojas-Castillo, D., Espley, J., Möstl, C., 2022. Making waves: Mirror mode structures around Mars observed by the MAVEN spacecraft. J. Geophys. Res. Space Phys. 127 (1), http://dx.doi.org/10.1029/2021JA029811, e2021JA029811, 2021JA029811.

Simon Wedlund, C., Volwerk, M., Mazelle, C., Rojas Mata, S., Stenberg Wieser, G., Futaana, Y., Halekas, J., Rojas-Castillo, D., Bertucci, C., Espley, J., 2023. Statistical distribution of mirror mode-like structures in the magnetosheaths of unmagnetised planets: 1. Mars as observed by the MAVEN spacecraft. EGUsphere 2022, 1–40. http://dx.doi.org/10.5194/egusphere-2022-634.

Sitar, R.J., Baker, J.B., Clauer, C.R., Ridley, A.J., Cumnock, J.A., Papitashvili, V.O., Spann, J., Brittnacher, M.J., Parks, G.K., 1998. Multi-instrument analysis of the ionospheric signatures of a hot flow anomaly occurring on July 24, 1996. J. Geophys. Res. Space Phys. 103 (A10), 23357–23372. http://dx.doi.org/10.1029/98JA01916.

Slavin, J.A., Holzer, R.E., 1981. Solar wind flow about the terrestrial planets, 1. Modeling bow shock position and shape. J. Geophys. Res. 86 (A13), 11401–11418. http://dx.doi.org/10.1029/JA086iA13p11401.

Smith, E.J., Wolfe, J.H., 1976. Observations of interaction regions and corotating shocks between one and five AU: Pioneers 10 and 11. Geophys. Res. Lett. 3 (3), 137–140. http://dx.doi.org/10.1029/GL003i003p00137.

Snow, B., Hiller, A., Murtas, G., Botha, G.J.J., 2021. Shock identification and classification in 2D magnetohydrodynamic compressible turbulence - Orszag-Tang vortex. Exp. Results 2 (e35), 1–10. http://dx.doi.org/10.1017/exp.2021.28.

Soriano, M.C., Zunino, L., Larger, L., Fischer, I., Mirasso, C.R., 2011. Distinguishing fingerprints of hyperchaotic and stochastic dynamics in optical chaos from a delayed opto-electronic oscillator. Opt. Lett. 36 (12), 2212–2214.

Sorriso-Valvo, L., Carbone, V., Giuliani, P., Veltri, P., Bruno, R., Antoni, V., Martines, E., 2001. Intermittency in plasma turbulence. Planet. Space Sci. 49 (12), 1193–1200.

Souza, A.M., Echer, E., Bolzan, M.J.A., Hajra, R., 2016. A study on the main periodicities in interplanetary magnetic field Bz component and geomagnetic AE index during HILDCAA events using wavelet analysis. J. Atmos. Sol.-Terr. Phys. 149, 81–86.

Steinolfson, R.S., Hundhausen, A.J., 1990a. Coronal mass ejection shock fronts containing the two types of intermediate shocks. J. Geophys. Res. 95 (A12), 20,693–20,699. http://dx.doi.org/10.1029/JA095iA12p20693.

Steinolfson, R.S., Hundhausen, A.J., 1990b. MHD intermediate shocks in coronal mass ejections. J. Geophys. Res. 95 (A5), 6389–6401. http://dx.doi.org/10.1029/JA095iA05p06389.

Stepanova, M.V., Antonova, E.E., Troshichev, O., 2003. Intermittency of magnetospheric dynamics through non-Gaussian distribution function of PC-index fluctuations. Geophys. Res. Lett. 30 (3), 1127. http://dx.doi.org/10.1029/2002GL016070.

Stepanova, M., Pinto, V.A., Valdivia, J.A., Antonova, E.E., 2011. Spatial distribution of the eddy diffusion coefficients in the plasma sheet during quiet time and substorms from THEMIS satellite data. J. Geophys. Res. (Space Phys.) 116, A00I24. http://dx.doi.org/10.1029/2010JA015887.

Sugiura, M., 1964. Hourly values of equatorial Dst for the IGY. Ann. Int. Geophys. Year 35, 9.

Suvorova, A.V., Dmitriev, A.V., Parkhomov, V.A., Tsegmed, B., 2019. Quiet time structured Pc1 waves generated during transient foreshock. J. Geophys. Res. (Space Phys.) 124 (11), 9075–9093. http://dx.doi.org/10.1029/2019JA026936.

Tarduno, J.A., Watkeys, M.K., Huffman, T.N., Cottrell, R.D., Blackman, E.G., Wendt, A., Scribner, C.A., Wagner, C.L., 2015. Antiquity of the south atlantic anomaly and evidence for top-down control on the geodynamo. Nature Commun. 6 (1), 7865. http://dx.doi.org/10.1038/ncomms8865.

Tarvus, V., Turc, L., Battarbee, M., Suni, J., Blanco-Cano, X., Ganse, U., Pfau-Kempf, Y., Alho, M., Dubart, M., Grandin, M., Johlander, A., Papadakis, K., Palmroth, M., 2021. Foreshock cavitons and spontaneous hot flow anomalies: a statistical study with a global hybrid-vlasov simulation. Ann. Geophys. 39 (5), 911–928. http://dx.doi.org/10.5194/angeo-39-911-2021.

Telloni, D., Carbone, V., Perri, S., Bruno, R., Lepreti, F., Veltri, P., 2016. Relaxation processes within flux ropes in solar wind. Astrophys. J. 826 (2), 205.

Temmer, M., 2021. Space weather: the solar perspective. Living Rev. Sol. Phys. 18 (1), 4. http://dx.doi.org/10.1007/s41116-021-00030-3.

Terada, N., Machida, S., Shinagawa, H., 2002. Global hybrid simulation of the kelvin-Helmholtz instability at the venus ionopause. J. Geophys. Res. 107 (A12), 1471. http://dx.doi.org/10.1029/2001JA009224.

Thaller, S.A., Andersson, L., Schwartz, S.J., Mazelle, C., Fowler, C., Goodrich, K., Newman, D., Halekas, J., Pilinski, M.D., Pollard, M., 2022. Bipolar electric field pulses in the martian magnetosheath and solar wind; their implication and impact accessed by system scale size. J. Geophys. Res. Space Phys. 127 (7), http://dx.doi.org/10.1029/2022JA030374, e2022JA030374, 2022JA030374.

Thébault, E., C Finlay, C., D Beggan, C., Alken, P., 2015. International geomagnetic reference field: the 12th generation. Earth Planets Space 67:79. http://dx.doi.org/10.1186/s40623-015-0228-9.

Thiemann, E.M.B., Eparvier, F.G., Andersson, L.A., Fowler, C.M., Peterson, W.K., Mahaffy, P.R., England, S.L., Larson, D.E., Lo, D.Y., Schneider, N.M., Deighan, J.I., McClintock, W.E., Jakosky, B.M., 2015. Neutral density response to solar flares at Mars. Geophys. Res. Lett. 42 (21), 8986–8992. http://dx.doi.org/10.1002/2015GL066334.

Thomsen, M.F., Gosling, J.T., Fuselier, S.A., Bame, S.J., Russell, C.T., 1986. Hot, diamagnetic cavities upstream from the Earth's bow shock. J. Geophys. Res. Space Phys. 91 (A3), 2961–2973. http://dx.doi.org/10.1029/JA091iA03p02961.

Thomsen, M.F., Thomas, V.A., Winske, D., Gosling, J.T., Farris, M.H., Russell, C.T., 1993. Observational test of hot flow anomaly formation by the interaction of a magnetic discontinuity with the bow shock. J. Geophys. Res. 98, 15. http://dx.doi.org/10.1029/93JA00792.

Toledo, B., Medina, P., Blunier, S., Rogan, J., Stepanova, M., Valdivia, J.A., 2021. Multifractal characteristics of geomagnetic field fluctuations for the northern and southern hemispheres at swarm altitude. Entropy (ISSN: 1099-4300) 23 (5), 558. http://dx.doi.org/10.3390/e23050558.

Torr, M.R., Torr, D.G., Zukic, M., Johnson, R.B., Ajello, J., Banks, P., Clark, K., Cole, K., Keffer, C., Parks, G., et al., 1995. A far ultraviolet imager for the international solar-terrestrial physics mission. Space Sci. Rev. 71, 329–383.

Torrence, C., Compo, G.P., 1998. A practical guide to wavelet analysis. Bull. Am. Meteorol. Soc. 79, 61–78. http://dx.doi.org/10.1175/1520-0477(1998)079<0061:APGTWA>2.0.CO;2.

Troitskaya, V.A., Plyasova-Bakunina, T.A., Gul'Elmi, A.V., 1971. The connection of Pc2-4 pulsations with the interplanetary magnetic field. Akademiia Nauk SSSR Doklady 197, 1312–1314.

Troshichev, O., Antonova, E.E., Kamide, Y., 2002. Inconsistency of magnetic field and plasma velocity variations in the distant plasma sheet: violation of the "frozen-in" criterion? Adv. Space Res. 30 (12), 2683–2687.

Tsurutani, B.T., Gonzalez, W.D., 1987. The cause of high-intensity long-duration continuous AE activity (HILDCAAs): interplanetary Alfvén wave trains. Planet. Space Sci. 35, 405–412.

Tsurutani, B.T., Gonzalez, W.D., Gonzalez, A.L.C., Guarnieri, F.L., Gopalswamy, N., Grande, M., Kamide, Y., Kasahara, Y., Lu, G., Mann, I., McPherron, R., Soraas, F., Vasyliunas, V., 2006. Corotating solar wind streams and recurrent geomagnetic activity: A review. J. Geophys. Res. Space Phys. 111 (A7), A07S01. http://dx.doi.org/10.1029/2005JA011273.

Tsurutani, B.T., Gonzalez, W.D., Tang, F., Akasofu, S.I., Smith, E.J., 1988. Origin of interplanetary southward magnetic fields responsible for major magnetic storms near solar maximum (1978–1979). J. Geophys. Res. 93 (A8), 8519–8531. http://dx.doi.org/10.1029/JA093iA08p08519.

Turner, D.L., Omidi, N., Sibeck, D.G., Angelopoulos, V., 2013. First observations of foreshock bubbles upstream of Earth's bow shock: Characteristics and comparisons to HFAs. J. Geophys. Res. 118, 1552–1570. http://dx.doi.org/10.1002/jgra.50198.

Vaisberg, O., 1992. The solar wind interaction with Mars: A review of results from previous soviet missions to Mars. Adv. Space Res. (ISSN: 0273-1177) 12 (9), 137–161. http://dx.doi.org/10.1016/0273-1177(92)90328-U.

Valdivia, J.A., Rogan, J., Muñoz, V., Toledo, B.A., Stepanova, M., 2013. The magnetosphere as a complex system. Adv. Space Res. (ISSN: 02731177) 51 (10), 1934–1941. http://dx.doi.org/10.1016/j.asr.2012.04.004.

Vallance Jones, A., 1974. Aurora. Geophysics and Astrophysics Monographs 9.

Vassiliadis, D., Klimas, A.J., Valdivia, J.A., Baker, D.N., 1999. The Dst geomagnetic response as a function of storm phase and amplitude and the solar wind electric field. J. Geophys. Res. Space Phys. 104 (A11), 24957–24976. http://dx.doi.org/10.1029/1999JA900185.

Veltri, P., 1999. MHD turbulence in the solar wind: self-similarity, intermittency and coherent structures. Plasma Phys. Control. Fusion 41 (3A), A787.

Verigin, M.I., Shutte, N.M., Galeev, A.A., Gringauz, K.I., Kotova, G.A., Remizov, A.P., Rosenbauer, H., Hemmerich, P., Livi, S., Richter, A.K., 1991. Ions of planetary origin in the Martian magnetosphere (Phobos 2/TAUS experiment). Planet. Space Sci. 39 (1–2), 131–137. http://dx.doi.org/10.1016/0032-0633(91)90135-W.

Vörös, Z., Baumjohann, W., Nakamura, R., Volwerk, M., Runov, A., Zhang, T.L., Klecker, B., Rème, H., 2004. Magnetic turbulence in the plasma sheet. J. Geophys. Res. Space Phys. 109 (A11), A11215.

Vuorinen, L., Hietala, H., Plaschke, F., 2019. Jets in the magnetosheath: IMF control of where they occur. Ann. Geophys. 37 (4), 689–697. http://dx.doi.org/10.5194/angeo-37-689-2019.

Walsh, B.M., Collier, M.R., Kuntz, K.D., Porter, F.S., Sibeck, D.G., Snowden, S.L., Carter, J.A., Collado-Vega, Y., Connor, H.K., Cravens, T.E., et al., 2016. Wide field-of-view soft X-ray imaging for solar wind-magnetosphere interactions. J. Geophys. Res. Space Phys. 121 (4), 3353–3361.

Wang, B., Nishimura, Y., Hietala, H., Angelopoulos, V., 2022. Investigating the role of magnetosheath high-speed jets in triggering dayside ground magnetic ultra-low frequency waves. Geophys. Res. Lett. 49 (22), http://dx.doi.org/10.1029/2022GL099768, e2022GL099768, 2022GL099768.

Wang, M., Yao, S., Shi, Q., Zhang, H., Tian, A., Degeling, A.W., Zhang, S., Guo, R., Sun, W., Liu, J., Bai, S., Shen, X., Zhu, X., Fu, S., Pu, Z., 2020. Propagation properties of foreshock cavitons: Cluster observations. Sci. China E: Technol. Sci. 63 (1), 173–182. http://dx.doi.org/10.1007/s11431-018-9450-3.

Wang, S., Zong, Q., Zhang, H., 2013. Hot flow anomaly formation and evolution: Cluster observations. J. Geophys. Res. Space Phys. 118 (7), 4360–4380. http://dx.doi.org/10.1002/jgra.50424.

Weck, P.J., Schaffner, D.A., Brown, M.R., Wicks, R.T., 2015. Permutation entropy and statistical complexity analysis of turbulence in laboratory plasmas and the solar wind. Phys. Rev. E 91 (2), 023101.

Weygand, J.M., Kivelson, M.G., 2019. Jensen–Shannon complexity measurements in solar wind magnetic field fluctuations. Astrophys. J. 872 (1), 59.

Weygand, J.M., Matthaeus, W.H., El-Alaoui, M., Kivelson, M.G., Walker, R.J., Goldstein, M.L., 2010. Anisotropy of the taylor scale and the correlation scale in plasma sheet magnetic field fluctuations as a function of auroral electrojet activity. J. Geophys. Res. Space Phys. 115 (A12), A12250.

Winningham, J., Frahm, R., Sharber, J., Coates, A., Linder, D., Soobiah, Y., Kallio, E., Espley, J., Lundin, R., Barabash, S., Holmström, M., Andersson, H., Yamauchi, M., Grigoriev, A., Scherrer, J., Jeffers, S., Kataria, D., Kozyra, J., Luhmann, J., Dierker, C., 2006. Electron oscillations in the induced martian magnetosphere. Icarus 182, 360–370. http://dx.doi.org/10.1016/j.icarus.2005.10.033.

Winterhalter, D., Neugebauer, M., Goldstein, B.E., Smith, E.J., Tsurutani, B.T., Bame, S.J., Balogh, A., 1995. Magnetic holes in the solar wind and their relation to mirror mode structures. Space Sci. Rev. 72 (1–2), 201–204. http://dx.doi.org/10.1007/BF00768780.

Wu, C.C., 1987. On MHD intermediate shocks. Geophys. Res. Lett. 14 (6), 668–671. http://dx.doi.org/10.1029/GL014i006p00668.

Wu, C.C., 1988. The MHD intermediate shock interaction with an intermediate wave: are intermediate shocks physical? J. Geophy. Res. 93 (A2), 987–990. http://dx.doi.org/10.1029/JA093iA02p00987.

Wu, M., Chen, Y., Du, A., Wang, G., Xiao, S., Peng, E., Pan, Z., Chen, Y., Zhang, T., 2021. Statistical properties of small-scale linear magnetic holes in the martian magnetosheath. Astrophys. J. 916 (2), 104. http://dx.doi.org/10.3847/1538-4357/ac090b.

Yeroshenko, Y., Riedler, W., Schwingenschuh, K., Luhmann, J.G., Ong, M., 1990. The magnetotail of Mars: Phobos observations. Geophys. Res. Lett. 17 (6), 885–888. http://dx.doi.org/10.1029/GL017i006p00885.

Zhang, Y., Li, L., Xie, L., Kong, L., Li, W., Tang, B., Ma, J., Zhang, A., 2023. Inversion of upstream solar wind parameters from ENA observations at Mars. Remote Sens. 15 (7), 1721.

Zhang, H., Sibeck, D.G., Zong, Q.G., Gary, S.P., McFadden, J.P., Larson, D., Glassmeier, K.H., Angelopoulos, V., 2010. Time History of Events and Macroscale Interactions during Substorms observations of a series of hot flow anomaly events. J. Geophys. Res. (Space Phys.) 115 (A12), A12235. http://dx.doi.org/10.1029/2009JA015180.

Zhang, H., Sibeck, D.G., Zong, Q.-G., Omidi, N., Turner, D., Clausen, L.B.N., 2013. Spontaneous hot flow anomalies at quasi-parallel shocks: 1. observations. J. Geophys. Res. (ISSN: 2169-9402) 118 (6), 3357–3363. http://dx.doi.org/10.1002/jgra.50376.

Zhao, D., Guo, J., Lin, H., Meng, W., Chen, Y., Wei, Y., Liu, L., 2023. Upstream proton cyclotron waves at Mars duing the passage of solar wind stream interaction regions. Astron. Astrophys. 674, 1–12.

Zhao, L.L., Zhang, H., Zong, Q.G., 2017. Global ULF waves generated by a hot flow anomaly. Geophys. Res. Lett. 44 (11), 5283–5291. http://dx.doi.org/10.1002/2017GL073249.

Zirker, J.B., 1977. Coronal holes and high-speed wind streams. Rev. Geophys. 15 (3), 257–269.

Zou, H., Li, C., Zong, Q., Parks, G.K., Pu, Z., Chen, H., Xie, L., Zhang, X., 2015. Short-term variations of the inner radiation belt in the South Atlantic Anomaly. J. Geophys. Res. Space Phys. 120, 4475–4486. http://dx.doi.org/10.1002/2015JA021312.

Zou, H., Zong, Q.G., Parks, G.K., Pu, Z.Y., Chen, H.F., Xie, L., 2011. Response of high-energy protons of the inner radiation belt to large magnetic storms. J. Geophys. Res. 116, A10229. http://dx.doi.org/10.1029/2011JA016733.

Zunino, L., Zanin, M., Tabak, B.M., Pérez, D.G., Rosso, O.A., 2009. Forbidden patterns, permutation entropy and stock market inefficiency. Phys. A 388 (14), 2854–2864.